This is a non-peer-reviewed preprint submitted to EarthArXiv, currently under review in Urban Climate as of March 2026.

Are high-resolution urban datasets necessary for accurate heat exposure modelling in cities?

Maryam Fazeli[1,2,3,4] (m.fazeli@unsw.edu.au), Negin Nazarian[1,2,3,4] (n.nazarian@unsw.edu.au), Jason P. Evans[2,3,4] (jason.evans@unsw.edu.au), Mathew J. Lipson[2,3,4] (m.lipson@unsw.edu.au), Jacobo Gabeiras Penas[5] (jacobo.gabeiras-penas@univ-grenoble-alpes.fr), Shankar Sharma[2,3,4] (shankar.sharma@unsw.edu.au), Alberto Martilli[6] (alberto.martilli@ciemat.es)

[1]School of Built Environment, UNSW, Australia
[2]Climate Change Research Centre, UNSW, Australia
[3]ARC Centre of Excellence for Weather of the 21st Century, Australia
[4]ARC Centre of Excellence for Climate Extremes, Australia
[5]Université Grenoble Alpes, France
[6]Environmental Department, CIEMAT, Spain

Abstract

Accurately capturing the spatial variability of urban heat exposure is important for planning heat-resilient cities. While regional climate models have historically simplified urban characteristics, high-resolution urban morphological datasets now present an opportunity to produce spatially accurate heat maps. In this vein, this study evaluates four morphological datasets for Sydney, Australia in the Weather Research and Forecasting (WRF) model during the extremely hot period of 10-20 January 2017: the default IGBP-MODIS data with no local morphology, a class-based Local Climate Zones (LCZ) dataset requiring parameter interpretation by modellers, and explicitly defined parameter datasets from World Settlement Footprint 3D (WSF-MB) and Geoscape. The latter three used the BEP-BEM-Comfort urban canopy model, which outputs subgrid-scale Universal Thermal Climate Index (UTCI), an indicator of human thermal stress. Comparison with observations showed any urban dataset over WRF default reduced 2m temperature mean absolute errors (MAEs) at peak solar hours by at least 1°C on average, while localized instantaneous and median temperature differences reached 13°C and 4.5°C across the domain. High-resolution gridded experiments outperformed LCZ temperature predictions by up to 0.37°C (MAE) before sunrise. LCZ and Gridded experiments revealed substantial UTCI differences, with LCZ predicting four times lower probability of extreme heat stress in the afternoon, and 2-3°C lower average UTCI exceedances in Western Sydney. Urban dataset choice mattered most under weak synoptic conditions, though simplified datasets could have critical discrepancies in estimating localised heat stress even during strong forcing. The findings underscore the importance of high-resolution data for identifying heat-vulnerable times and locations.

Keywords: Heat Extremes, Urban Climate, Urban Morphology, WRF, Urban Canopy Model, Heat Exposure

Highlights

- Four urban datasets were compared for their predictive accuracy in heat modelling
- WRF default had 1°C worse temperature MAE than the spatial datasets at peak heating
- LCZ underestimated afternoon extreme heat stress by 4x compared with gridded data
- LCZ had 2-3°C lower average UTCI exceedances than gridded data in Sydney's west
- Urban dataset choice mattered most under weak synoptic conditions

1. Introduction

Heat is the deadliest natural hazard in Australia (Coates et al., 2022), increasingly disrupting our health, economy, and environment (Abunyewah et al., 2025). In cities, in particular, heat is a growing challenge due to the compounding effect of climate change and urbanisation (Ghanbari et al., 2023; Ren et al., 2022; Wu et al., 2021). Most Australians live in urban environments – 90% in 2021 (Australian Bureau of Statistics, 2021) – motivating quantifying urban heat to better understand health risks for inhabitants.

Understanding urban heat requires a multiscale consideration of drivers and impacts. Large-scale physical processes affect weather and climate patterns over cities while local-scale design affects intra-urban temperature distribution. As a result, in recent decades, cities have experienced higher temperatures and more frequent, stronger, and longer heatwaves and the trend is projected to continue (Bhattarai et al., 2025; Meehl and Tebaldi, 2004; Xue et al., 2024). This in turn results in different levels of impacts on life on a broad city scale through the economy and energy consumption (He et al., 2022; Lipson et al., 2019; Miner et al., 2017; Obringer et al., 2022; Salamanca et al., 2014; Santamouris et al., 2020; Shen et al., 2025) – down to an individual level concerning health, exposure to heat, morbidity, mortality, and cognitive performance (Arsad et al., 2022; Cedeño Laurent et al., 2018; Faurie et al., 2022; Guo et al., 2017; Marcotullio et al., 2022; Mazloumi et al., 2014; Nazarian et al., 2022; Nazarian and Lee, 2021; Tong et al., 2021; Yang et al., 2024).

Addressing urban heat requires an accurate representation of heat across the landscape (Fuhrmann et al., 2024). Achieving this is particularly challenging in cities, where heterogeneous morphologies entail complex land-atmosphere processes (Oke, 1982). Capturing these urban heterogeneities demands high-resolution modelling, for which regional convection-permitting climate models are an appropriate tool (Prein et al., 2015). These models, however, need to be informed with accurate urban data and physics. Only an appropriate resolution of urban surface and land data can reflect the intra-urban variability of heat exposure in the modelling process (Thisara Sathsara and Kusaka, 2025).

Historically, regional climate models did not include local urban characteristics, instead they described urban areas as a generic class using modified roughness length and thermal properties – an approach that persists in the modelling community to this day (Argüeso et al., 2014; Katzfey et al., 2020; Li et al., 2016). However, advanced technological developments such as LiDAR and artificial intelligence in conjunction with satellite data have allowed for a range of datasets to emerge that can describe local urban characteristics globally (Biljecki et al., 2021; “Geoscape Australia,” 2022; Sirko et al., 2021). Such datasets have undergone different processing methods to enable their use in regional climate models, resulting in the development of class-based datasets based on, e.g., local climate zones, as in (Ching et al., 2018), or developing gridded datasets with unique building information at the grid-level, such as in (Cheng et al., 2025; Esch et al., 2022; Liao et al., 2025; Lipson et al., 2022). In class-based datasets, the city is divided into a limited number of neighbourhood “types” such as compact highrise, open midrise, and heavy industry (Stewart and Oke, 2012). Yet, given their recent availability, how the application and potential of different representations of urban areas compare in regional climate models remains underexplored.

Furthermore, preparing people for the consequences of urban heat requires relevant indicators. Air temperature (commonly extracted at 2-meter in meso-scale models) and urban heat island

intensity are common indices to measure urban heat using regional climate models outputs, but they do not represent how people feel thermally (Martilli et al., 2020; Nazarian et al., 2022). Human thermal comfort is affected by other meteorological parameters (e.g. wind speed, absolute/relative humidity, and mean radiant temperature) in addition to air temperature, as well as physiological, psychological characteristics (de Dear and Brager, 1998). These are better described in thermal comfort indices such as the universal thermal climate index UTCI (Jendritzky et al., 2012; Jendritzky and Tinz, 2009). A recently developed urban canopy model (UCM) in the Weather Research and Forecast WRF model – WRF-Comfort (Martilli et al., 2024) – addresses this limitation by enabling modelling of sub-grid variability in UTCI, capturing a clearer picture of how urban heat landscape is affected by local heterogeneities, making it well-suited for our study.

The overarching aim of this research is to assess the impact of different urban morphological representations on the accuracy of human-centric heat exposure maps. Implementing four different representations of urban datasets – two grid-level building information from local and global sources, one class-based, and one representing urban areas as a special natural land as the most simplified practice - and three different heat indicators, 2m air temperature, UTCI, and average UTCI exceedance, this study attempts to answer three research questions:

- Are high-resolution urban datasets necessary for accurate mesoscale heat exposure modelling in cities?
- How does a temperature-based analysis compare with a human heat exposure one (based on e.g., UTCI) using spatial datasets in urban climate modelling?
- When is it most beneficial to use high-resolution urban datasets in urban heat modelling?

The rest of the paper is structured as follows: Section 2 first describes the case study and model setup. It then introduces the three morphological datasets (that are used with urban physics activated) that will be compared with the common practice of the broad community of WRF users: using the default bulk urban scheme and the default land use land cover data (LULC) of WRF. Section 3 includes Results and Discussion presenting a detailed comparison between the urban datasets, evaluation of the model temperature outputs with the observations, and spatial analysis of the heat exposure maps, as well as comparing UTCI with 2m temperature, and in the end explaining the effect of synoptic forcing of varying degrees. Section 4 outlines the concluding remarks.

2. Methods

The case study is Sydney, Australia, a coastal city with subtropical and temperate climate classes (The Bureau of Meteorology, 2025). Two computational domains were used to study Sydney's heat exposure conditions during 10-20 January 2017, with the parent domain covering the southeastern coasts of Australia (Figure 1 (a)). Summer 2017 was an unusually hot summer in southeast Australia with several heatwaves, two of which falling within our 10-day simulated period. January 2017, in particular, was the warmest January on record for Sydney since measurements started in 1910 (The Bureau of Meteorology, 2017). Such outstanding conditions make this period suitable for a heat exposure study. We compare our results with 13 weather stations – 5 from the Australian Bureau of Meteorology (BoM) and 8 from New South Wales Department of Climate Change, Energy, the Environment and Water (DCCEEW, 2023) – to

confirm the model setup and to evaluate the performance of implementing each morphological dataset in WRF (Figure 1 (b)).

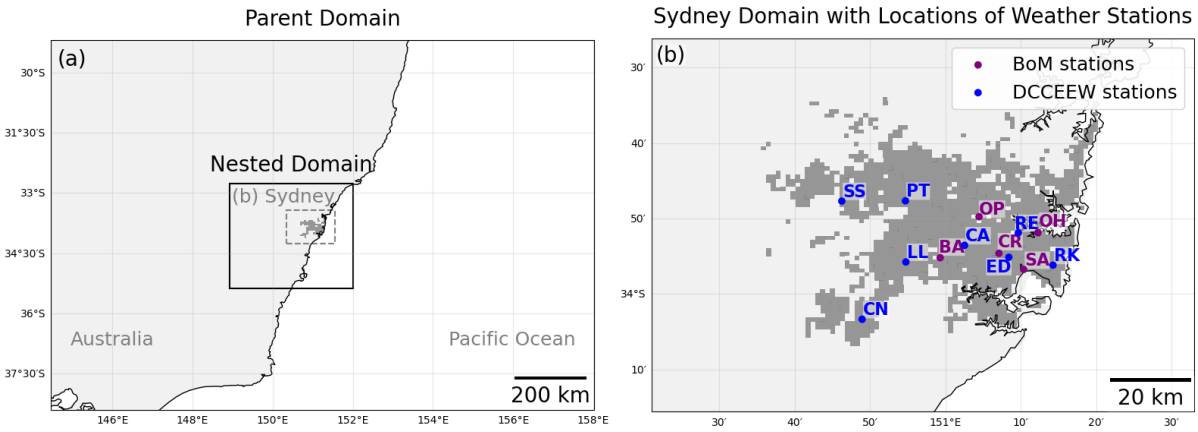

Figure 1. The parent domain located in Southeastern coasts of Australia within latitudes = (-38.37, -29.23) and longitudes = (144.50, 157.98) and the nested domain within latitudes (-35.38, -32.77) and longitudes = (148.93, 152.00) including Sydney (a). Sydney computational domain with the locations of official weather stations from the Bureau of Meteorology (BoM) and NSW Department of Climate Change, Energy, the Environment and Water (DCCEEW) (b). BoM stations include Sydney Observatory Hill (OH), Sydney Airport (SA), Canterbury Racecourse (CR), Sydney Olympic Park (OP), Bankstown Airport (BA). DCCEEW stations include Randwick (RK), Rozelle (RE), Earlwood (ED), Chullora (CA), Liverpool (LL), Prospect (PT), Campbelltown (CN), St Marys (SS). Sydney boundaries delineate study areas and do not necessarily depict accepted national boundaries.

2.1. Numerical Model and Configurations

To quantify the amount of heat exposure to people at a city scale, mesoscale models that can simulate conditions within the urban canopy layer (e.g. the pedestrian-level atmosphere) are useful. Weather Research and Forecasting model (WRF) is a widely-adopted weather prediction system for mesoscale modelling (Skamarock et al., 2019) with built-in urban canopy models (UCMs). Building Effect Parameterisation BEP (Martilli et al., 2002) is a UCM that considers the effect of buildings on urban climate through computing the impact of vertical and horizontal surfaces of street canyons on air temperature, radiation, wind speed, humidity and turbulent kinetic energy. Following that, (Salamanca et al., 2010; Salamanca and Martilli, 2010) introduced a building energy model (BEM) to also consider the internal/external heat fluxes of urban buildings, natural ventilation, occupant and equipment heat generation, and air conditioning use. The combination of the two schemes (BEP-BEM) is commonly used for high-resolution urban modelling at the pedestrian level within the WRF modelling community.

In this study, we have used WRF-Comfort (Martilli et al., 2024), a recent development of BEP-BEM, on WRF version 4.5.2. WRF-Comfort focuses on improving the relevancy of mesoscale modelling outputs to human thermal comfort. It uses UTCI, a heat index based on human thermal comfort, to specify the range of thermal exposure. UTCI has four variables: temperature, wind speed, humidity, and mean radiant temperature. To account for sub-grid variability, WRF-Comfort considers different locations a pedestrian may be standing within an urban environment, paramaterised from 1 m resolution computational fluid dynamics simulation data. For each mesoscale grid cell, WRF-Comfort uses three wind speeds (as a function of urban morphology and mean wind velocity), six mean radiant temperatures (for three pedestrian locations – the middle and sides of the canopy – and two street directions – North-South and East-West), and three air temperatures (simply assuming ±1 degree

difference). Absolute humidity is assumed to be constant within the canopy, but relative humidity is calculated for three different temperatures. Taking into account these variations, 54 different UTCI values are calculated for each mesoscale grid cell. The 10th and 90th percentile values of UTCI correspond to the UTCI "cool spot" and UTCI "hot spot" values, respectively.

A two-way nesting method is used with two domains, including a parent domain with 238×201 grids at a 5km resolution and a model domain with 281×291 grids at a 1km resolution. The initial and boundary conditions were established by ERA5 (Copernicus Climate Change Service, 2018; Hersbach et al., 2020) and ERA5-Land reanalysis datasets (Copernicus Climate Change Service, 2019; Muñoz-Sabater et al., 2021), with approximately 31km and 9km horizontal resolution, respectively. A 5-second time step was chosen for the inner domain, with outputs written hourly.

Table 1 shows the physical parameterisation schemes used in WRF. When using BEP-BEM, the surface layer scheme is disabled over urban areas and the 2m temperature is calculated at the middle point of the first model level (Salamanca et al., 2018). Hence, we have defined 50 model levels to obtain 2m temperature values over urban areas.

Table 1. The selected physics options in WRF. The schemes were used for both domains, except that no cumulus scheme has been used for the nested domain.

Physics Option	Scheme	Reference
Microphysics	WRF Single-Moment 6-Class (WSM6)	(Hong and Lim, 2006)
Cumulus	Multi-scale Kain-Fritsch	(Bechtold et al., 2001; Glotfelty et al., 2019; Zheng et al., 2016)
Long Wave Radiation	Rapid Radiative Transfer Model for GCMs (RRTMG)	(Iacono et al., 2008)
Short Wave Radiation	Rapid Radiative Transfer Model for GCMs (RRTMG)	(Iacono et al., 2008)
Boundary Layer	Bougeault-Lacarrère (BouLac)	(Bougeault and Lacarrere, 1989)
Surface Layer	Monin-Obukhov (Janjić)	(Janjić, 2001, 1996, 1994; Monin and Obukhov, 2009)
Land Surface	Noah, the Multi-Parameterisation Option (Noah-MP)	(Niu et al., 2011; Yang et al., 2011)
Urban Canopy Model	BEP-BEM-Comfort	(Martilli et al., 2024)

2.2. Urban Datasets

Four urban morphological datasets are considered here (Table 2): Default WRF land use/ land cover (LULC), Local Climate Zones (LCZs) with ten urban classes, and two continuously varying gridded datasets derived from local and global sources.

By default, WRF uses the Noah-modified IGBP-MODIS LULC dataset at ~927m resolution (Skamarock et al., 2019) for describing land surface characteristics for the whole domain through 20 classifications including 'snow and ice', 'water', 'croplands', different types of 'shrublands', 'forests', 'savannas', and so on. Alongside the natural types, one special class appears as 'urban and built-up' described with the same land cover characteristics (e.g., min/max of surface albedo, roughness, and emissivity) as natural classes. In this class, urban areas appear as a homogeneous, completely impervious area with a constant roughness length of 1m. The defaults of WRF consist of this land dataset alongside the bulk urban

parameterisation (no urban canopy model (UCM) activated) for urban physics. We have used this combination as our simplest case, labelled as 'Default', which would be informative for the WRF users beyond the urban community who would only use the defaults for urban land and physics.

The other three experiments still use IGBP-MODIS for describing their natural land cover, but their urban land description is more advanced. These three experiments use spatially-heterogeneous urban datasets that include impervious fraction, plan area density, building surface to plan area ratio, area-weighted mean building height, and building height histograms (a three-dimensional variable in the geo_em file with 15 bins) as their morphological parameters. These datasets are run with the BEP-BEM-Comfort UCM (Martilli et al., 2024) – see Section 2.1.

The local climate zones dataset 'LCZ' – from the World Urban Database and Access Portal Tools WUDAPT (Ching et al., 2018) – has the morphological data of a given city processed into 10 urban classes at 100m resolution. The default values of WUDAPT-to-WRF (W2W) by (Demuzere et al., 2022) are used for urban canopy parameters which generally follow the mid-range values of the original landmark study by (Stewart and Oke, 2012) and (Stewart et al., 2014). The next dataset uses the World Settlement Footprint 3D dataset (Esch et al., 2022) which contains urban data at 90m resolution, complemented by Microsoft Building Footprints (*GlobalMLBuildingFootprints*, 2024), labelled as 'WSF-MB' experiment here.

Unlike the other datasets that are satellite-based and available for all cities globally, 'Geoscape' is a local Australian dataset developed using a mix of satellite and the advanced LiDAR technologies, with surface data at 2m resolution, and building data at mixed vertical accuracy of 0.1m and 2m and horizontal accuracy of 0.2 m and 2.5 m depending on the processing method ("Geoscape Australia," 2022; "Geoscape Buildings v2.0," 2020; "Geoscape Surface Cover v1.6," 2020). Using the Geoscape data, (Lipson et al., 2022) have developed a gridded morphological dataset at 300m resolution which was used in this study. An updated LCZ map based on the 2020 Geoscape data for Sydney (Sharma et al., 2025) was used as the base in the geo_em files of the three spatial datasets.

Table 2. The urban morphological datasets.

Dataset	Resolution	Type	Parameter derivation	Notes
Default WRF (IGBP-MODIS)	~927 m	Bulk urban – No local morphology	Lookup table in WRF (Skamarock et al., 2019)	Globally replicable
LCZ (WUDAPT)	100 m	Class-based – 10 urban classes	The default of W2W inferred from LCZ classes (Demuzere et al., 2022)	Globally replicable
WSF-MB	90 m	Gridded morphology	Explicit building and surface parameters from (Esch et al., 2022) and (*GlobalMLBuildingFootprints*, 2024)	Globally replicable
Geoscape	~0.1-2.5 m averaged to 300 m grids	Gridded morphology	Explicit building and surface parameters from (Lipson et al., 2022)	Australia-specific

We ingested the datasets into WRF using two Python packages: W2W (Demuzere et al., 2022) for the 'LCZ' case, and WRFUP (Gabeiras, 2025) for the 'WSF-MB' and 'Geoscape' datasets. Both packages interpolate and average the values of urban parameters from the original resolution of the urban morphological datasets to the model resolution – here 1 km – and directly enter the data into the WRF Preprocessing System (WPS) alongside the domain's geographical properties. This automation streamlines the process and reduces errors compared with classic table-based approaches.

3. Results and Discussion

3.1. Comparison of urban datasets

Before comparing the cases, we briefly describe how WRF represents urban land characteristics to provide context for the analysis. The Default WRF experiment represents limited urban land characteristics and no urban canopy model (UCM). With the UCM turned off for the Default case, the Noah-MP land surface model (LSM) becomes the main model representing the physics over urban areas, treating them as a special natural class with land cover characteristics assigned to mimic urban areas (see Section 2.2). Other WRF experiments use a UCM to work on the urban fraction of grids which are further described with morphological data including plan area density, building surface to plan area ratio, area-weighted mean building height, and building height histograms. Figure S1 shows the spatial maps of the first three for each dataset. Note that urban fraction and impervious fraction are interpreted interchangeably in the WRF UCMs (Salamanca et al. 2018).

Noah-MP land surface model (LSM) uses a tiling approach (considering bare soil and vegetated fraction, see Figure S2) to calculate fluxes for the natural surfaces (He et al., 2023). The UCM calculates them for the impervious urban surfaces. In the end, WRF takes the weighted mean of these fluxes in the urban (impervious) and natural fractions calculated by the UCM and LSM, respectively (Salamanca et al., 2018).

Now, we turn our attention to comparing the datasets. The Default dataset in WRF (i.e., IGBP-MODIS) has a bulk representation of the impervious fraction, assuming 100% imperviousness in urban grid points. The LCZ dataset represents Sydney with a limited distribution range, where impervious fraction mostly falls between 0.3 and 0.8. Gridded urban datasets (i.e., WSF3DMB and Geoscape), on the other hand, show more granular distributions over the city, with impervious fraction ranging from 0.0 to 1.0 (Figure 2).

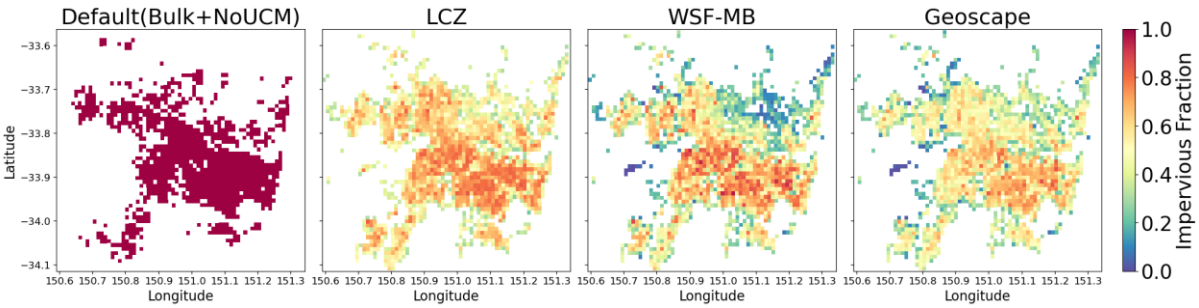

Figure 2. Spatial distribution of impervious fraction for four datasets describing Sydney, Australia.

Figure 3 compares the probability density function of impervious fraction, as well as plan area density, building surface to plan area ratio, and area-weighted mean building height across the

datasets (the Default case only has impervious fraction). Sydney's urban area covers 1629 km^2 surface area, mostly with relatively low impervious fraction, building coverage, and building height. Using the gridded Geoscape dataset, we find that half of Sydney's impervious fraction, plan area density, building surface to plan area ratio, and area-weighted mean building height fall under 0.48, 0.25, 0.31, and 6.43 m, respectively.

Compared with the locally acquired data of the Geoscape dataset, the LCZ case overestimates the values of all urban parameters, with median values of 0.60, 0.32, 0.66 (about twice the Geoscape value), 6.91m, in the order previously mentioned. This showcases how the class-based nature of LCZs with unified values per class, smoothing out variability, hinders the accuracy of morphological description. The WSF-MB case holds median values similar to Geoscape for impervious fraction and building surface to plan area ratio, while it has the lowest medians for plan area density and area-weighted mean building height valued at 0.14 and 5.09m, respectively. The numbers indicate higher and lower thermal mass over the city for the LCZ and WSF-MB cases, respectively, compared with the Geoscape.

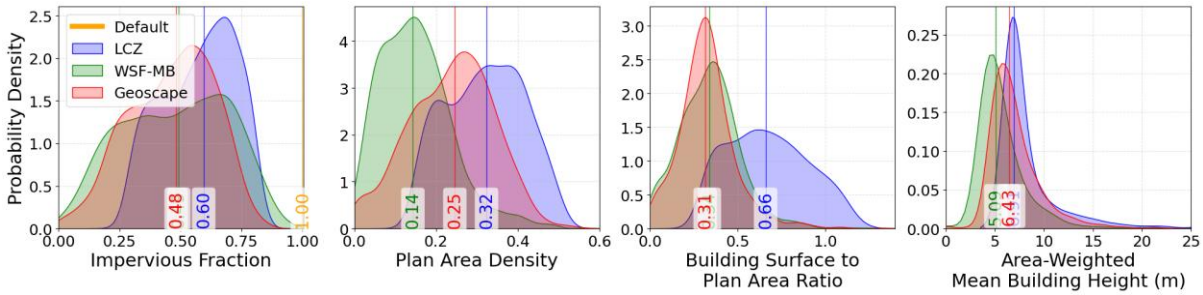

Figure 3. Probability density distribution of impervious fraction, plan area density, building surface to plan area ratio, and area-weighted mean building height (m) for the urban datasets of this study (see Figure S1 for the spatial distribution of the last three). The area under the curve equals to 1 or slightly less than 1 for the curves that extend beyond the x-axis limits. The probability density unit is dimensionless for the first three parameters and 1/m for the area-weighted mean building height subplot.

3.2. Comparison of predicted temperature with local observations

Sydney is a low-lying city bounded by the Blue Mountains in West, and the Pacific Ocean to the East. During the summer, land-sea breezes often develop, cooling the city from the east, while hot airflows come from the continental interior (west of Sydney). These hot flows initiated and maintained the heatwave days during the 10-day period, resulting in a steep temperature rise on 11, 13-14, and 17-18 January 2017 that later got cooled by southerly/easterly flows (Figure 4). Such patterns were also identified by (Hirsch et al., 2021). The interaction of these different flows resulted in up to about 15°C difference in the observed temperatures of the western and eastern sites during the 10-day period of this study (Figure 4 and S3-S5).

13-14 January stands out as an extended time period with large discrepancies between the experiments and observations in Figure 4. The wide range and strong spatial gradient of temperatures across the city might be a contributing factor. Such conditions are more difficult to simulate than calmer conditions, as the representation of the sea breeze and the locations of the selected weather stations would affect the discrepancies more than in weakly forced conditions (see Section 3.5).

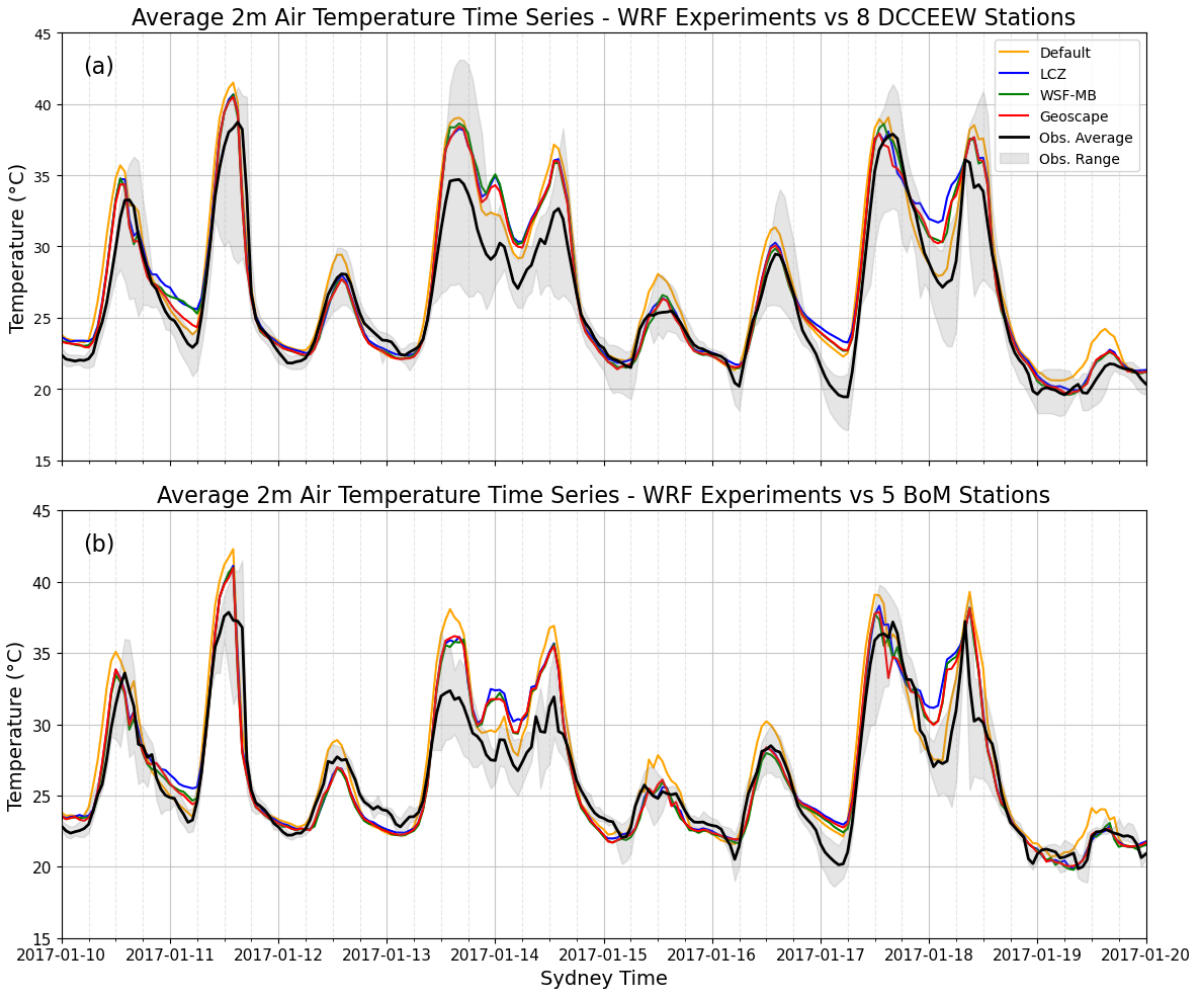

Figure 4. Time series of hourly mean 2 metre air temperature averaged over the 8 Department of Climate Change, Energy, the Environment and Water DCCEEW stations (a) and time series of instantaneous 2 metre air temperature averaged over 5 urban stations from Bureau of Meteorology BoM (b) in Sydney for observational data (solid black line) as well as the four WRF experiments (see legends). The shadowed area shows the range of observational data across sites (see Figures S3-S5).

Here we compare the modelled 2m temperature with local weather stations established across the city and quality controlled by the BoM and DCCEEW. There are 14 weather stations in the Greater Sydney region established by the BoM and 24 sites by the DCCEEW, out of which 5 and 8 have valid data that fall within the areas classified as urban in WRF grid points, respectively – see Table 3 for their locations and urban land characteristics. The grid corresponding to each station was used for comparing 2m temperature with the observations.

Following observing guidelines by (World Meteorological Organization (WMO), 2008), almost all of the weather stations are located at open spaces (Table 3). The DCCEEW stations are typically located in or close to large parks. Their corresponding WRF grid values for plan area density and area-weighted mean building height range from 0.15 to 0.38 and from 4.26m to 13.04 m, respectively. Not more urban than the DCCEEW sites, two of the five BoM stations are located at airports (plan area density = 0.06 and 0.01), two at a park and a racecourse, with only the Sydney Observatory Hill station falling within the high-rise, central business district (plan area density of 0.51 and area-weighted mean building height of 50.30m), albeit located on a hill that is surrounded by water bodies.

Table 3. The latitude, longitude, and satellite images ("Google Earth," 2025) *of the official weather stations from the Bureau of Meteorology (BoM) and NSW Department of Climate Change, Energy, the Environment and Water (DCCEEW) alongside their urban characteristics of the corresponding WRF grid (1km resolution) at each station location. The values of urban parameters are based on Geoscape (the most accurate scenario). The values other than the area-weighted mean building height are dimensionless. LCZ icons are based on* (Demuzere et al., 2020). *See the full names of the stations in the caption of Figure 1.*

	Station		**RK**	**RE**	**ED**	**CA**
DCCEEW	(latitude, longitude)		(-33.93, 151.24)	(-33.86, 151.16)	(-33.92, 151.14)	(-33.89, 151.05)
	500mx500m satellite image of the station					
	LCZ					
	Urban land properties as in Geoscape data (LiDAR and satellite)	Impervious fraction	0.69	0.28	0.38	0.52
		Plan area density	0.38	0.15	0.22	0.24
		Area-weighted mean building height (m)	8.90	7.10	6.00	13.04
		Building surface to plan area ratio	0.61	0.27	0.33	0.16
DCCEEW	**Station**		**LL**	**PT**	**CN**	**SS**
	(latitude, longitude)		(-33.93, 150.91)	(-33.79, 150.91)	(-34.06, 150.81)	(-33.80, 150.77)
	500mx500m satellite image of the station		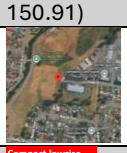			
	LCZ					
	Urban land properties as in Geoscape data (LiDAR and satellite)	Impervious fraction	0.59	0.52	0.51	0.43
		Plan area density	0.26	0.27	0.21	0.25
		Area-weighted mean building height (m)	5.06	4.83	7.38	4.26
		Building surface to plan area ratio	0.26	0.33	0.21	0.27
BoM	**Station**		**OH**	**SA**	**CR**	**OP**	**BA**
	(latitude, longitude)		(-33.86, 151.20)	(-33.95, 151.17)	(-33.91, 151.11)	(-33.85, 151.06)	(-33.92, 150.98)
	500mx500m satellite image of the station				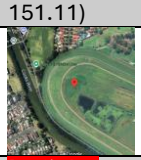		
	LCZ					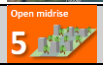	
	Urban land properties as in Geoscape data (LiDAR and satellite)	Impervious fraction	0.82	0.44	0.49	0.38	0.39
		Plan area density	0.51	0.01	0.25	0.18	0.06
		Area-weighted mean building height (m)	50.30	9.72	8.35	23.35	9.13
		Building surface to plan area ratio	2.32	0.03	0.41	0.49	0.11

Tables S1-S4 in Supplementary materials show the performance metrics – mean bias error (MBE), mean absolute error (MAE), and Pearson correlation – according to the DCCEEW mean temperature and mean relative humidity, and the BoM instantaneous temperature. The data are presented for each individual station as well as for a spatial average over all station locations, and averaged across all times as well as for five three-hour, diurnal periods: before sunrise (2-5

h), morning (7-10 h), peak solar heating (11-14 h), afternoon (15-18 h), and evening (19-22 h). Table 4 summarises the key differences in MBE and MAE across the four experiments for temperature data. Besides the total averages, representative diurnal periods and stations are selected that highlight the MAE differences between the experiments. The selection criterion prioritizes MAE over MBE to emphasize absolute prediction errors rather than directional biases. The analyses for relative humidity would be similar as below and we refer the reader to Figures S6-S8 and Tables S5-S7 for more information.

Looking at the DCCEEW data (Table 4), compared with the Default case, simulations using the Geoscape morphological data reduced mean bias error (MBE) by 0.51°C and mean absolute error (MAE) by 0.26°C averaged over the 10 days and 8 stations. The reductions in MBE and MAE using gridded datasets reached 1.43°C and 1.05°C, respectively, at peak solar heating hours (11-14 local time). The absence of 3D structures (i.e., no shading) in the Default led to higher difference at peak solar hours. Spatially, Campbelltown CN (the second most western site) is the station where most differences of MAE between the two experiments happened, with a 10-day average value of 0.45°C and 1.26°C at all times and peak solar heating hours, respectively. Knowing the western parts of the city and peak heating times experienced the most intense heat, an adequate urban representation could therefore benefit people where and when they are most vulnerable by estimating more accurate temperatures. The total averages do not reveal this part of the story.

The BoM temperature metrics, showing similar figures and trends in the differences between the Default and Geoscape case further confirm these findings. We observe negligible average temperature differences between Default-Geoscape experiments (MBE and MAE of 0.52°C and 0.17°C) that reached MBE and MAE of 1.69°C and 1.08°C during peak solar heating. Here, again the most western station (Bankstown Airport) shows higher MAE of 1.38°C at peak solar hours.

Table 4. The mean bias error (MBE) and mean absolute error (MAE) values of the modelled temperature for the four experiments compared with the observations from the NSW Department of Climate Change, Energy, the Environment and Water (DCCEEW) stations (hourly mean temperature); and comparisons with the Bureau of Meteorology (BoM) stations (instantaneous temperature). The 10-day temporal averages are shown as well as averages at peak solar heating hours (11-14) and before sunrise (2-5). For each period, the spatial averages over the 8 DCCEEW and the 5 BoM stations (All) are shown as well as metrics at one station with large differences between the experiments: Campbelltown station (CN) and St Marys station (SS) from DCCEEW and Bankstown Airport station (BA) from BoM.

10-day Average Errors

	Hourly mean temperature (compared to DCCEEW)				Instantaneous temperature (compared to BoM)			
	MBE °C		MAE °C		MBE °C		MAE °C	
Experiment	All	CN	All	CN	All	BA	All	BA
Default	1.34	2.10	1.75	2.24	1.01	1.57	1.69	2.02
LCZ	1.11	1.77	1.62	1.96	0.63	1.34	1.61	1.91
WSF-MB	0.89	1.70	1.55	1.89	0.41	0.99	1.53	1.75
Geoscape	0.83	1.55	1.49	1.79	0.49	0.76	1.52	1.7

10-day Average Errors for Peak Solar Heating (11-14 h)

	Hourly mean temperature (compared to DCCEEW)				Instantaneous temperature (compared to BoM)			
	MBE °C		MAE °C		MBE °C		MAE °C	
Experiment	All	CN	All	CN	All	BA	All	BA
Default	3.01	3.17	3.02	3.18	2.88	3.1	3.01	3.27
LCZ	1.72	1.75	2.02	1.99	1.19	1.77	2.01	2.07

WSF-MB	1.60	1.97	1.94	2.06	1.03	1.46	1.95	1.96
Geoscape	1.58	1.63	1.97	1.92	1.19	1.5	1.93	1.89

10-day Average Errors for Before Sunrise (2-5 h)

	Hourly mean temperature (compared to DCCEEW)				Instantaneous temperature (compared to BoM)			
	MBE °C		MAE °C		MBE °C		MAE °C	
Experiment	All	SS	All	SS	All	BA	All	BA
Default	0.95	2.48	1.34	2.54	0.55	1.58	1.33	1.74
LCZ	1.75	3.47	1.99	3.49	1.39	2.56	1.91	2.73
WSF-MB	1.38	3.08	1.73	3.12	1.06	1.99	1.67	2.27
Geoscape	1.27	2.76	1.62	2.81	1.05	1.61	1.63	1.99

Comparing the urban classification method (LCZ) with gridded datasets shows that the temperature differences between them are more modest than the Default-Geoscape differences (Table 4). The accuracy gain for using Geoscape over LCZ at DCCEEW observation sites is 0.28°C for MBE and 0.13°C for MAE when comparing the 10-day mean. However, the differences vary throughout the day. We find that before sunrise (2-5 h) is the period with most differences, when the Geoscape improvements over the LCZ for MBE and MAE reached 0.48°C and 0.37°C, respectively. Focusing on the localised effects of different stations, particularly in Western Sydney where most differences between the experiments happened at St Marys SS (the westernmost DCCEEW site), we find that the average MBE and MAE differences before sunrise reached 0.71°C and 0.68°C.

Overall, the gridded experiments, WSF-MB and Geoscape, performed similarly. Their 10-day spatial average differences in MBE and MAE remain at about 0.1°C and less regardless of the diurnal period (also see Table S1). And their localised MBE and MAE differences across all DCCEEW stations and the 5 diurnal periods, including before sunrise, do not exceed 0.42°C (also see Table S2).

The higher differences between the experiments before sunrise suggest that the local characteristics might play a more important role at night (including 2-5 h). The high temperatures of the LCZ at night (10-day averaged MBE and MAE of 1.75°C and 1.99°C before sunrise) can be attributed to an overly built morphology with higher thermal storage (see Section 3.1), more trapped longwave radiation in the canopy (affected by 3D building characteristics), in addition to having the lowest wind speeds among all experiments (see Section 3.3 and Figure 8). The BoM data analysis further confirm these findings (Tables 4 and S3).

Table 4 and Tables S1-S3 also show that the Default case had a marginally better performance before sunrise at most sites – with a 10-day, spatially averaged MBE and MAE of 0.95°C and 1.34°C compared with 1.27°C and 1.62°C values for Geoscape. For the same reason (absence of 3D urban structures) that the Default case excessively heated up at peak hours, it cooled down faster, this time to its benefit due to the overall overestimation of temperature in WRF. While the numbers shown are from DCCEEW data, BoM data show similar figures.

In summary, WRF performed best when implementing locally informed, gridded, urban datasets (i.e., Geoscape), closely followed by the global dataset of WSF-MB. The Default experiment showed the poorest performance, highlighting that implementing any building-descriptive dataset (here shown for class-based and gridded – either satellite-based or more advanced LiDAR-based) would perform better than the default of WRF, particularly at the hottest times

and places. Any spatial dataset improved the Default temperature accuracy by at least 1.29°C for MBE and 1°C for MAE on average at peak solar heating (Table 4). Furthermore, WSF-MB and Geoscape outperformed LCZ's temperature MBE and MAE predictions before sunrise by up to 0.48°C and 0.37°C on average, respectively, showing their superior performance at nighttime. Note that while urban morphology substantially reduces temperature errors (especially at peak heating), a residual model bias remains due to larger-scale model physics and forcing, which urban data alone cannot resolve.

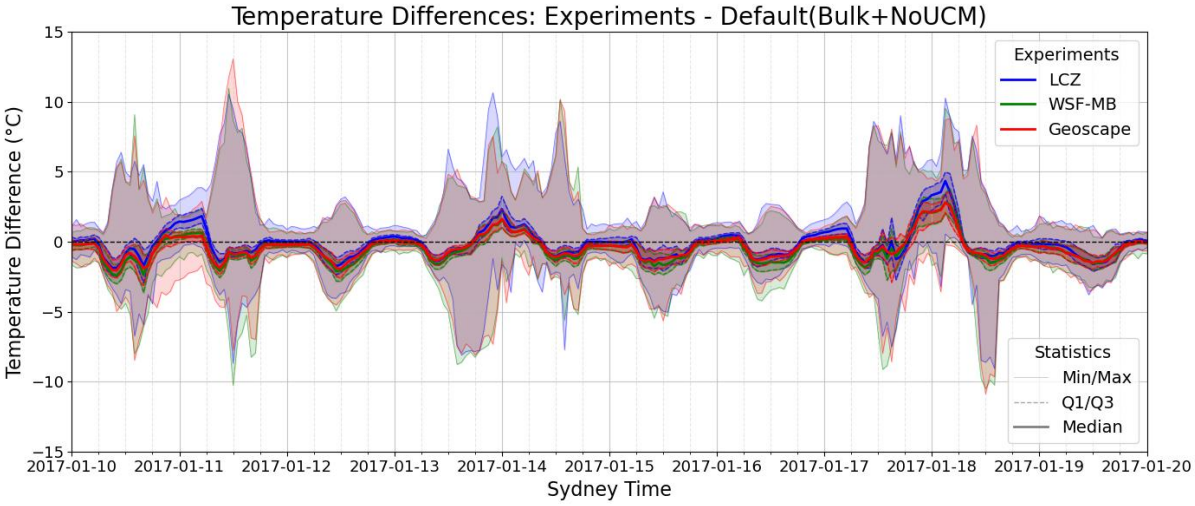

Figure 5. Statistical distribution of instantaneous temperature differences of the LCZ, WSF-MB, and Geoscape experiments with the Default case at all the spatial points during the simulation period. The five lines for each experiment specify the minimum, maximum, first quartile, median, and third quartile.

Before closing this Section, we want to present how average differences translate into the point- and hour-based predictions as well as a classic objection about comparisons with observations in urban climate modelling. Starting with the former, going beyond temporal and spatial averages, a closer look at the range of temperature differences between the experiments at all times and places reveals temperature differences of up to 13°C (11 January at 12 h) and several instances of 5+°C between the experiments (Figure 5). Additionally, the median temperature differences reached 2-4.5°C (late night and early hours of 17 and 18 January). It is a reminder that spatially and temporally averaged analysis does not provide a complete picture. In this case, most of the top differences were located in coastal areas and can be attributed to the different rates of the progression of sea breezes or cold fronts (see Figure S8 and Table S7).

While comparison with measurements is a key method for assessing the accuracy of experiments, there are key limitations that affect the interpretation of such results in an urban context. First, a spatial mismatch occurs between the simulated grid-averaged (~ 1 km^2) air temperature and the point-based observed air temperature. Second, the open spaces (parks or airports) in which almost all of the weather stations are located does not represent the conditions within the urban canopy. Finally, when it comes to thermal comfort analysis, temperature is just one of the four environmental contributing factors and not the most locally dependent.

For the reasons outlined above, relying on the evaluations with weather stations available in Sydney does not give a full picture of the differences between the urban scenarios, necessitating the spatial comparisons in the next section.

3.3. Temporal evolution of 10-day averaged spatial maps of selected variables

As seen in Table 3, the weather stations within our urban domain are not representative of urban canopy conditions across Sydney. Here, we detail inter-experimental differences in the spatial maps of 2m air temperature, wind speed and direction, and mean radiant temperature, drawing attention to the temporal processes during the 10-day period (Figure 6-9). The spatial maps of the universal thermal climate index (UTCI), a thermal comfort index combining these microclimate parameters, further adds insight on human exposure to heat (Figure 10).

The 2m air temperature maps show a cool-warm gradient from east to west over Sydney that became more pronounced during the day as the land warms up. Strong sea breezes then cooled down the entire city by the end of the day. Compared to the other three experiments that show fairly similar patterns, the Default case warmed up faster in the morning (~30-31°C in central western parts, about 2°C higher than the other three experiments), showed higher temperatures at peak (reaching 34+°C temperatures in central areas unlike the other cases), and cooled down slightly faster in the evening (especially in central-west areas reaching ~25°C, about 1-2°C cooler than the rest of experiments), due to the absence of 3D structures in its urban description – i.e., no longwave radiation trapping at night, and no shading during the day.

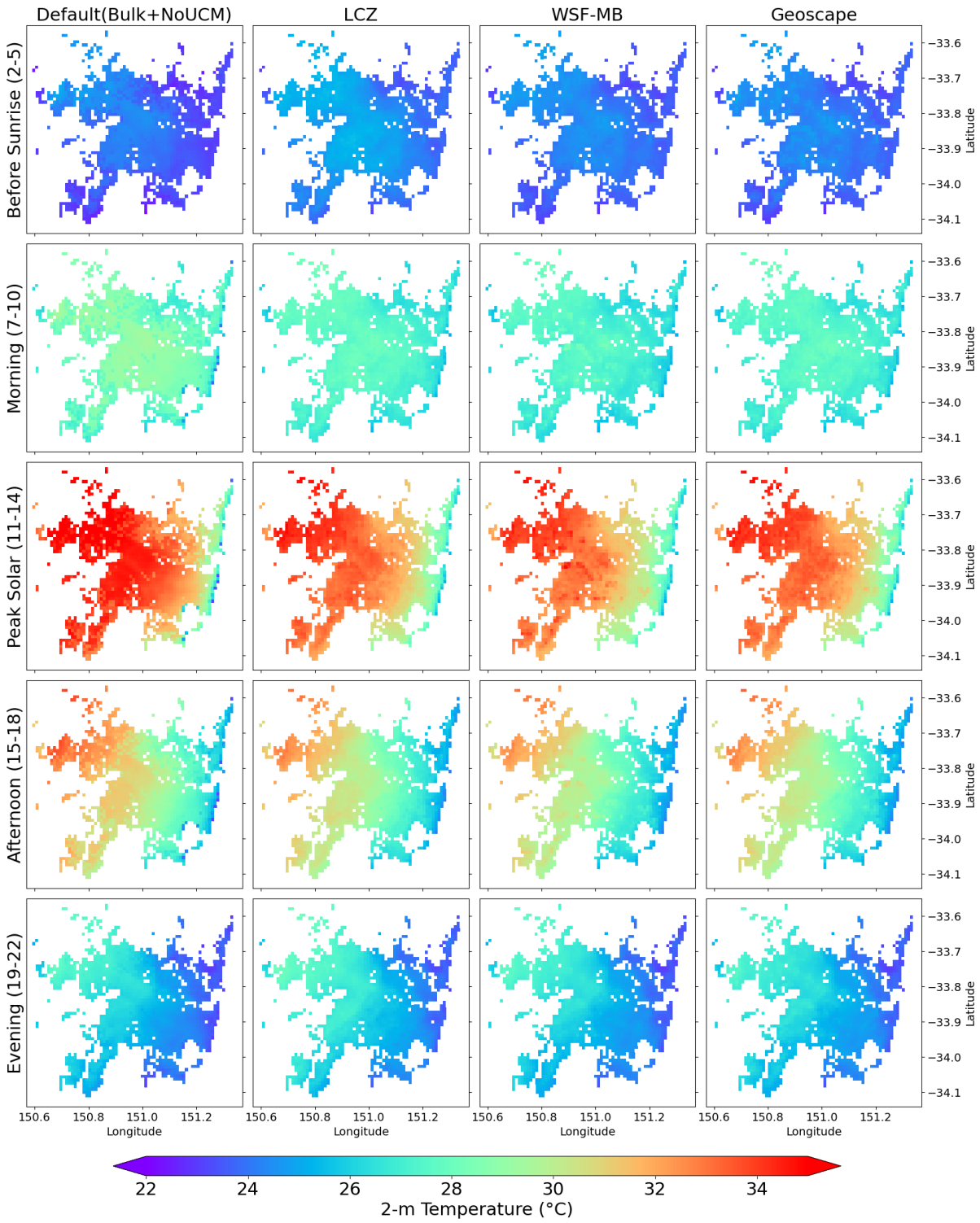

Figure 6. The temporal evolution of 2m air temperature spatial maps for the four experiments.

The wind plots (**Error! Reference source not found.**Figure 8) better describe the cooling mechanism of sea breezes for a coastal city like Sydney. During the day, solar radiation warmed up the land more quickly than the ocean due to their difference in heat capacity. This difference in temperature triggered sea breezes resulting from the convection of the cool air from the ocean to the land. Figure 7 shows how the dominant winds from north- and south-east before sunrise gave way to sea breezes coming from the east and opposing dry hot winds from western inner land areas at the peak heating hours. From the peak hours through to the evening, sea

breezes then became more dominant (almost all wind coming from the eastern sides and eventually north- and south-east) cooling down the city.

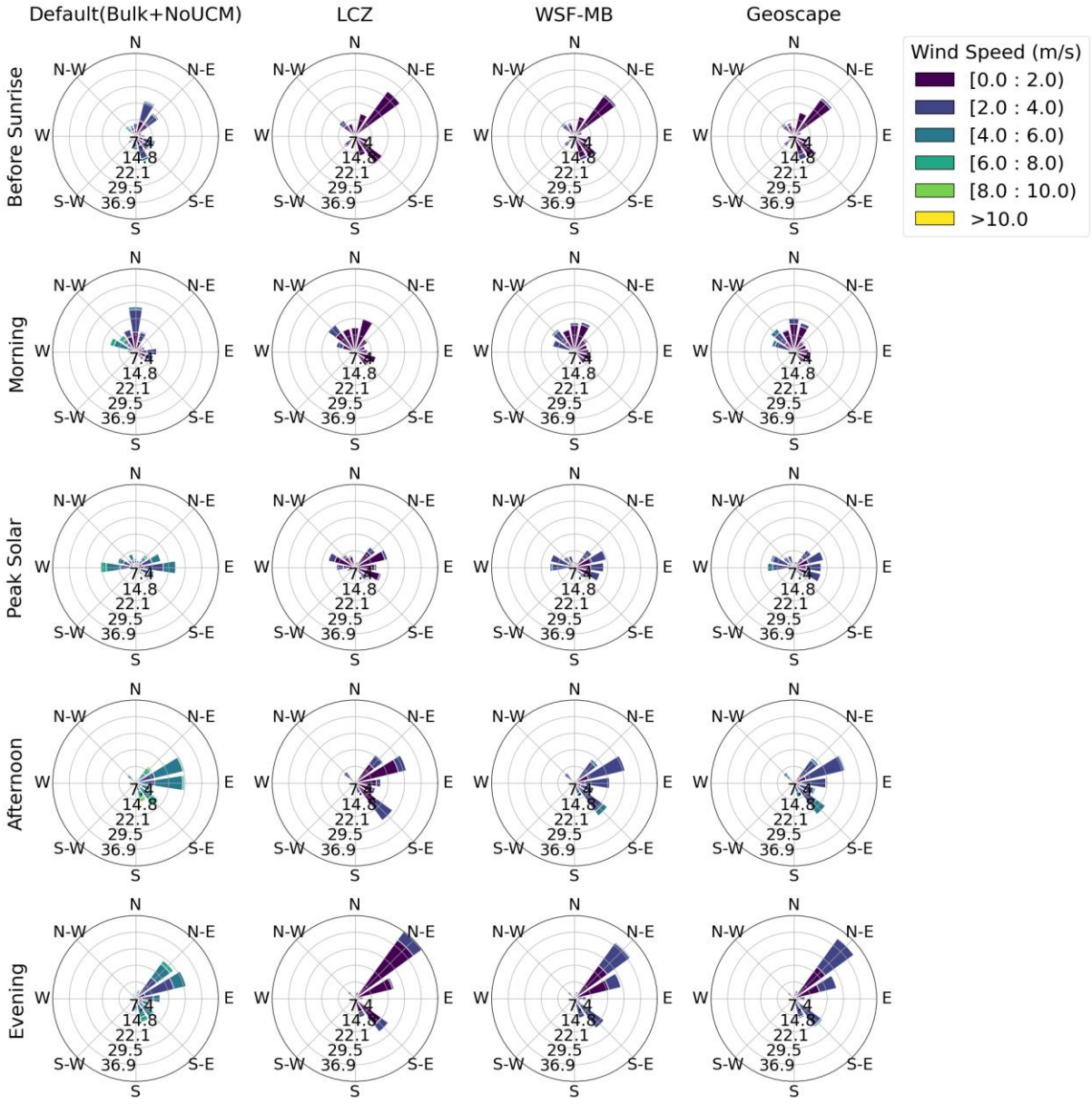

Figure 7. The temporal evolution of windroses over the Sydney domain for the four experiments.

Comparing the wind speed maps between the experiments (Figure 8), the highest wind speeds happened in the afternoon, within the range of ~4-8 m/s over urban areas for the Default case, ~2.5-5 m/s for the gridded WSF-MB and Geoscape experiments, and only ~1.5-3 m/s for the LCZ case (see Figure S8 for wind speed time series). Figure 7 further shows that wind speed and direction in the Default case is most distinct, while being more consistent across the other three experiments. Most variability in wind direction is observed during morning hours (hot air coming from north and west and onset of development of sea breezes from the east) and peak hours (the hotter inland air coming from the west and cool sea breezes coming from the east).

In contrast, evening had the least variability in wind directions, with northeastern winds dominating. This dominance was more pronounced in the spatial cases (~30-37% fraction of the winds) that channel an extra 9-16% of winds from this direction compared with the Default

case (~21%). The strong dominance of certain wind directions in the evening – unlike the more varied daytime patterns – can be explained by the absence of solar-induced convection phenomena. In particular, the reason why wind is more dominant in spatial cases can be explained by the presence of urban structures that channel winds along specific pathways. In this case, urban developments in southeastern Sydney (areas with high plan area density in Figure S1) likely blocked winds from east-to-south directions that would otherwise occur in the Default case.

The representation of urban areas has a significant effect on local wind, sensitive to local aerodynamic characteristics. The impact of homogeneous land characteristics on the wind speed map is clearly noticeable in the Default case, with a constant urban roughness length of 1m in contrast with half of buildings having an area-weighted height above 5m for all other cases (Figure 3). The higher plan area density of the LCZ case (Figure S1) has led to higher drag coefficients (Figure S10) – see (Gutiérrez et al., 2015; Lu et al., 2024; Nazarian et al., 2020; Santiago and Martilli, 2010) – which in turn resulted in lower wind speeds over urban areas. The other two cases show granular patterns matching their granular urban distributions (Figure 2 and S1). This particularly manifests itself in the Geoscape case, where wind speed differences between two neighbouring grids reached 2.5 m/s at peak hours (1 and 3.5 m/s) and 2+ m/s in the afternoon (2.5 and 4.5+ m/s).

Going beyond urban areas, the differences between the experiments become negligible in the entire nested domain (Figures S11 and S12), as wind is highly dependent on local characteristics.

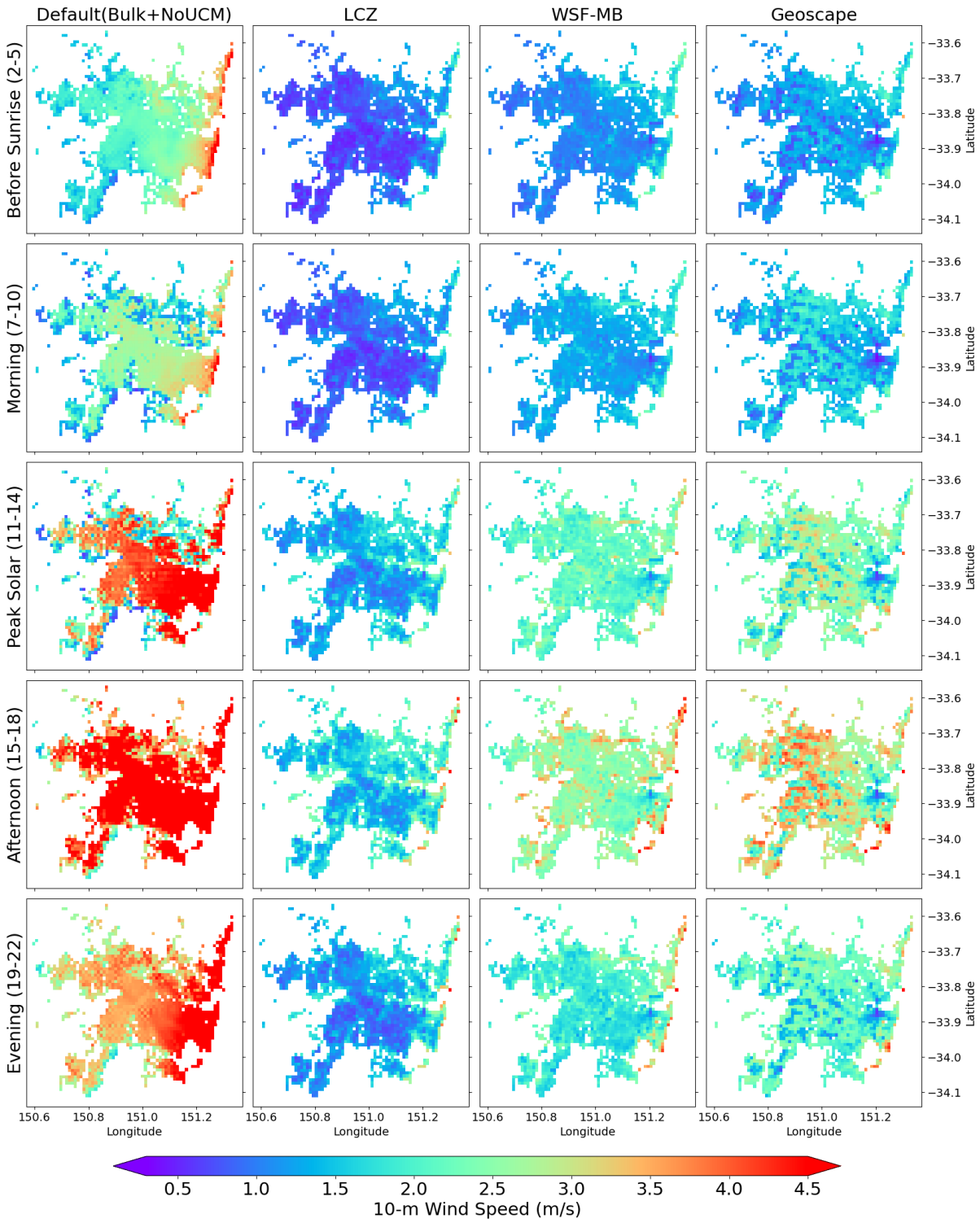

Figure 8. The temporal evolution of wind speed spatial maps for the four experiments.

Another locally dependent property is the mean radiant temperature (MRT), which is a function of the temperature of urban surfaces. In WRF-Comfort, two street directions (N-S and E-W) and three pedestrian positions (sides and centre) are considered, resulting in 6 MRT values. One MRT value was calculated for the Default case using the thermofeel package (Brimicombe et al., 2022), assuming full sun exposure. Only one value since there is no urban canopy in the Default case and the only surface is concrete-like ground. Here, the maximum of the 6 MRT values of

LCZ, WSF-MB, and Geoscape are considered as the value comparable with the one fully sun exposed value of the Default case (Figure 9).

Figure 9 compares MRT values for four experiments. With full exposure to the sun (and no urban canopy), the Default case mostly stayed in the range of 45-55°C during the day (7-18 h). This range was wider for LCZ (35-50°C) and the gridded (45-60+°C). At peak heating hours, LCZ, WSF-MB, and Geoscape cases were quite similar, mainly ranging between 45-50°C, while the range was higher by 5°C for the Default case. In the morning and afternoon, the LCZ case generally stayed in the 35-45°C range of MRT, compared with the ~52-60+°C values of the gridded and ~46-52°C of the Default.

As MRT depends on surface temperatures, building surface to plan area ratio plays a particularly influential role in MRT values, since this parameter is key in determining the street width and thus shadowing. The remarkably higher values of surface to plan area ratio of the LCZ compared with the gridded data – LCZ's median of 0.66 being double those of the gridded (see Section 3.1, Figure 3 and S1) – has led to its stark MRT differences. This characteristic of the LCZ added to its higher plan area density and building height created more shading (i.e., lower MRTs) in the morning and afternoon hours (when solar radiation is angular) and trapped more longwave radiation within the canopy at night when LCZ's MRTs were slightly higher.

The gridded cases were again similar, except for the low ~35°C MRT values in the northeastern parts of the WSF3D case and the ~40°C patches in the hot 60+°C western parts of the Geoscape case in the morning and afternoon. Both observations have a quite direct relation with their land characteristics: the former can be explained by the low plan area density in the northeastern parts of WSF-MB (Figure S1), and the latter by the high-albedo areas in the western parts of Sydney (Figure S13).

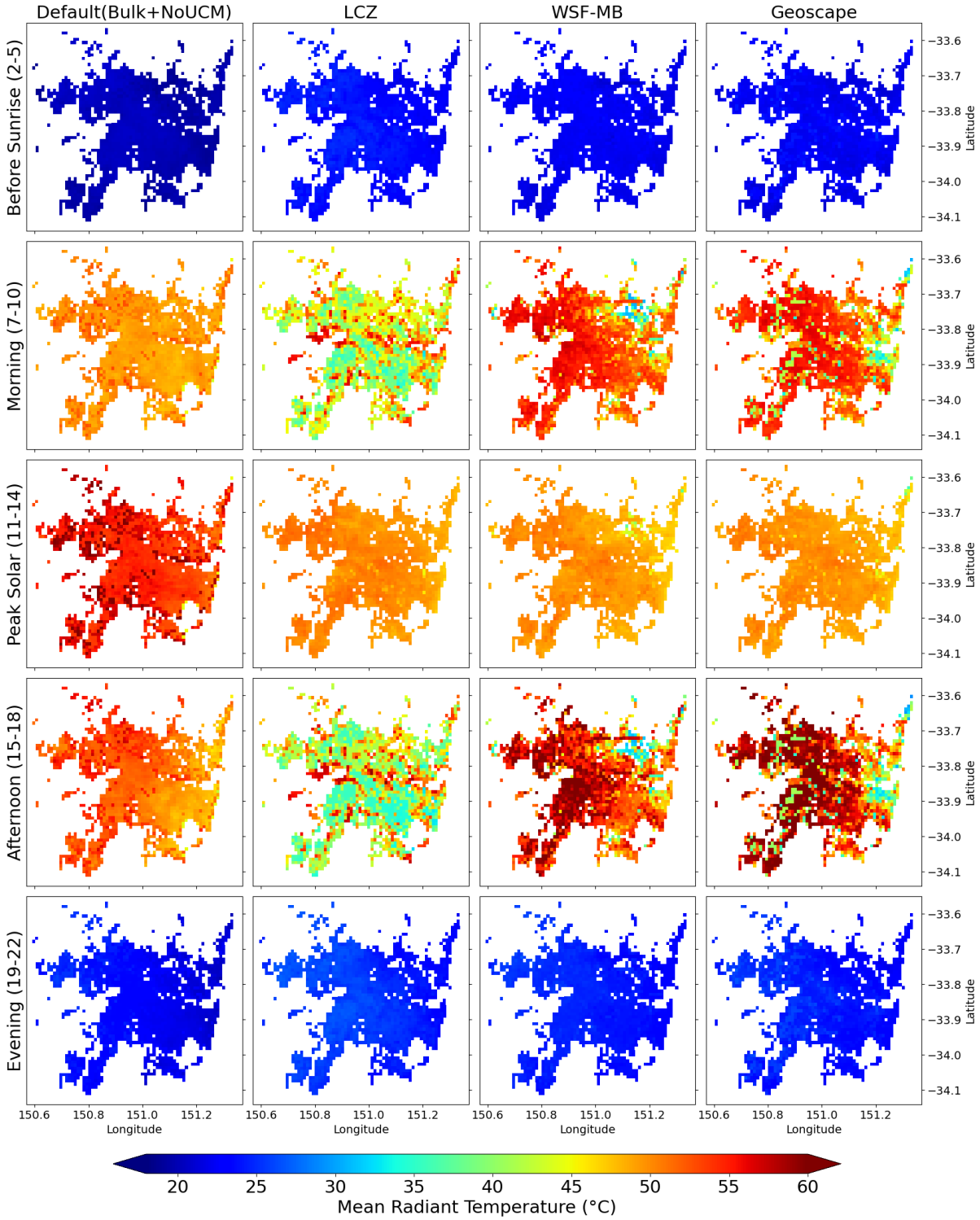

Figure 9. The temporal evolution of mean radiant temperature spatial maps for the four experiments. The Default case has only one value with the assumption of full exposure to the sun and no shade. The maximum of the 6 MRT values is shown for the other experiments.

The universal thermal climate index (UTCI) maps are derived from 2 m air temperature, wind speed, mean radiant temperature, and absolute humidity (Figures 6-9, S14, and S15).

UTCI is the equivalent air temperature that an individual would experience under reference environmental conditions (10m wind speed of ~0.5 m/s, mean radiant temperature equal to air temperature, and relative humidity of 50%) and a reference activity level (walking at 4 km/h outdoors). The reference conditions are chosen to be relevant across different individuals and climate contexts (Błażejczyk et al., 2013). The UTCI range of 9-26°C correspond to no thermal stress, and the values outside this range fall into stress categories that elicit certain physiological responses, e.g., sweat rate, skin temperature, and total net heat loss. Increased UTCI in summer is associated with immediate rises in morbidity and in strong cases, mortality (Di Napoli et al., 2018; Ghada et al., 2021).

Looking at the distribution of stress categories for UTCI hot spots (Figure 10), strong and moderate heat stress were dominant during the day. The UTCI Cool Spots maps (Figure 10) show that although there was an escape from such conditions to neutral ones in the eastern suburbs, Western Sydney was locked in heat stress. Most differences between the experiments happened in the west. LCZ had higher values in the west at peak hours reaching very strong heat stress in northwestern parts. But its ~30°C values in the morning and afternoon were ~4-5°C lower than the gridded (see Figure S16) because of more building shading, similar to the MRT patterns.

The UTCI hot spots patterns of the gridded experiments closely follow those of the average of MRT values (Figure S14). While for LCZ, its considerably lower wind speed values (Figure 8) were also influential, especially in its higher UTCI values at the peak hours (very strong heat stress). Note that the average MRT values follow the general patterns of maximum MRT (Figure 9) discussed in the previous paragraphs, with one notable difference: the highest values of MRT happened at the peak solar heating hours in the former (~45°C) and in the afternoon in the latter (~60°C).

Here, we further emphasize how basing analyses on different heat indicators can lead to different outcomes. While the 2m air temperature spatial maps demonstrated little differences between the LCZ, WSF-MB, and Geoscape cases (Figure 6), the UTCI hot spots maps showed otherwise. At nighttime (before sunrise and evening), Sydney was dominated by neutral heat stress in the gridded cases while a large part of the city (in western suburbs) was under the moderate heat stress risk in the LCZ case. On the other hand, the LCZ case missed the strong heat stress of the gridded cases in the west for the most part during the morning and afternoon. These differences can signal different levels of preparedness in the face of heatwave events.

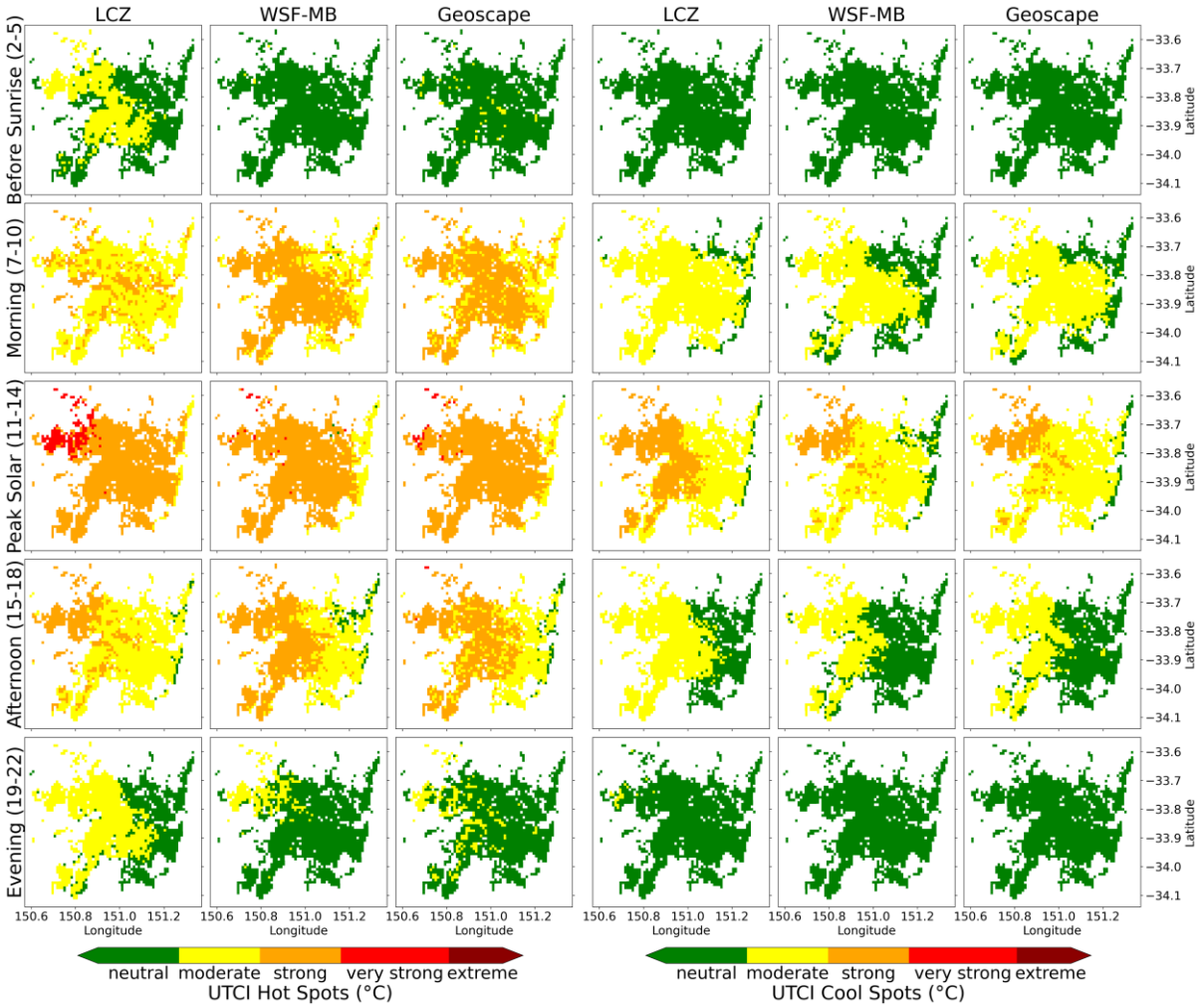

Figure 10. The temporal evolution of the universal thermal climate index (UTCI) spatial maps for hot spots (left) and cool spots (right) for the four experiments. The UTCI stress categories correspond to the following UTCI values: no thermal stress (neutral) = 9-26°C, moderate = 26-32°C, strong = 32-38°C, very strong = 38-46°C, and extreme heat stress = 46+°C. UTCI hot spots represent the tenth highest percentile of 54 sub-grid values that WRF-Comfort calculates for each grid, while UTCI cool spots represent the tenth lowest (see Section 2.1).

3.4. Heat exposure analysis

Here we compare the probability density function of 2m temperature, UTCI hot and cool spots to highlight the implications of different urban datasets on various microclimate parameters (Figure 11 and S17).

In nighttime hours (before sunrise and evening), a narrower UTCI and temperature range had higher probability densities compared to daytime hours (morning, peak, and afternoon) – see Figure S17. For instance, before sunrise, UTCI hot spots had a probability density of ~0-0.15 across a ~16-35°C range, with half the data falling within ~16-24°C. In contrast, afternoon UTCI hot spots showed a reduced probability density of ~0-0.05 across a wider ~16-52°C range, with half the values between 31-52°C according to Geoscape (Figure 11).

The majority of Sydney experienced the highest values of UTCI hot spots, UTCI cool spots, and temperatures during peak solar heating when the sun reaches its highest point, with medians of 35.3°C, 31.0°C, and 32.2°C (Geoscape), respectively. A similar pattern emerged for UTCI cool

spots. However, there was a notable ~7°C difference between the medians of UTCI cool spots and UTCI hot spots in both morning and afternoon hours (when angular solar radiation creates shaded shelters against heat across the city). This difference narrowed to ~2-4°C before sunrise, at peak, and in the evening.

For the present heatwave study, the variation in heat exposure severity estimates across different experiments is of particular interest. Before sunrise was the period when the experiments varied most in their estimated probabilities of the most critical 2m temperatures, with the LCZ case showing a probability density of 0.04 for 34.5°C air temperature – four times higher than Geoscape (Figure S17). Similarly, the probability of the most critical UTCI hot spot values varied most before sunrise, when the LCZ case overestimated the probability of strong heat stress (0.05) by approximately five times compared to the other two experiments. During morning and afternoon periods, the experiments diverged in their estimates of alarmingly high UTCIs, with the LCZ case underestimating very strong and extreme heat stress by factors of two and four, respectively.

The UTCI probability density plots demonstrate how urban canopy characteristics can alter the severity of heatwaves within the urban canopy, while temperature plots only slightly capture these differences arising from the microscale land characteristics (Figure S17). If emergency warning systems were to use heat maps based on LCZ land description (that includes less intra-urban variability), its underestimation of heat stress severity could have significant consequences. Since UTCI is highly dependent on urban morphology, the more accurate morphology data of WSF-MB and Geoscape should lead to better UTCI predictions.

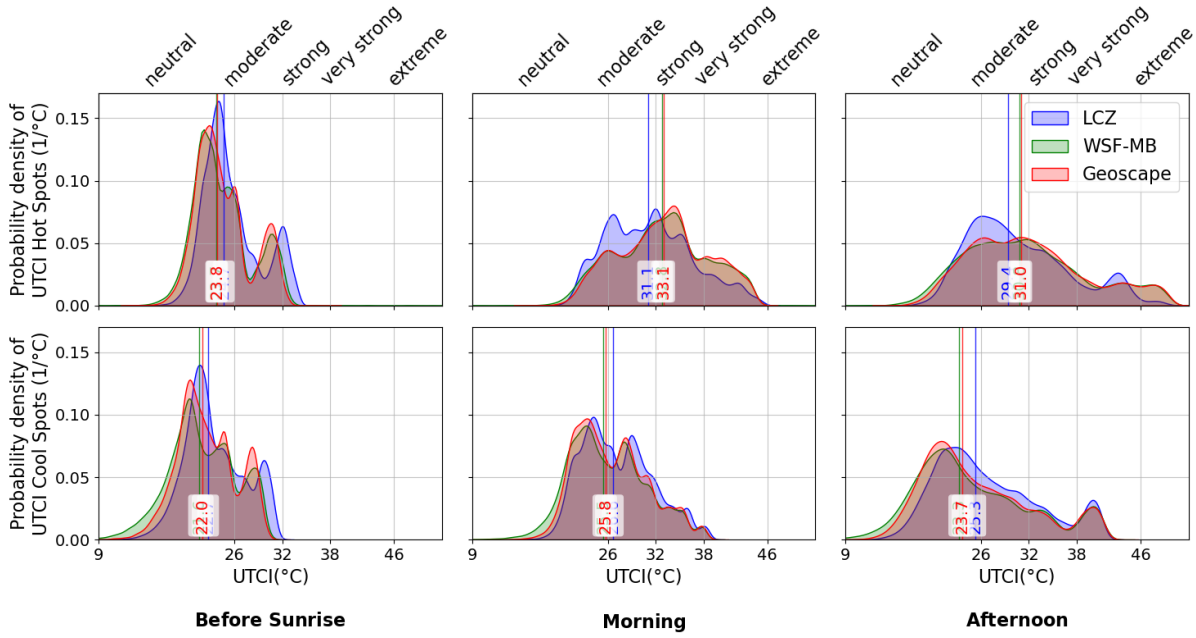

Figure 11. Probability density distribution of UTCI hot spots and UTCI cool spots before sunrise, in the morning and afternoon (rows) for the LCZ, WSF-MB, and Geoscape cases. The area under the curve equals to 1.

Here we evaluate another heat exposure metric. Average UTCI exceedance is a heat metric taking into account both intensity and duration of exposure to heat exceeding the neutral UTCI threshold of 26°C (Sadeghi et al., 2021). Summing up all the exceedances ∑ΔUTCI (°C.h) and dividing it by the number of exceedance hours gives average UTCI exceedance.

The average UTCI exceedance spatially averaged over the urban domain for LCZ, WSF-MB, and Geoscape were 7.10°C, 7.70°C, 7.64°C, respectively, further showing LCZ's underestimation of heat severity. Location-wise (Figure 12), the eastern suburbs influenced by the breezes from the Pacific Ocean retained relatively low average exceedances, while experiments differed by 2-3°C in their estimates in Western Sydney. Morning and afternoon MRT and UTCI patterns (Figure 9Figure 10) dominate the average UTCI exceedance maps: LCZ's lower values in the West and Geoscape's patches of low exposure (see Section 3.3). This could be expected as morning and afternoon comprise 2/3rd of the daytime hours (6 hours out of 9) with mostly moderate and strong heat stress categories.

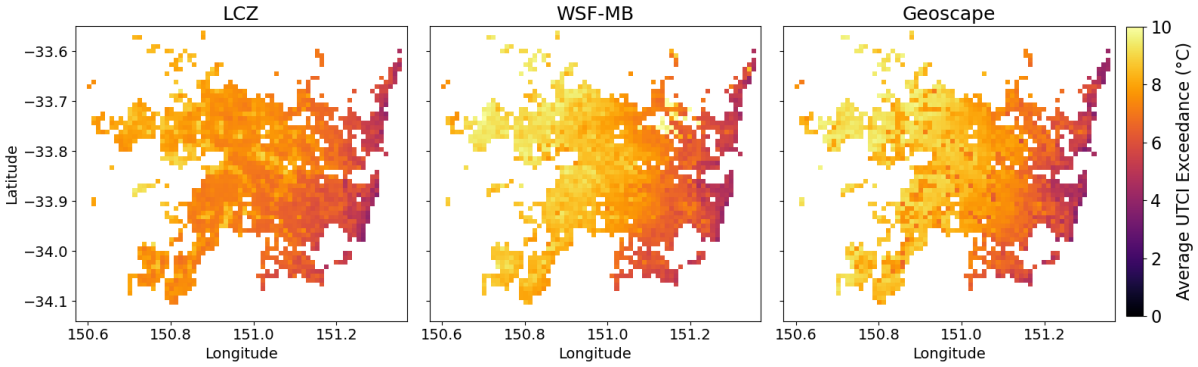

Figure 12. Spatial distribution of average UTCI hot spots exceedance, ∑ΔUTCI/H (°C), during 10-20 January 2017 for LCZ, WSF-MB, and Geoscape.

While Figure 11 depicted when the experiments differed in their estimations of heat intensity, Figure 12 showed where most of these inter-experimental differences happened. The differences between the LCZ and gridded cases can be explained by the previously described overestimation in the LCZ's urban land description, which includes significantly higher plan area densities and building plan-to-surface area ratios, in addition to the experiments' differences in albedo maps (Figures S1 and S13). These all return to the fact that the LCZ dataset smoothens the morphological variability within the city, leading to erroneous estimates. Beyond predictive accuracy, the 2-3°C difference in average exceedance is indicative of the potential of the interventions targeting urban morphological characteristics.

3.5. Varying degrees of synoptic forcing and the urban effect

Heatwaves initiate from synoptic phenomena beyond urban areas. How urban characteristics can affect their unfolding in cities depends on how strong the synoptic forcings are. Two snapshots from 13 January and 17 January 2017 illustrates this point. On 13 January 2017, 15:00 AEST, a hot north-westerly opposing a strong, cool north-easterly determined the temperature patterns (a large fraction going to alarming 40+°C temperature values and very strong heat stress) regardless of the urban representation. With weaker synoptic forcings on the 17th, however, each case had its own distinct local patterns which can be explained through the wind patterns (see Figure S18 for the difference in synoptic forcings of the two days).

On both snapshots, the LCZ experiment showed the lowest wind speeds (and the Default had the highest, see Figure S19 and Figure 8). On the 13th, the gridded cases showed quite similar wind patterns, while on the 17th, the local processes of the Geoscape case had stronger cooling

mechanisms leading to 3+°C temperature differences (and larger strong/very strong fraction) with the WSF-MB in central to eastern parts of the city.

Here, we can better see that although the overall patterns were the same under the strong synoptic conditions of 13-14 January, how each experiment captured the strong spatial gradients of temperature and varying degrees of sea breeze advancement can lead to

substantial temperature and UTCI differences for a particular location (see Figure 4-5 and Section 3.2).

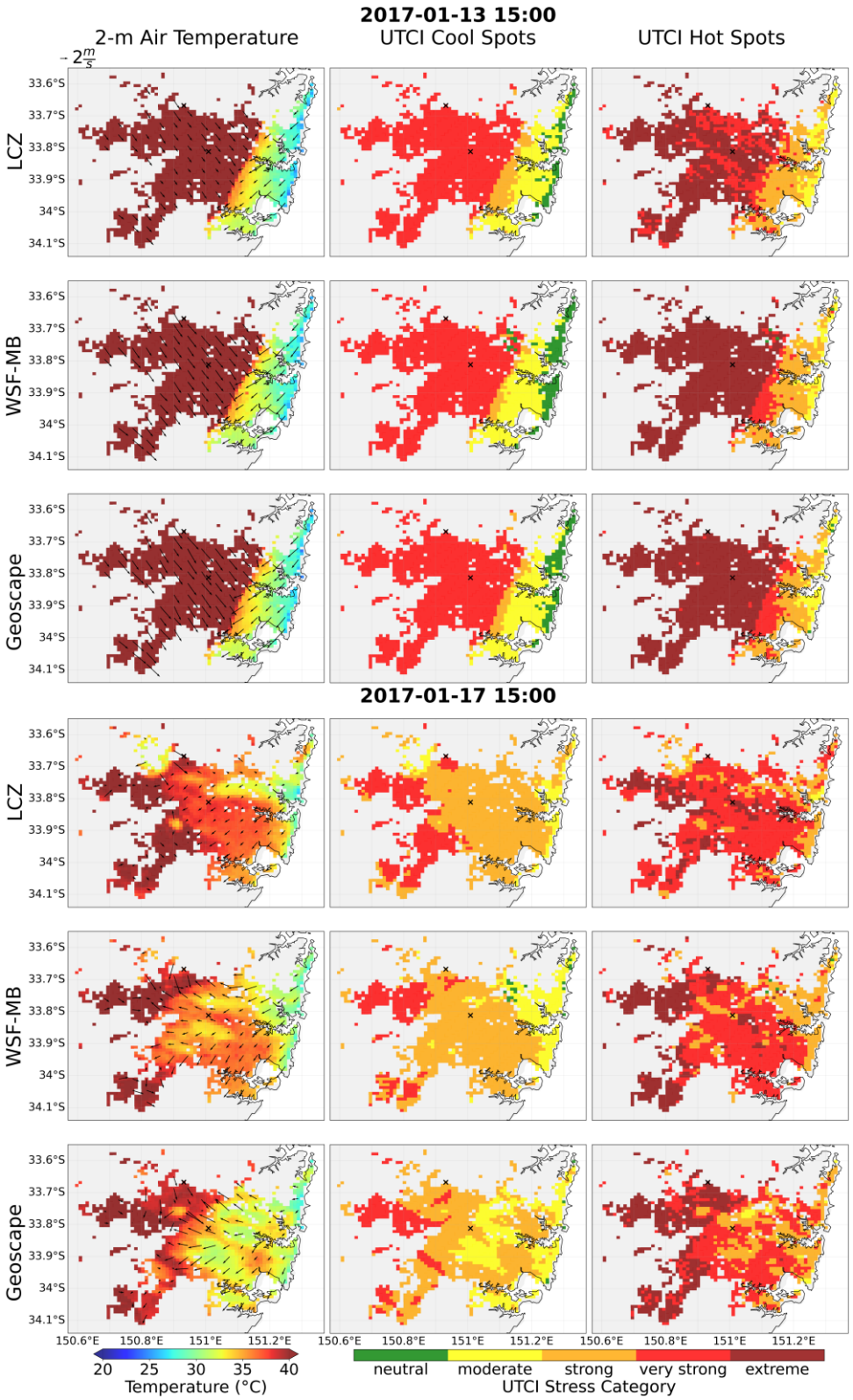

Figure 13. Snapshots of temperature maps with wind vectors on top and UTCI cool and hot spots maps for the LCZ, WSF-MB, and Geoscape experiments on 13 January 2017, 15:00 AEST (top), and 17 January 2017, 15:00 AEST (bottom). When strong synoptic forcings are in effect, the representation of urban areas plays a less significant role in determining the overall patterns of a heat extreme.

Even during a period strongly affected by synoptic forcing, considerable differences might be expected at high-built and hot locations. We picked a point at the high-built areas of Paramatta – one of the most heat-vulnerable suburbs in Sydney – and compare three of its time series with a low-built point around the same longitude to maintain similar weather phenomena (considering the east-west temperature gradient of Sydney) – see Figure 13 for their locations (central x referring to the high-built point and upper x to the low-built).

According to Geoscape (at 1 km model resolution), the high-built point has an impervious fraction of 0.65, plan area density of 0.33, area-weighted mean building height of 23.08 m, and building surface to plan area ratio of 0.87. These values are 0.23, 0.11, 6.82 m, and 0.16 for the low-built point, respectively (Table 5). The numbers remain fairly consistent across the datasets, except that the LCZ case has the area-weighted mean building height of 34.17 m for the high-built point, and building surface to plan area ratio of 0.42 for the low-built point.

Table 5. The urban parameters of the selected two points at the modelled 1 km grid resolution. The high-built and low-built points have the elevations of 18.25 m and 54.68 m above sea level and their grids are classified as local climate zone = 3, compact lowrise, and 6, open lowrise, respectively.

	High built (-33.81, 151.01)			Low built (-33.67, 150.93)		
	LCZ	WSF-MB	Geoscape	LCZ	WSF-MB	Geoscape
Impervious fraction	0.68	0.63	0.65	0.37	0.26	0.23
Plan area density	0.37	0.26	0.33	0.21	0.05	0.11
area-weighted mean building height (m)	34.17	21.36	23.08	6.50	5.79	6.82
building surface to plan area ratio	0.88	0.78	0.87	0.42	0.18	0.16

During 17 January, the low-built point showed higher variations at peak through to nighttime across the datasets compared with the high-built one. The temperature time series of the low-built point at 16-17 h showed 6°C variation between the experiments, with 39°C, 37°C, and 33°C values for Geoscape, WSF-MB, and LCZ respectively. This further confirms the observations from Figure 13. The impact on humans at the same time and date would be more tangible looking at the UTCI plots. While the three experiments remained in the strong heat stress zone in their 10^{th} lowest percentile (UTCI cool spots), the 10^{th} highest percentile (UTCI hot spots) showed extreme heat stress (UTCI = 48°C) for Geoscape versus very strong (UTCI = 44°C) and strong (UTCI = 35°C) for WSF-MB and LCZ. Note that increase in UTCI means higher morbidity and mortality (Ghada et al., 2021).

Turning our focus to 13 January, unlike the similar patterns of temperature and UTCI cool spots, the Geoscape and WSF-MB cases reached the extreme heat stress category (UTCI=~48°C) while LCZ stayed in the very strong one (UTCI = 44°C) at the peak of 13 January at the location of the low-built point. The high-built point exhibited a similar pattern except that Geoscape was the case that stayed in the very strong heat stress category. This indicates that certain morphologies can alter their local climate despite strong synoptic forcing.

Average UTCI exceedance can better sum up the differences between the experiments at these two points during 10-20 January 2017. The average exceedance for the high-built point was 9.02°C, 7.86°C, 7.06°C according to LCZ, WSF-MB, and Geoscape, respectively. These numbers were 7.54°C, 9.01°C, 8.93°C for the low built point, respectively. The ~2°C average exceedance difference between the LCZ and Geoscape for the high-built point can be explained by LCZ's higher thermal capacity retaining heat due to its 11m higher area-weighted mean building

height. The LCZ-Geoscape average exceedance difference of ~1.5°C for the low-built point, this time with LCZ having the lower value, can be associated to LCZ's approximately three-fold higher building surface to plan area ratio that creates more shading and lower UTCIs.

Before making any general conclusions about how morphology influences the heat indicators, we emphasise that the longitudinal location (i.e., distance from the coast) led to more drastic changes than the urban characteristics in Sydney as observed in the Figures and analyses since Section 3.2. In other words, the changes due to morphological differences should only be studied within longitudinal locations under the influence of similar weather dynamics, confirming (Potgieter et al., 2021). To conclude this section, we have chosen another point distantly located from the Paramatta area for a similar analysis (Figure S20). Positioned in the cooler eastern suburbs, the peaks dropped by up to 10°C for the three heat indicators (on 13 January) clearly showing the longitudinal effect. The low-built point shows lower valleys (due to lower longwave radiation trapping) and overall, more fluctuations between the datasets compared with the high-built one. This is in line with the fact that lower-built points share more

similar characteristics with a natural land that normally goes through higher temperature peaks and lower nighttime temperatures, aligned with the findings from (Martilli et al., 2024).

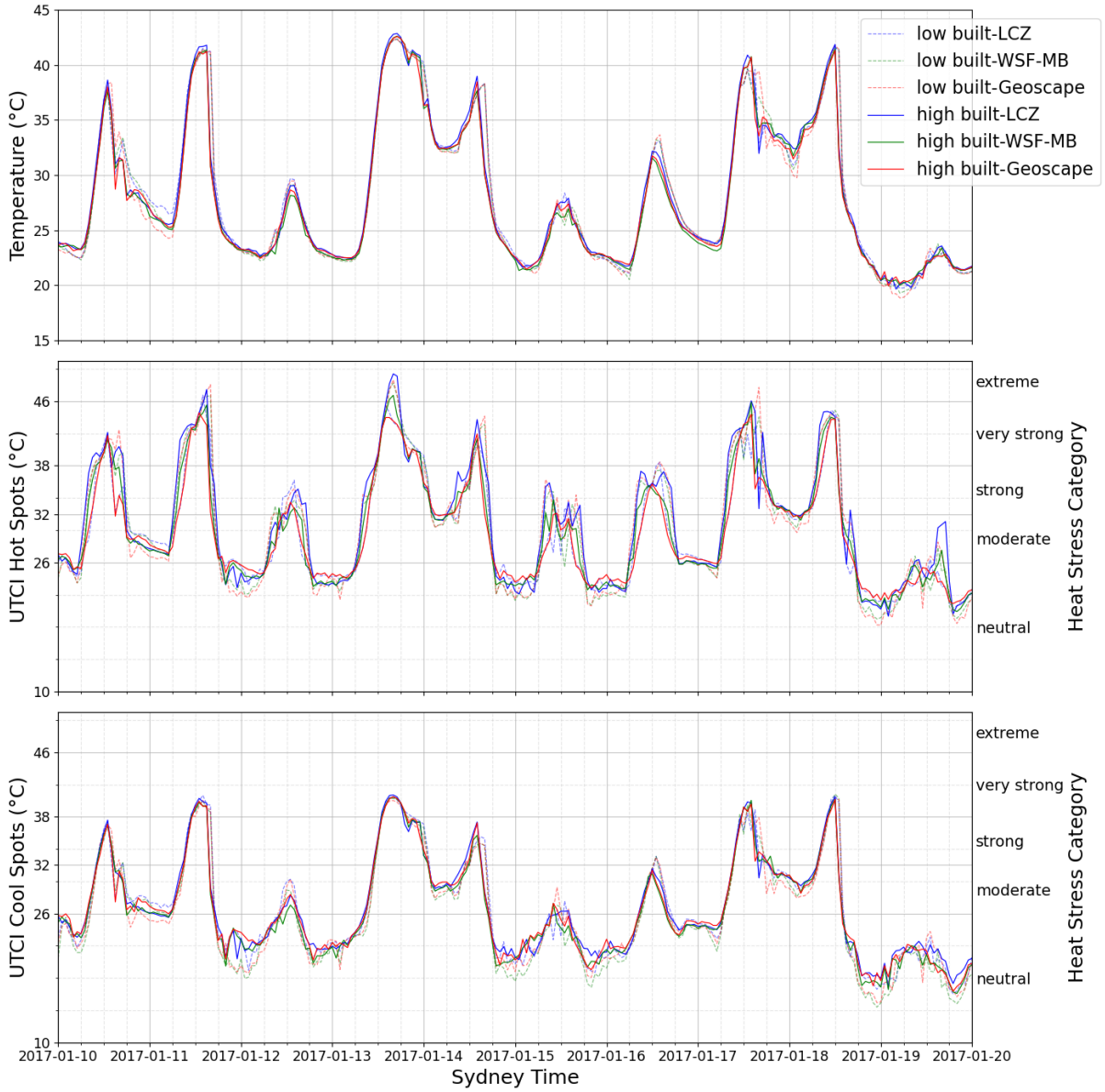

Figure 14. Time series of 2m air temperature (first row), UTCI hot spots (second row), and UTCI cool spots (third row) at the highest-built point in the Paramatta suburb (solid lines, central x mark in Figure 133) and a low-built point (dashed lines, the top x mark in Figure 133) within a similar longitude for the LCZ (blue lines), WSF-MB (green lines), and Geoscape (red lines) cases.

4. Conclusions

This study evaluated four urban morphological datasets for heat modelling in Sydney during 10-20 January 2017 using the Weather Research and Forecasting (WRF) model: the default IGBP-MODIS land use/ land cover data (~927 m resolution), a class-based Local Climate Zones (LCZ) dataset (100 m resolution), gridded satellite-based World Settlement Footprint 3D (WSF-MB, 90m resolution), and a gridded dataset (300 m resolution) derived from Geoscape building-resolving data (at original metre and submetre resolution) based on LiDAR technology in addition to satellite imagery. Although the morphological datasets varied in their spatial

resolution, they were all interpolated and converted to a 1-km resolution to be run with the WRF model. The IGBP-MODIS dataset was used to inform the characteristics of non-urban, natural areas across all experiments. The latter three datasets define the urban morphology with impervious fraction, plan area density, building surface to plan area ratio, area-weighted mean building height, and distribution of building heights. While the IGBP-MODIS dataset was run with the default bulk urban parameterisation of WRF, the latter three experiments used the BEP-BEM-Comfort urban canopy model that provides the subgrid distribution of the universal thermal climate index (UTCI) by calculating 54 values. The LCZ dataset overestimated Sydney's urban morphology parameters compared with the WSF-MB and Geoscape datasets, predicting up to twice the median values of the gridded cases (for building surface to plan area ratio).

Comparing with observations, any spatial dataset improved temperature accuracy by at least 1.29°C mean bias error (MBE) and 1°C mean absolute error (MAE) over WRF defaults, respectively, averaged for peak solar heating hours. The gridded experiments had the most accurate predictions, outperforming the LCZ case by up to 0.48°C (MBE) and 0.37°C (MAE) on average, before sunrise. This suggests urban data holds particular significance at nighttime when longwave radiation highly depends on morphological parameters. The differences became pronounced at inland western stations. More broadly, beyond individual observational sites and averaged metrics, absolute temperature differences between the Default and spatial datasets reached up to 13°C, highlighting the substantial difference urban datasets can make.

Overall, at peak heating times and in heat-vulnerable Western Sydney, any spatial representation would be better for temperature predictions than the default global values. For accurate heat stress estimation during both day and night, gridded urban datasets would provide benefit. While 2m temperature probability density distributions appeared similar across spatial experiments, UTCI probability density distributions revealed substantial differences in heat stress categories during before sunrise, morning, afternoon hours. Gridded datasets predicted up to four times higher probability of the most extreme UTCI heat stress category than the LCZ dataset during the daytime periods, and five times lower probability of strong heat stress before sunrise compared to LCZ. Additionally, LCZ and gridded cases differed by 2-3°C in their estimates of average UTCI exceedance (a cumulative heat exposure index) in Western Sydney, with LCZ producing lower values. Geoscape and WSF-MB (gridded datasets) performed similarly, demonstrating that including a reasonable level of intra-urban variability makes accurate modelling achievable without access to advanced technologies such as LiDAR. This level is not met in the LCZ case for heat exposure studies due to its toned-down morphological variability.

Urban dataset choice would influence temperature and UTCI spatial patterns most strongly during weak synoptic conditions. However, even under strong synoptic forcing, relying on more simplified urban datasets such as LCZ might lead to substantial discrepancies in estimating heat stress during critical hours. For instance, the 10th highest percentile of UTCI dropped from 48°C (extreme heat stress) as predicted by the gridded to 44°C in LCZ (very strong heat stress) at a central northern area in Sydney in the afternoon of 13 January 2017– a day with strong synoptic forcing. These numbers could require different levels of emergency preparation, knowing the direct correlation between an increase in UTCI and increased rate of morbidity and mortality (Ghada et al., 2021).

Although the findings showed urban morphology considerably reduced temperature errors, residual model biases remain due to larger-scale forcing and physics. Future studies can explore these model-related biases through running with different physics schemes, higher

spatial resolution, and employing ensemble members. Although our case study was Sydney, the conceptual findings regarding the WRF default versus class-based versus gridded urban representations are expected to be relevant for other cities. Nonetheless, to consolidate the findings, we suggest choosing cities with different geographical and meteorological conditions, such as non-coastal, mountainous, arid, polar or tropical cities, and during weak and strong synoptic forcing periods. Finally, we recommend exploring more human heat-health indicators in order to quantify and better describe the implications that using each urban dataset might have on human health.

Data and code availability

The Automated Weather Station data used in this study was purchased from the Bureau of Meteorology (https://reg.bom.gov.au/climate/data/stations/). The observational data from Department of Climate Change, Energy, the Environment and Water is publicly available (https://www.airquality.nsw.gov.au/air-quality-data-services/data-download-facility). The WRF model is open access and publicly available (https://github.com/wrf-model/WRF). The analysis codes and associated WRF files of this study are publicly available (https://github.com/maryam-fazeli/Analysis-Fazeli_et_al_2026 and https://zenodo.org/records/18960698).

Declaration of generative AI use

During the preparation of this work the author(s) used Claude, Anthropic and ChatGPT, OpenAI in order to help with analysis, coding, and revising the manuscript for sentence structures and proofreading. After using this tool/service, the author(s) reviewed and edited the content as needed and take(s) full responsibility for the content of the published article.

Financial support

This research was supported by the Australian Research Council Centre of Excellence for the Weather of the 21st Century (grant no. CE230100012) and the Australian Research Council Centre of Excellence for Climate Extremes (CE170100023).

Acknowledgement

This research was undertaken with the assistance of resources from the National Computational Infrastructure (NCI Australia), an NCRIS enabled capability supported by the Australian Government.

References

Abunyewah, M., Gajendran, T., Erdiaw-Kwasie, M.O., Baah, C., Okyere, S.A., Kankanamge, A.K.S.U., 2025. The multidimensional impacts of heatwaves on human ecosystems: A systematic literature review and future research direction. Environ. Sci. Policy 165, 104024. https://doi.org/10.1016/j.envsci.2025.104024

Argüeso, D., Evans, J.P., Fita, L., Bormann, K.J., 2014. Temperature response to future urbanization and climate change. Clim. Dyn. 42, 2183–2199. https://doi.org/10.1007/s00382-013-1789-6

Arsad, F.S., Hod, R., Ahmad, N., Ismail, R., Mohamed, N., Baharom, M., Osman, Y., Radi, M.F.M., Tangang, F., 2022. The impact of heatwaves on mortality and morbidity and the associated vulnerability factors: A systematic review. Int. J. Environ. Res. Public Health 19, 16356. https://doi.org/10.3390/ijerph192316356

Australian Bureau of Statistics, 2021. Historical population [WWW Document]. ABS. URL https://www.abs.gov.au/statistics/people/population/historical-population/2021 (accessed 11.19.24).

Bechtold, P., Bazile, E., Guichard, F., Mascart, P., Richard, E., 2001. A mass-flux convection scheme for regional and global models. Q. J. R. Meteorol. Soc. 127, 869–886. https://doi.org/10.1002/qj.49712757309

Bhattarai, S., Bokati, L., Sharma, S., Talchabhadel, R., 2025. Understanding spatiotemporal variation of heatwave projections across US cities. Sci. Rep. 15, 10643. https://doi.org/10.1038/s41598-025-95097-5

Biljecki, F., Chew, L.Z.X., Milojevic-Dupont, N., Creutzig, F., 2021. Open government geospatial data on buildings for planning sustainable and resilient cities. arXiv [cs.CY].

Błażejczyk, K., Jendritzky, B.G., Bröde, B.P., Kampmann, B.B., 2013. An introduction to the Universal Thermal Climate Index (UTCI). Geographia Polonica 86, 5–10. https://doi.org/10.7163/GPol.2013.1

Bougeault, P., Lacarrere, P., 1989. Parameterization of orography-induced turbulence in a mesobeta--scale model. Mon. Weather Rev. 117, 1872–1890. https://doi.org/10.1175/1520-0493(1989)117<1872:pooiti>2.0.co;2

Brimicombe, C., Di Napoli, C., Quintino, T., Pappenberger, F., Cornforth, R., Cloke, H.L., 2022. Thermofeel: A python thermal comfort indices library. SoftwareX 18, 101005. https://doi.org/10.1016/j.softx.2022.101005

Cedeño Laurent, J.G., Williams, A., Oulhote, Y., Zanobetti, A., Allen, J.G., Spengler, J.D., 2018. Reduced cognitive function during a heat wave among residents of non-air-conditioned buildings: An observational study of young adults in the summer of 2016. PLoS Med. 15, e1002605. https://doi.org/10.1371/journal.pmed.1002605

Cheng, Y., Zhao, L., Chakraborty, T.C., Oleson, K., Demuzere, M., Liu, X., Che, Y., Liao, W., Zhou, Y., Li, X. “cathy,” 2025. U-Surf: a global 1 km spatially continuous urban surface property dataset for kilometer-scale urban-resolving Earth system modeling. Earth Syst. Sci. Data 17, 2147–2174. https://doi.org/10.5194/essd-17-2147-2025

Ching, J., Mills, G., Bechtel, B., See, L., Feddema, J., Wang, X., Ren, C., Brousse, O., Martilli, A., Neophytou, M., Mouzourides, P., Stewart, I., Hanna, A., Ng, E., Foley, M., Alexander, P., Aliaga, D., Niyogi, D., Shreevastava, A., Bhalachandran, P., Masson, V., Hidalgo, J., Fung, J., Andrade, M., Baklanov, A., Dai, W., Milcinski, G., Demuzere, M., Brunsell, N., Pesaresi, M., Miao, S., Mu, Q., Chen, F., Theeuwes, N., 2018. WUDAPT: An Urban Weather, Climate, and Environmental Modeling Infrastructure for the Anthropocene. Bulletin of the American Meteorological Society 99, 1907–1924. https://doi.org/10.1175/BAMS-D-16-0236.1

Coates, L., van Leeuwen, J., Browning, S., Gissing, A., Bratchell, J., Avci, A., 2022. Heatwave fatalities in Australia, 2001–2018: An analysis of coronial records. Int. J. Disaster Risk Reduct. 67, 102671. https://doi.org/10.1016/j.ijdrr.2021.102671

Copernicus Climate Change Service, 2019. ERA5-Land hourly data from 1950 to present. https://doi.org/10.24381/CDS.E2161BAC

Copernicus Climate Change Service, 2018. ERA5 hourly data on single levels from 1940 to present. https://doi.org/10.24381/CDS.ADBB2D47

DCCEEW, 2023. Data download facility [WWW Document]. Air Quality NSW. URL https://www.airquality.nsw.gov.au/air-quality-data-services/data-download-facility (accessed 1.28.26).

de Dear, R., Brager, G., 1998. Developing an adaptive model of thermal comfort and preference. UC Berkeley: Center for the Built Environment.

Demuzere, M., Argüeso, D., Zonato, A., Kittner, J., 2022. W2W: A Python package that injects WUDAPT's Local Climate Zone information in WRF. J. Open Source Softw. 7, 4432. https://doi.org/10.21105/joss.04432

Demuzere, M., Hankey, S., Mills, G., Zhang, W., Lu, T., Bechtel, B., 2020. Combining expert and crowd-sourced training data to map urban form and functions for the continental US. Sci. Data 7, 264. https://doi.org/10.1038/s41597-020-00605-z

Di Napoli, C., Pappenberger, F., Cloke, H.L., 2018. Assessing heat-related health risk in Europe via the Universal Thermal Climate Index (UTCI). Int. J. Biometeorol. 62, 1155–1165. https://doi.org/10.1007/s00484-018-1518-2

Esch, T., Brzoska, E., Dech, S., Leutner, B., Palacios-Lopez, D., Metz-Marconcini, A., Marconcini, M., Roth, A., Zeidler, J., 2022. World Settlement Footprint 3D - A first three-dimensional survey of the global building stock. Remote Sens. Environ. 270, 112877. https://doi.org/10.1016/j.rse.2021.112877

Faurie, C., Varghese, B.M., Liu, J., Bi, P., 2022. Association between high temperature and heatwaves with heat-related illnesses: A systematic review and meta-analysis. Sci. Total Environ. 852, 158332. https://doi.org/10.1016/j.scitotenv.2022.158332

Fuhrmann, C., Robinson, A., Konrad, C., Bhatia, A., 2024. From data to action: How urban heat mapping campaigns can expose vulnerabilities and inform local heat policy. Bull. Am. Meteorol. Soc. 105, E2078–E2084. https://doi.org/10.1175/bams-d-24-0230.1

Gabeiras, J., 2025. wrfup. Github. https://github.com/jacobogabeiraspenas/wrfup.

Geoscape Australia [WWW Document], 2022. . PSMA. URL https://geoscape.com.au/ (accessed 8.1.24).

Geoscape Buildings v2.0, 2020. . Geoscape Buildings v2.0.

Geoscape Surface Cover v1.6, 2020. . Geoscape Surface Cover v1.6.

Ghada, W., Estrella, N., Ankerst, D.P., Menzel, A., 2021. Universal thermal climate index associations with mortality, hospital admissions, and road accidents in Bavaria. PLoS One 16, e0259086. https://doi.org/10.1371/journal.pone.0259086

Ghanbari, M., Arabi, M., Georgescu, M., Broadbent, A.M., 2023. The role of climate change and urban development on compound dry-hot extremes across US cities. Nat. Commun. 14, 3509. https://doi.org/10.1038/s41467-023-39205-x

GlobalMLBuildingFootprints, 2024. . Github.

Glotfelty, T., Alapaty, K., He, J., Hawbecker, P., Song, X., Zhang, G., 2019. The Weather Research and Forecasting Model with aerosol-Cloud Interactions (WRF-ACI): Development, evaluation, and initial application. Mon. Weather Rev. 147, 1491–1511. https://doi.org/10.1175/MWR-D-18-0267.1

Google Earth [WWW Document], 2025. URL https://earth.google.com/web/search/Sydney+NSW/@-33.74040628,150.79740034,97.65028137a,165710.99752558d,35y,0h,0t,0r/data=CiwiJgokCTi1WTKZ7D7AEdiSK2XmXUPAGXRbz2A6SGRAIYXxN5uxhGFAQgIIATIpCicKJQohM

WgxNXRCOWpxYnpEZEF1VFVoYVByOWY2QjRRUFBLb1lfIAE6AwoBMEICCABKCAiNzMbkAxAB (accessed 25).
Guo, Y., Gasparrini, A., Armstrong, B.G., Tawatsupa, B., Tobias, A., Lavigne, E., Coelho, M. de S.Z.S., Pan, X., Kim, H., Hashizume, M., Honda, Y., Guo, Y.-L.L., Wu, C.-F., Zanobetti, A., Schwartz, J.D., Bell, M.L., Scortichini, M., Michelozzi, P., Punnasiri, K., Li, S., Tian, L., Garcia, S.D.O., Seposo, X., Overcenco, A., Zeka, A., Goodman, P., Dang, T.N., Van Dung, D., Mayvaneh, F., Saldiva, P.H.N., Williams, G., Tong, S., 2017. Heat wave and mortality: A multicountry, multicommunity study. Environ. Health Perspect. 125, 087006. https://doi.org/10.1289/EHP1026
Gutiérrez, E., Martilli, A., Santiago, J.L., González, J.E., 2015. A mechanical drag coefficient formulation and urban canopy parameter assimilation technique for complex urban environments. Boundary Layer Meteorol. 157, 333–341. https://doi.org/10.1007/s10546-015-0051-7
He, C., Valayamkunna, P., Barlage, M., Chen, F., Gochis, D., Cabell, R., Schneider, T., Rasmussen, R., Niu, G.-Y., Yang, Z.-L., Niyogi, D., Ek, M., 2023. The Community Noah-MP Land Surface Modeling System Technical Description Version 5.0.
He, C., Zhang, Yuqiang, Schneider, A., Chen, R., Zhang, Yan, Ma, W., Kinney, P.L., Kan, H., 2022. The inequality labor loss risk from future urban warming and adaptation strategies. Nat. Commun. 13, 3847. https://doi.org/10.1038/s41467-022-31145-2
Hersbach, H., Bell, B., Berrisford, P., Hirahara, S., Horányi, A., Muñoz-Sabater, J., Nicolas, J., Peubey, C., Radu, R., Schepers, D., Simmons, A., Soci, C., Abdalla, S., Abellan, X., Balsamo, G., Bechtold, P., Biavati, G., Bidlot, J., Bonavita, M., De Chiara, G., Dahlgren, P., Dee, D., Diamantakis, M., Dragani, R., Flemming, J., Forbes, R., Fuentes, M., Geer, A., Haimberger, L., Healy, S., Hogan, R.J., Hólm, E., Janisková, M., Keeley, S., Laloyaux, P., Lopez, P., Lupu, C., Radnoti, G., de Rosnay, P., Rozum, I., Vamborg, F., Villaume, S., Jean-Noël Thépaut, 2020. The ERA5 global reanalysis. Q. J. R. Meteorol. Soc. 146, 1999–2049. https://doi.org/10.1002/qj.3803
Hirsch, A.L., Evans, J.P., Thomas, C., Conroy, B., Hart, M.A., Lipson, M., Ertler, W., 2021. Resolving the influence of local flows on urban heat amplification during heatwaves. Environ. Res. Lett. 16, 064066. https://doi.org/10.1088/1748-9326/ac0377
Hong, S., Lim, J., 2006. The WRF Single-Moment 6-Class Microphysics Scheme (WSM6). Asia-pacific Journal of Atmospheric Sciences 42, 129–151.
Iacono, M.J., Delamere, J.S., Mlawer, E.J., Shephard, M.W., Clough, S.A., Collins, W.D., 2008. Radiative forcing by long-lived greenhouse gases: Calculations with the AER radiative transfer models. J. Geophys. Res. 113. https://doi.org/10.1029/2008jd009944
Janjić, Z.I., 2001. Nonsingular implementation of the Mellor-Yamada level 2.5 scheme in the NCEP Meso model [WWW Document]. URL https://repository.library.noaa.gov/view/noaa/11409 (accessed 7.22.25).
Janjić, Z.I., 1996. THE SURFACE LAYER IN THE NCEP ETA MODEL. Presented at the 11th Numerical Weather Prediction, American Meteorological Society, Boston, MA.
Janjić, Z.I., 1994. The step-mountain eta coordinate model: Further developments of the convection, viscous sublayer, and turbulence closure schemes. Mon. Weather Rev. 122, 927–945. https://doi.org/10.1175/1520-0493(1994)122<0927:tsmecm>2.0.co;2
Jendritzky, G., de Dear, R., Havenith, G., 2012. UTCI--why another thermal index? Int. J. Biometeorol. 56, 421–428. https://doi.org/10.1007/s00484-011-0513-7
Jendritzky, G., Tinz, B., 2009. The thermal environment of the human being on the global scale. Glob. Health Action 2. https://doi.org/10.3402/gha.v2i0.2005
Katzfey, J., Schlünzen, H., Hoffmann, P., Thatcher, M., 2020. How an urban parameterization affects a high-resolution global climate simulation. Quart. J. Roy. Meteor. Soc. 146, 3808–3829. https://doi.org/10.1002/qj.3874

Li, D., Malyshev, S., Shevliakova, E., 2016. Exploring historical and future urban climate in the Earth System Modeling framework: 1. Model development and evaluation. J. Adv. Model. Earth Syst. 8, 917–935. https://doi.org/10.1002/2015ms000578
Liao, W., Li, Y., Liu, X., Wang, Y., Che, Y., Shao, L., Chen, G., Yuan, H., Zhang, N., Chen, F., 2025. GloUCP: a global 1 km spatially continuous urban canopy parameters for the WRF model. Earth Syst. Sci. Data 17, 2535–2551. https://doi.org/10.5194/essd-17-2535-2025
Lipson, M.J., Nazarian, N., Hart, M.A., Nice, K.A., Conroy, B., 2022. A Transformation in City-Descriptive Input Data for Urban Climate Models. Front. Environ. Sci. Eng. China 10. https://doi.org/10.3389/fenvs.2022.866398
Lipson, M.J., Thatcher, M., Hart, M.A., Pitman, A., 2019. Climate change impact on energy demand in building-urban-atmosphere simulations through the 21st century. Environ. Res. Lett. 14, 125014. https://doi.org/10.1088/1748-9326/ab5aa5
Lu, J., Nazarian, N., Hart, M.A., 2024. A one-dimensional urban flow model with an eddy-diffusivity mass-flux (EDMF) scheme and refined turbulent transport (MLUCM v3. 0). Geoscientific Model.
Marcotullio, P.J., Keßler, C., Fekete, B.M., 2022. Global urban exposure projections to extreme heatwaves. Front. Built Environ. 8, 947496. https://doi.org/10.3389/fbuil.2022.947496
Martilli, A., Clappier, A., Rotach, M.W., 2002. An Urban Surface Exchange Parameterisation for Mesoscale Models. Bound.-Layer Meteorol. 104, 261–304. https://doi.org/10.1023/A:1016099921195
Martilli, A., Krayenhoff, E.S., Nazarian, N., 2020. Is the Urban Heat Island intensity relevant for heat mitigation studies? Urban Climate 31, 100541. https://doi.org/10.1016/j.uclim.2019.100541
Martilli, A., Nazarian, N., Krayenhoff, E.S., Lachapelle, J., Lu, J., Rivas, E., Rodriguez-Sanchez, A., Sanchez, B., Santiago, J.L., 2024. WRF-Comfort: simulating microscale variability in outdoor heat stress at the city scale with a mesoscale model. Geosci. Model Dev. 17, 5023–5039. https://doi.org/10.5194/gmd-17-5023-2024
Mazloumi, A., Golbabaei, F., Mahmood Khani, S., Kazemi, Z., Hosseini, M., Abbasinia, M., Farhang Dehghan, S., 2014. Evaluating effects of heat stress on cognitive function among workers in a hot industry. Health Promot. Perspect. 4, 240–246. https://doi.org/10.5681/hpp.2014.031
Meehl, G.A., Tebaldi, C., 2004. More intense, more frequent, and longer lasting heat waves in the 21st century. Science 305, 994–997. https://doi.org/10.1126/science.1098704
Miner, M.J., Taylor, R.A., Jones, C., Phelan, P.E., 2017. Efficiency, economics, and the urban heat island. Environ. Urban. 29, 183–194. https://doi.org/10.1177/0956247816655676
Monin, A.S., Obukhov, A.M., 2009. Basic laws of turbulent mixing in the surface layer of the atmosphere. Inst 24, 163–187.
Muñoz-Sabater, J., Dutra, E., Agustí-Panareda, A., Albergel, C., Arduini, G., Balsamo, G., Boussetta, S., Choulga, M., Harrigan, S., Hersbach, H., Martens, B., Miralles, D.G., Piles, M., Rodríguez-Fernández, N.J., Zsoter, E., Buontempo, C., Jean-Noël Thépaut, 2021. ERA5-Land: a state-of-the-art global reanalysis dataset for land applications. Earth Syst. Sci. Data 13, 4349–4383. https://doi.org/10.5194/essd-13-4349-2021
Nazarian, N., Krayenhoff, E.S., Bechtel, B., Hondula, D.M., Paolini, R., Vanos, J., Cheung, T., Chow, W.T.L., de Dear, R., Jay, O., Lee, J.K.W., Martilli, A., Middel, A., Norford, L.K., Sadeghi, M., Schiavon, S., Santamouris, M., 2022. Integrated assessment of urban overheating impacts on human life. Earths Future 10. https://doi.org/10.1029/2022ef002682
Nazarian, N., Krayenhoff, E.S., Martilli, A., 2020. A one-dimensional model of turbulent flow through “urban” canopies (MLUCM v2.0): updates based on large-eddy simulation. Geosci. Model Dev. 13, 937–953. https://doi.org/10.5194/gmd-13-937-2020

Nazarian, N., Lee, J.K.W., 2021. Personal assessment of urban heat exposure: a systematic review. Environ. Res. Lett. 16, 033005. https://doi.org/10.1088/1748-9326/abd350
Niu, G.-Y., Yang, Z.-L., Mitchell, K.E., Chen, F., Ek, M.B., Barlage, M., Kumar, A., Manning, K., Niyogi, D., Rosero, E., Tewari, M., Xia, Y., 2011. The community Noah land surface model with multiparameterization options (Noah-MP): 1. Model description and evaluation with local-scale measurements. J. Geophys. Res. 116. https://doi.org/10.1029/2010jd015139
Obringer, R., Nateghi, R., Maia-Silva, D., Mukherjee, S., Cr, V., McRoberts, D.B., Kumar, R., 2022. Implications of increasing household air conditioning use across the United States under a warming climate. Earths Future 10, e2021EF002434. https://doi.org/10.1029/2021ef002434
Oke, T.R., 1982. The energetic basis of the urban heat island. Q. J. R. Meteorol. Soc. 108, 1–24. https://doi.org/10.1002/qj.49710845502
Potgieter, J., Nazarian, N., Lipson, M.J., Hart, M.A., Ulpiani, G., Morrison, W., Benjamin, K., 2021. Combining high-resolution land use data with crowdsourced air temperature to investigate intra-urban microclimate. Front. Environ. Sci. 9, 720323. https://doi.org/10.3389/fenvs.2021.720323
Prein, A.F., Langhans, W., Fosser, G., Ferrone, A., Ban, N., Goergen, K., Keller, M., Tölle, M., Gutjahr, O., Feser, F., Brisson, E., Kollet, S., Schmidli, J., van Lipzig, N.P.M., Leung, R., 2015. A review on regional convection-permitting climate modeling: Demonstrations, prospects, and challenges: CONVECTION-PERMITTING CLIMATE MODELING. Rev. Geophys. 53, 323–361. https://doi.org/10.1002/2014RG000475
Ren, Z., Fu, Y., Dong, Y., Zhang, P., He, X., 2022. Rapid urbanization and climate change significantly contribute to worsening urban human thermal comfort: A national 183-city, 26-year study in China. Urban Clim. 43, 101154. https://doi.org/10.1016/j.uclim.2022.101154
Sadeghi, M., de Dear, R., Morgan, G., Santamouris, M., Jalaludin, B., 2021. Development of a heat stress exposure metric – Impact of intensity and duration of exposure to heat on physiological thermal regulation. Build. Environ. 200, 107947. https://doi.org/10.1016/j.buildenv.2021.107947
Salamanca, F., Georgescu, M., Mahalov, A., Moustaoui, M., Wang, M., 2014. Anthropogenic heating of the urban environment due to air conditioning: Anthropogenic Heating due to AC. J. Geophys. Res. 119, 5949–5965. https://doi.org/10.1002/2013jd021225
Salamanca, F., Krpo, A., Martilli, A., Clappier, A., 2010. A new building energy model coupled with an urban canopy parameterization for urban climate simulations—part I. formulation, verification, and sensitivity analysis of the model. Theor. Appl. Climatol. 99, 331–344. https://doi.org/10.1007/s00704-009-0142-9
Salamanca, F., Martilli, A., 2010. A new Building Energy Model coupled with an Urban Canopy Parameterization for urban climate simulations—part II. Validation with one dimension off-line simulations. Theor. Appl. Climatol. 99, 345–356. https://doi.org/10.1007/s00704-009-0143-8
Salamanca, F., Zhang, Y., Barlage, M., Chen, F., Mahalov, A., Miao, S., 2018. Evaluation of the WRF-urban modeling system coupled to Noah and Noah-MP land surface models over a semiarid urban environment. J. Geophys. Res. 123, 2387–2408. https://doi.org/10.1002/2018jd028377
Santamouris, M., Paolini, R., Haddad, S., Synnefa, A., Garshasbi, S., Hatvani-Kovacs, G., Gobakis, K., Yenneti, K., Vasilakopoulou, K., Feng, J., Gao, K., Papangelis, G., Dandou, A., Methymaki, G., Portalakis, P., Tombrou, M., 2020. Heat mitigation technologies can improve sustainability in cities. An holistic experimental and numerical impact assessment of urban overheating and related heat mitigation strategies on energy

consumption, indoor comfort, vulnerability and heat-related mortality and morbidity in cities. Energy Build. 217, 110002. https://doi.org/10.1016/j.enbuild.2020.110002
Santiago, J.L., Martilli, A., 2010. A dynamic urban canopy parameterization for mesoscale models based on computational fluid dynamics Reynolds-averaged Navier–stokes microscale simulations. Boundary Layer Meteorol. 137, 417–439. https://doi.org/10.1007/s10546-010-9538-4
Sharma, S., Evans, J.P., Pitman, A., Nazarian, N., Lipson, M.J., Lopez-Bravo, C., 2025. Mapping urban dynamics in Greater Sydney – A scalable multi-decadal local climate zone classification approach. PLOS Clim. 4, e0000677. https://doi.org/10.1371/journal.pclm.0000677
Shen, P., Ji, Y., Li, Y., Wang, M., Cui, X., Tong, H., 2025. Combined impact of climate change and urban heat island on building energy use in three megacities in China. Energy Build. 331, 115386. https://doi.org/10.1016/j.enbuild.2025.115386
Sirko, W., Kashubin, S., Ritter, M., Annkah, A., Bouchareb, Y.S.E., Dauphin, Y., Keysers, D., Neumann, M., Cisse, M., Quinn, J., 2021. Continental-Scale Building Detection from High Resolution Satellite Imagery. arXiv [cs.CV].
Skamarock, W.C., Klemp, J.B., Dudhia, J., Gill, D.O., Liu, Z., Berner, J., Wang, W., Powers, J.G., Duda, M.G., Barker, D.M., Huang, X.Y., 2019. A Description of the Advanced Research WRF Model Version 4.
Stewart, I.D., Oke, T.R., 2012. Local Climate Zones for Urban Temperature Studies. Bull. Am. Meteorol. Soc. 93, 1879–1900. https://doi.org/10.1175/BAMS-D-11-00019.1
Stewart, I.D., Oke, T.R., Krayenhoff, E.S., 2014. Evaluation of the 'local climate zone' scheme using temperature observations and model simulations: EVALUATION OF THE 'LOCAL CLIMATE ZONE' SCHEME. Int. J. Climatol. 34, 1062–1080. https://doi.org/10.1002/joc.3746
The Bureau of Meteorology, 2025. Climate classification maps [WWW Document]. URL https://www.bom.gov.au/climate/maps/averages/climate-classification/?maptype=koppen_major_AGCDv2_&period=1991-2020 (accessed 11.4.25).
The Bureau of Meteorology, 2017. Special Climate Statement 61-exceptional heat in southeast Australia in early 2017. The Bureau of Meteorology.
Thisara Sathsara, K.L., Kusaka, H., 2025. Impact of high-resolution land use data on numerical simulations of Colombo's thermal environment during heatwaves. Theor. Appl. Climatol. 156, 106. https://doi.org/10.1007/s00704-024-05242-9
Tong, S., Prior, J., McGregor, G., Shi, X., Kinney, P., 2021. Urban heat: an increasing threat to global health. BMJ 375, n2467. https://doi.org/10.1136/bmj.n2467
World Meteorological Organization (WMO), 2008. Guide to Meteorological Instruments and Methods of Observation, Seventh Edition. WMO.
Wu, S., Wang, P., Tong, X., Tian, H., Zhao, Y., Luo, M., 2021. Urbanization-driven increases in summertime compound heat extremes across China. Sci. Total Environ. 799, 149166. https://doi.org/10.1016/j.scitotenv.2021.149166
Xue, L., Doan, Q., Kusaka, H., He, C., Chen, F., 2024. Insights into urban heat island and heat waves synergies revealed by a land-surface-physics-Based Downscaling method. J. Geophys. Res. 129, e2023JD040531. https://doi.org/10.1029/2023jd040531
Yang, X., Xu, X., Wang, Y., Yang, J., Wu, X., 2024. Heat exposure impacts on urban health: A meta-analysis. Sci. Total Environ. 947, 174650. https://doi.org/10.1016/j.scitotenv.2024.174650
Yang, Z.-L., Niu, G.-Y., Mitchell, K.E., Chen, F., Ek, M.B., Barlage, M., Longuevergne, L., Manning, K., Niyogi, D., Tewari, M., Xia, Y., 2011. The community Noah land surface model with multiparameterization options (Noah-MP): 2. Evaluation over global river basins. J. Geophys. Res. 116. https://doi.org/10.1029/2010jd015140

Zheng, Y., Alapaty, K., Herwehe, J.A., Del Genio, A.D., Niyogi, D., 2016. Improving high-resolution weather forecasts using the weather research and forecasting (WRF) model with an updated Kain–Fritsch scheme. Mon. Weather Rev. 144, 833–860. https://doi.org/10.1175/mwr-d-15-0005.1

Are high-resolution urban datasets necessary for accurate heat exposure modelling in cities? – Supplementary material

Maryam Fazeli[1,2,3,4], Negin Nazarian[1,2,3,4], Jason P. Evans[2,3,4], Mathew J. Lipson[2,3,4], Jacobo Gabeiras Penas[5], Shankar Sharma [2,3,4], Alberto Martilli[6]

[1]School of Built Environment, UNSW, Australia
[2]Climate Change Research Centre, UNSW, Australia
[3]ARC Centre of Excellence for Weather of the 21st Century, Australia
[4]ARC Centre of Excellence for Climate Extremes, Australia
[5]Université Grenoble Alpes, France
[6]Environmental Department, CIEMAT, Spain

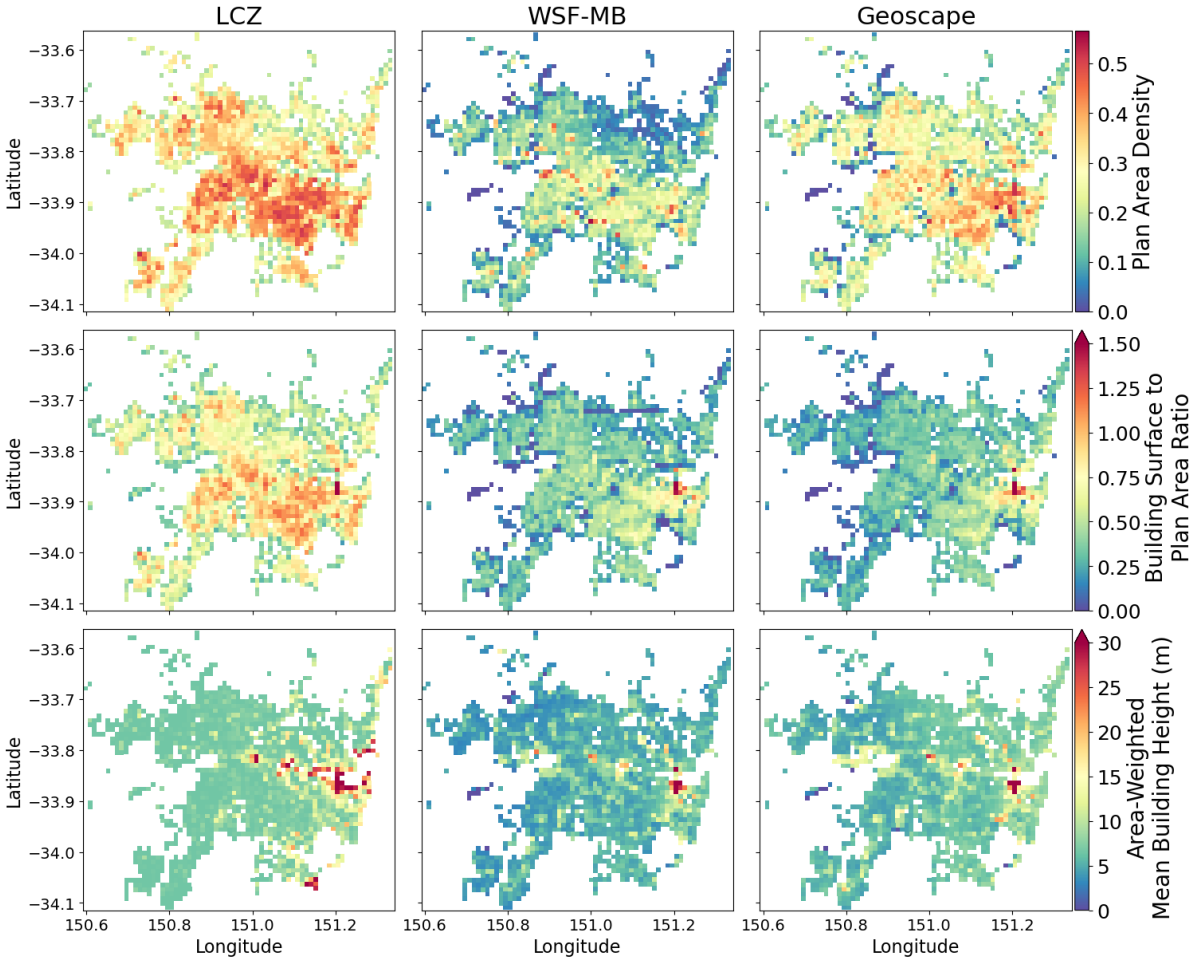

Figure S1. Spatial distribution of plan area density (first row), building surface to plan area ratio (second row), and area-weighted mean building height (third row) for the LCZ, WSF-MB, and Geoscape experiments.

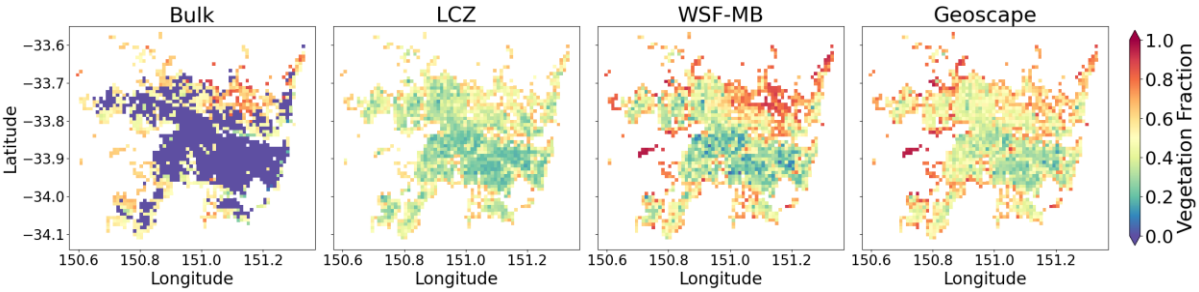

Figure S2. Spatial distribution of vegetation fraction for the four experiments.

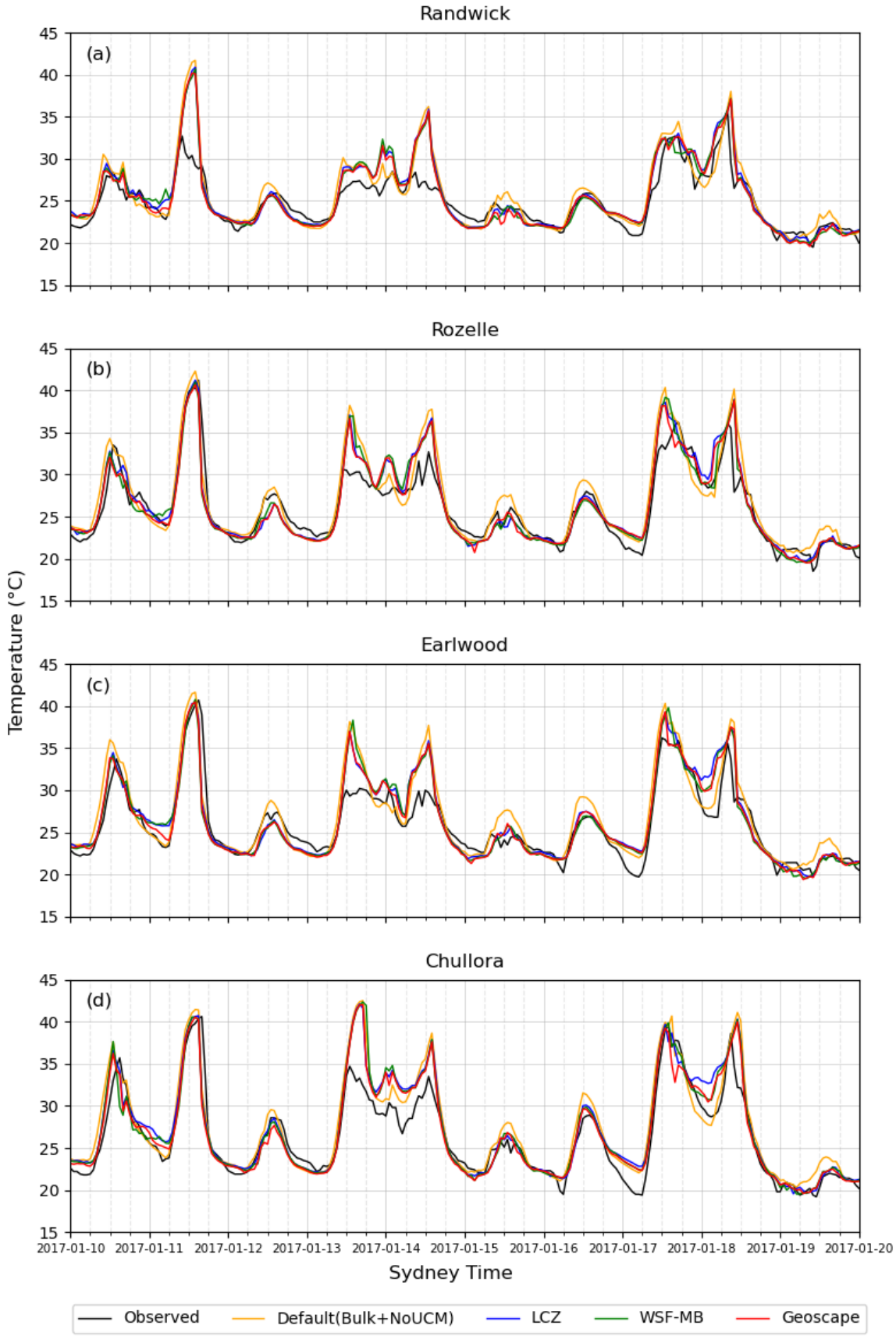

Figure S3. Hourly mean temperature time series – observed vs. modelled (Default, LCZ, WSF-MB, and Geoscape experiments) – at DCCEEW stations at Randwick (a), Rozelle (b), Earlwood (c), and Chullora (d).

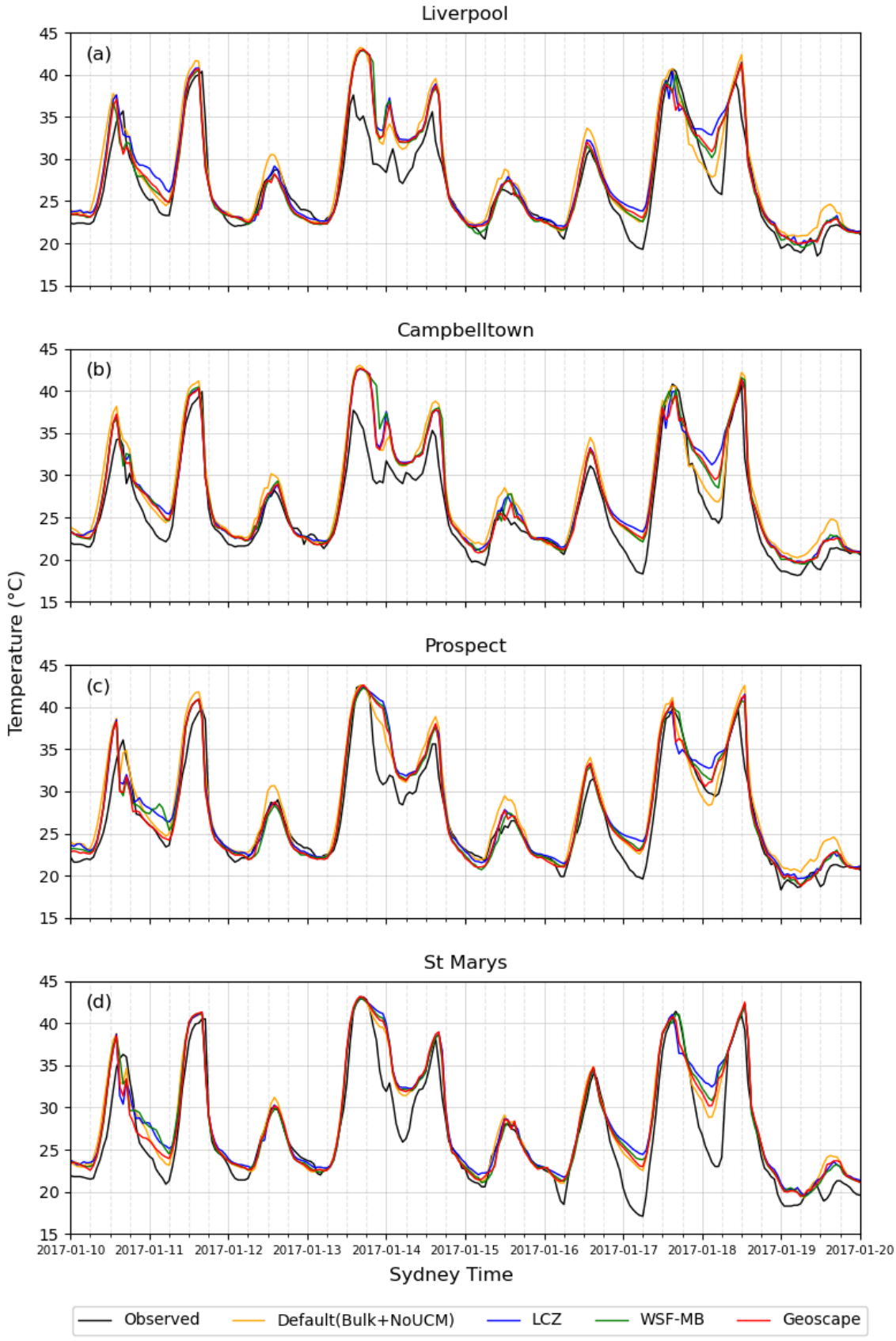

Figure S4. Hourly mean temperature time series – observed vs. modelled (Default, LCZ, WSF-MB, and Geoscape experiments) – at DCCEEW stations at Liverpool (a), Campbelltown (b), Prospect (c), and St Marys (d).

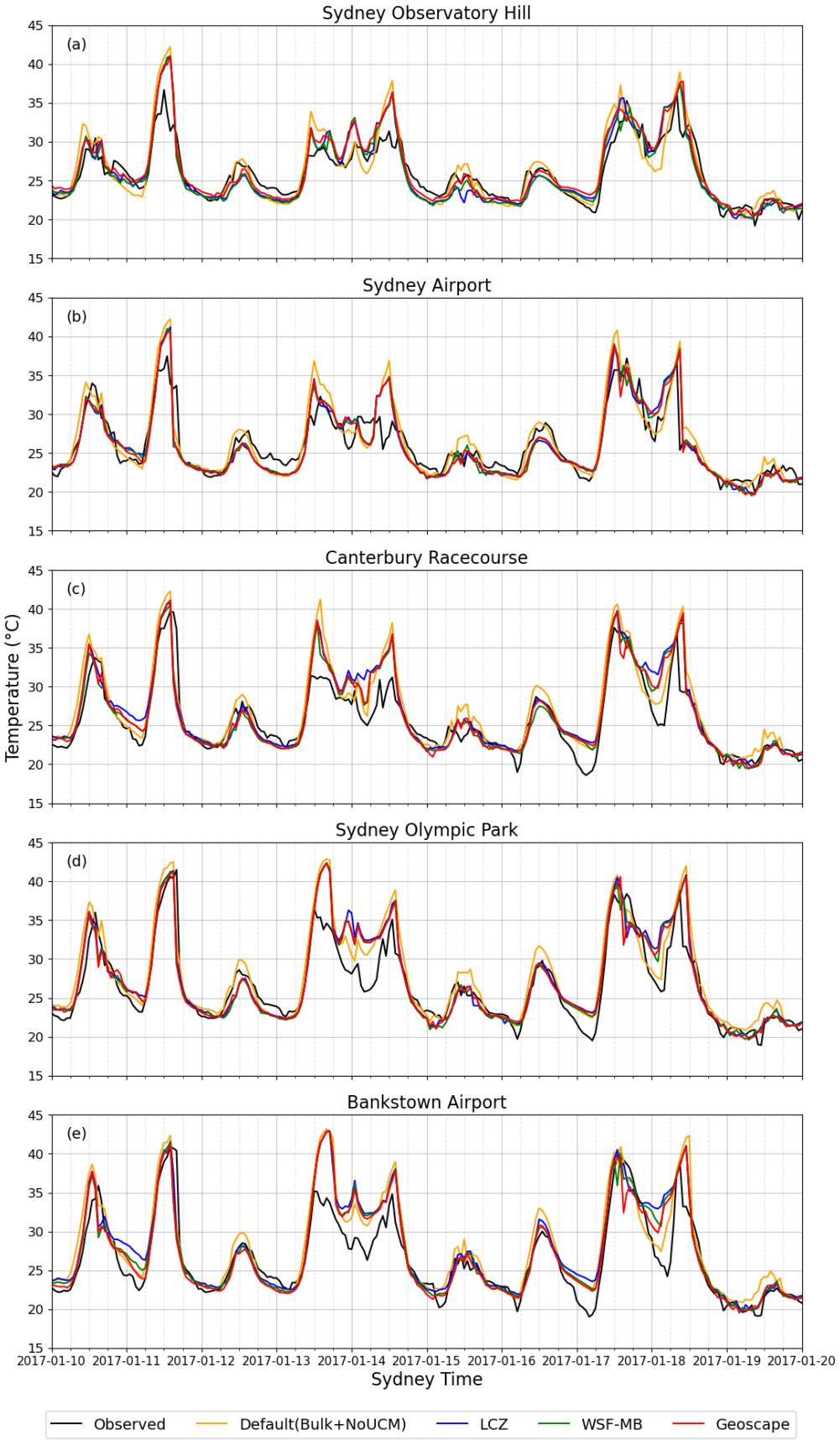

Figure S5. Instantaneous temperature time series – observed vs. modelled (Default, LCZ, WSF-MB, and Geoscape experiments) – at BoM stations at Sydney Observatory Hill (a), Sydney Airport (b), Canterbury Racecourse (c), Sydney Olympic Park (d), Bankstown Airport (e).

Table S1. Mean bias error (MBE), mean absolute error (MAE), and Pearson correlation of modelled data with observations (DCCEEW hourly mean temperature, BoM instantaneous temperature, and DCCEEW hourly mean relative humidity) – temporally averaged over the 10-day period at all times as well as averaged over the diurnal periods of before sunrise (2-5 h), morning (7-10 h), peak solar heating (11-14 h), afternoon (15-18 h), evening (19-22 h), and spatially averaged over all the stations (8 DCCEEW and 5 BoM stations).

10-day Average Metrics									
	Hourly mean temperature at DCCEEW station locations			Instantaneous temperature at BoM station locations			Hourly mean relative humidity at DCCEEW station locations		
Experiment	MBE °C	MAE °C	Corr.	MBE °C	MAE °C	Corr.	MBE %	MAE %	Corr.
Default	1.34	1.75	0.93	1.01	1.69	0.91	-3.43	6.99	0.87
LCZ	1.11	1.62	0.93	0.63	1.61	0.9	-1.94	6.88	0.85
WSF-MB	0.89	1.55	0.92	0.41	1.53	0.9	-0.55	6.93	0.84
Geoscape	0.83	1.49	0.93	0.49	1.52	0.9	-0.45	6.76	0.85
10-day Average Metrics for Before Sunrise (2-5 h)									
	Hourly mean temperature at DCCEEW station locations			Instantaneous temperature at BoM station locations			Hourly mean relative humidity at DCCEEW station locations		
Experiment	MBE °C	MAE °C	Corr.	MBE °C	MAE °C	Corr.	MBE %	MAE %	Corr.
Default	0.95	1.34	0.91	0.55	1.33	0.9	-1.63	5.82	0.87
LCZ	1.75	1.99	0.89	1.39	1.91	0.88	-4.68	7.83	0.79
WSF-MB	1.38	1.73	0.90	1.06	1.67	0.88	-2.23	6.90	0.80
Geoscape	1.27	1.62	0.90	1.05	1.63	0.88	-2.00	6.44	0.82
10-day Average Metrics for Morning (7-10 h)									
	Hourly mean temperature at DCCEEW station locations			Instantaneous temperature at BoM station locations			Hourly mean relative humidity at DCCEEW station locations		
Experiment	MBE °C	MAE °C	Corr.	MBE °C	MAE °C	Corr.	MBE %	MAE %	Corr.
Default	1.84	1.89	0.94	1.97	2.15	0.9	-5.98	7.15	0.88
LCZ	0.85	1.28	0.95	0.54	1.55	0.9	0.61	6.01	0.86
WSF-MB	0.65	1.24	0.95	0.37	1.51	0.9	2.18	6.71	0.85
Geoscape	0.69	1.19	0.95	0.55	1.53	0.9	1.63	6.43	0.86
10-day Average Metrics for Peak Solar Heating (11-14 h)									
	Hourly mean temperature at DCCEEW station locations			Instantaneous temperature at BoM station locations			Hourly mean relative humidity at DCCEEW station locations		
Experiment	MBE °C	MAE °C	Corr.	MBE °C	MAE °C	Corr.	MBE %	MAE %	Corr.
Default	3.01	3.02	0.92	2.88	3.01	0.9	-8.95	10.00	0.78
LCZ	1.72	2.02	0.93	1.19	2.01	0.91	-3.75	7.28	0.79
WSF-MB	1.60	1.94	0.92	1.03	1.95	0.9	-3.19	7.11	0.78
Geoscape	1.58	1.97	0.93	1.19	1.93	0.91	-3.18	7.46	0.78
10-day Average Metrics for Afternoon (15-18 h)									
	Hourly mean temperature at DCCEEW station locations			Instantaneous temperature at BoM station locations			Hourly mean relative humidity at DCCEEW station locations		
Experiment	MBE °C	MAE °C	Corr.	MBE °C	MAE °C	Corr.	MBE %	MAE %	Corr.
Default	1.07	1.87	0.90	0.54	1.63	0.87	-2.44	7.19	0.74
LCZ	0.18	1.59	0.90	-0.4	1.63	0.86	1.03	7.44	0.73
WSF-MB	0.07	1.68	0.88	-0.6	1.68	0.85	1.53	8.35	0.69
Geoscape	-0.06	1.65	0.89	-0.6	1.67	0.85	2.01	8.13	0.71

Table S2. Continued.

10-day Average Metrics for Evening (19-22 h)									
	Hourly mean temperature at DCCEEW station locations			Instantaneous temperature at BoM station locations			Hourly mean relative humidity at DCCEEW station locations		
Experiment	MBE °C	MAE °C	Corr.	MBE °C	MAE °C	Corr.	MBE %	MAE %	Corr.
Default	0.30	1.03	0.94	-0.28	0.89	0.94	0.75	5.64	0.82
LCZ	0.61	1.06	0.95	0.07	0.93	0.94	-0.32	5.33	0.85
WSF-MB	0.41	1.10	0.94	-0.11	0.92	0.94	0.89	5.83	0.82
Geoscape	0.35	1.01	0.95	0	0.93	0.94	1.02	5.46	0.86

Table S2. Mean bias error (MBE) and mean absolute error (MAE) of modelled vs. DCCEEW observed ***hourly mean temperature*** *– with the same temporal averaging as Table S1 at the location of each of the* ***8 DCCEEW stations****. Pearson correlations range from 0.87 to 0.96 averaged over all times and 0.72-0.98 for averages over the 5 diurnal periods and are not mentioned here to save space.*

10-day Average Errors								
	MBE °C							
Experiment	RK	RE	ED	CA	LL	PT	CN	SS
Default	0.87	0.93	0.98	1.16	1.62	1.51	2.10	1.54
LCZ	0.76	0.41	0.60	0.98	1.47	1.18	1.77	1.73
WSF-MB	0.60	0.25	0.43	0.80	0.98	0.88	1.70	1.52
Geoscape	0.55	0.23	0.40	0.60	1.07	0.80	1.55	1.43
	MAE °C							
Experiment	RK	RE	ED	CA	LL	PT	CN	SS
Default	1.37	1.51	1.56	1.63	1.98	1.82	2.24	1.86
LCZ	1.23	1.26	1.40	1.51	1.86	1.65	1.96	2.12
WSF-MB	1.30	1.29	1.43	1.46	1.58	1.51	1.89	1.90
Geoscape	1.26	1.22	1.32	1.41	1.64	1.45	1.79	1.86
10-day Average Errors for Before Sunrise (2-5 h)								
	MBE °C							
Experiment	RK	RE	ED	CA	LL	PT	CN	SS
Default	-0.09	-0.01	0.38	0.73	1.35	1.06	1.72	2.48
LCZ	0.68	0.57	1.28	1.56	2.33	1.75	2.36	3.47
WSF-MB	0.63	0.33	1.06	1.26	1.53	1.36	1.8	3.08
Geoscape	0.44	0.38	0.84	1.16	1.77	0.94	1.9	2.76
	MAE °C							
Experiment	RK	RE	ED	CA	LL	PT	CN	SS
Default	0.78	0.84	0.94	1.05	1.44	1.29	1.84	2.54
LCZ	1.06	1.08	1.75	1.86	2.34	1.91	2.39	3.49
WSF-MB	1.11	0.97	1.7	1.63	1.71	1.66	1.93	3.12
Geoscape	0.98	1.02	1.49	1.5	1.87	1.29	2.02	2.81
10-day Average Errors for Morning (7-10 h)								
	MBE °C							
Experiment	RK	RE	ED	CA	LL	PT	CN	SS
Default	1.66	1.71	1.96	1.74	2.08	2.08	2.08	1.42
LCZ	0.82	0.56	0.72	0.69	0.94	0.94	1.04	1.1
WSF-MB	0.64	0.53	0.55	0.52	0.52	0.57	1.01	0.85
Geoscape	0.74	0.47	0.64	0.41	0.67	0.75	0.89	0.95
	MAE °C							
Experiment	RK	RE	ED	CA	LL	PT	CN	SS
Default	1.8	1.77	1.99	1.76	2.08	2.08	2.08	1.58
LCZ	1.25	1.4	1.43	1.16	1.25	1.25	1.12	1.38
WSF-MB	1.33	1.36	1.38	1.17	0.97	1.19	1.1	1.39
Geoscape	1.3	1.34	1.37	1.08	0.99	1.16	1.01	1.3

Table S2. Continued.

10-day Average Errors for Peak Solar Heating (11-14 h)								
	MBE °C							
Experiment	RK	RE	ED	CA	LL	PT	CN	SS
Default	3.03	3.06	3.19	2.89	3	3.56	3.17	2.15
LCZ	2.06	1.15	1.41	1.69	1.72	2.23	1.75	1.74
WSF-MB	1.76	1.15	1.29	1.72	1.36	1.99	1.97	1.58
Geoscape	1.71	0.98	1.34	1.38	1.48	2.32	1.63	1.83
	MAE °C							
Experiment	RK	RE	ED	CA	LL	PT	CN	SS
Default	3.04	3.12	3.2	2.9	3	3.56	3.18	2.15
LCZ	2.28	2.08	1.88	1.83	1.95	2.3	1.99	1.82
WSF-MB	2.22	2.05	1.95	1.81	1.59	2.14	2.06	1.72
Geoscape	2.3	1.95	1.92	1.71	1.69	2.37	1.92	1.93
10-day Average Errors for Afternoon (15-18 h)								
	MBE °C							
Experiment	RK	RE	ED	CA	LL	PT	CN	SS
Default	0.83	0.96	0.69	1.09	1.59	0.71	2.52	0.18
LCZ	0.19	-0.28	-0.5	0.24	0.88	-0.46	1.55	-0.18
WSF-MB	-0.08	-0.52	-0.61	0.2	0.48	-0.53	1.67	-0.01
Geoscape	-0.01	-0.63	-0.67	-0.38	0.36	-0.52	1.4	-0.03
	MAE °C							
Experiment	RK	RE	ED	CA	LL	PT	CN	SS
Default	1.13	1.61	1.71	2.23	2.43	1.54	2.85	1.43
LCZ	0.97	1.32	1.37	1.88	2.16	1.38	2.16	1.5
WSF-MB	1.21	1.48	1.64	2.09	2.22	1.34	2.31	1.15
Geoscape	1.12	1.34	1.31	2.15	2.32	1.39	2.1	1.49
10-day Average Errors for Evening (19-22 h)								
	MBE °C							
Experiment	RK	RE	ED	CA	LL	PT	CN	SS
Default	-0.23	-0.31	-0.52	0.02	0.54	0.67	1.5	0.75
LCZ	0.17	-0.16	-0.13	0.34	0.96	0.9	1.64	1.17
WSF-MB	0.06	-0.46	-0.31	0.09	0.6	0.57	1.81	0.91
Geoscape	0.04	-0.23	-0.26	0.04	0.62	0.38	1.52	0.65
	MAE °C							
Experiment	RK	RE	ED	CA	LL	PT	CN	SS
Default	0.73	0.75	0.72	0.77	1.35	1.09	1.75	1.08
LCZ	0.82	0.62	0.63	0.73	1.31	1.22	1.78	1.38
WSF-MB	0.87	0.8	0.73	0.74	1.34	1.15	1.94	1.24
Geoscape	0.89	0.64	0.72	0.69	1.21	1.16	1.65	1.13

Table S3. Mean bias error (MBE) and mean absolute error (MAE) of modelled vs. BoM observed ***instantaneous temperature*** *– with the same temporal averaging as Table S1 at the location of each of the* ***5 BoM stations****. Pearson correlations range from 0.89 to 0.93 averaged over all times and 0.74-0.97 for averages over the 5 diurnal periods and are not mentioned here to save space.*

10-day Average Errors										
	MBE °C					MAE °C				
Experiment	OH	SA	CR	OP	BA	OH	SA	CR	OP	BA
Default	0.4	0.46	1.25	1.39	1.57	1.48	1.45	1.68	1.83	2.02
LCZ	0.1	-0.12	0.96	0.85	1.34	1.38	1.4	1.63	1.73	1.91
WSF-MB	0.01	-0.08	0.5	0.65	0.99	1.37	1.41	1.51	1.62	1.75
Geoscape	0.51	-0.14	0.63	0.69	0.76	1.29	1.41	1.55	1.65	1.7
10-day Average Errors for Before Sunrise (2-5 h)										
	MBE °C					MAE °C				
Experiment	OH	SA	CR	OP	BA	OH	SA	CR	OP	BA
Default	-0.73	-0.58	1.19	1.3	1.58	1.01	0.98	1.45	1.48	1.74
LCZ	0.31	0.05	2.2	1.82	2.56	0.94	1.18	2.44	2.25	2.73
WSF-MB	0.19	-0.01	1.53	1.59	1.99	0.82	1.12	1.98	2.13	2.27
Geoscape	0.58	-0.11	1.52	1.65	1.61	0.96	1.08	1.97	2.15	1.99
10-day Average Errors for Morning (7-10 h)										
	MBE °C					MAE °C				
Experiment	OH	SA	CR	OP	BA	OH	SA	CR	OP	BA
Default	1.66	1.47	2.31	2.1	2.33	2.01	1.85	2.41	2.17	2.34
LCZ	0.35	-0.1	0.9	0.6	0.92	1.61	1.54	1.71	1.55	1.33
WSF-MB	0.22	-0.09	0.58	0.47	0.69	1.66	1.58	1.67	1.44	1.2
Geoscape	0.79	-0.13	0.88	0.57	0.65	1.68	1.6	1.71	1.44	1.24
10-day Average Errors for Peak Solar Heating (11-14 h)										
	MBE °C					MAE °C				
Experiment	OH	SA	CR	OP	BA	OH	SA	CR	OP	BA
Default	2.57	2.67	3.08	2.99	3.1	2.77	2.85	3.08	3.06	3.27
LCZ	0.61	0.69	1.51	1.36	1.77	2.32	1.94	1.82	1.89	2.07
WSF-MB	0.73	0.93	1	1.04	1.46	2.21	2.05	1.76	1.76	1.96
Geoscape	1.24	0.78	1.3	1.14	1.5	2.01	2.05	1.94	1.76	1.89
10-day Average Errors for Afternoon (15-18 h)										
	MBE °C					MAE °C				
Experiment	OH	SA	CR	OP	BA	OH	SA	CR	OP	BA
Default	0.16	-0.06	0.47	0.99	1.15	1.04	1.19	1.47	2.13	2.3
LCZ	-0.48	-1.18	-0.52	-0.29	0.26	1.52	1.46	1.22	1.85	2.09
WSF-MB	-0.62	-1.11	-0.91	-0.35	0.03	1.4	1.47	1.49	1.78	2.27
Geoscape	-0.15	-1.1	-0.84	-0.59	-0.29	1.19	1.38	1.43	1.92	2.44
10-day Average Errors for Evening (19-22 h)										
	MBE °C					MAE °C				
Experiment	OH	SA	CR	OP	BA	OH	SA	CR	OP	BA
Default	-0.82	-0.57	-0.15	0.11	0.04	1.01	1	0.61	0.91	0.91
LCZ	-0.38	-0.36	0.33	0.27	0.5	0.89	1.01	0.8	0.99	0.94
WSF-MB	-0.51	-0.31	-0.02	0.11	0.18	0.97	1.02	0.76	0.99	0.84
Geoscape	0.04	-0.33	0.09	0.25	-0.08	0.84	1.06	0.81	1.04	0.92

*Table S4. Same as Table S2 for **hourly mean relative humidity**. Pearson correlations range from 0.75 to 0.91 averaged over all times and 0.29-0.97 for averages over the 5 diurnal periods and are not mentioned here to save space.*

10-day Average Errors								
	MBE %							
Experiment	RK	RE	ED	CA	LL	PT	CN	SS
Default	-1.14	-1.65	-3.95	-2.93	-5.02	-3.70	-5.64	-3.43
LCZ	-0.27	1.23	-2.04	-1.17	-3.78	-1.34	-3.74	-4.43
WSF-MB	0.73	2.32	-0.87	0.23	-1.14	0.42	-2.94	-3.14
Geoscape	0.84	2.07	-0.75	0.28	-2.15	0.80	-2.38	-2.29
	MAE %							
Experiment	RK	RE	ED	CA	LL	PT	CN	SS
Default	6.90	6.46	7.19	6.46	7.72	6.50	7.22	7.47
LCZ	6.30	6.60	7.01	6.57	7.39	6.24	6.68	8.22
WSF-MB	6.84	7.08	7.05	6.73	6.84	6.34	6.55	7.99
Geoscape	6.90	6.70	6.78	6.59	6.85	6.31	6.48	7.43
10-day Average Errors for Before Sunrise (2-5 h)								
	MBE %							
Experiment	RK	RE	ED	CA	LL	PT	CN	SS
Default	3.81	3.13	-1.1	-0.35	-4.29	-1.55	-4.29	-8.39
LCZ	0.01	0.95	-5.31	-2.81	-7.66	-3.66	-6.79	-12.17
WSF-MB	1.4	3.39	-3.3	-0.54	-2.78	-1.41	-3.83	-10.73
Geoscape	1.42	2.46	-2.65	-0.86	-4.69	0.64	-3.69	-8.59
	MAE %							
Experiment	RK	RE	ED	CA	LL	PT	CN	SS
Default	5.99	5.4	5	4.84	5.12	4.82	5.98	9.42
LCZ	5.52	6.23	8.65	7.52	8.45	6.09	7.46	12.7
WSF-MB	5.68	6.14	8.06	6.65	5.7	5.49	5.49	11.99
Geoscape	5.64	6.17	7.56	5.96	6.14	4.14	6.13	9.76
10-day Average Errors for Morning (7-10 h)								
	MBE %							
Experiment	RK	RE	ED	CA	LL	PT	CN	SS
Default	-6.33	-6.37	-9.94	-6.25	-6.91	-5.91	-4.75	-1.34
LCZ	-0.73	1.14	-1.82	1.47	0.16	1.46	2.18	0.98
WSF-MB	0.39	1.58	-1.03	2.91	3.16	3.91	3.12	3.39
Geoscape	-0.31	1.5	-1.02	2.13	1.16	3.08	3.51	2.97
	MAE %							
Experiment	RK	RE	ED	CA	LL	PT	CN	SS
Default	7.88	7.45	10.11	6.63	7.5	6.16	5.24	6.21
LCZ	5.97	7.57	7.98	6.14	5.17	5.07	4.66	5.5
WSF-MB	6.5	7.76	7.67	6.81	6.44	6.39	5.49	6.6
Geoscape	6.24	7.47	7.97	6.51	5.01	6.04	5.83	6.38

Table S4. Continued.

10-day Average Errors for Peak Solar Heating (11-14 h)								
	MBE %							
Experiment	RK	RE	ED	CA	LL	PT	CN	SS
Default	-8.9	-9.22	-10.97	-9.63	-9.07	-10.64	-8.4	-4.78
LCZ	-4.24	-1.23	-4.1	-4.24	-3.95	-5.56	-2.82	-3.87
WSF-MB	-3.26	-1.44	-3.23	-4.35	-2.89	-4.75	-2.6	-3
Geoscape	-2.37	-1.15	-3.5	-3.73	-3.73	-5.63	-1.71	-3.63
	MAE %							
Experiment	RK	RE	ED	CA	LL	PT	CN	SS
Default	10.97	10.42	12.81	10.32	9.41	10.66	8.91	6.47
LCZ	10.03	8.73	8.88	6.07	6.01	7.08	5.65	5.79
WSF-MB	9.81	8.62	9.11	6.37	5.16	6.81	5.33	5.65
Geoscape	11.11	8.14	8.95	6.78	5.82	7.21	5.78	5.91
10-day Average Errors for Afternoon (15-18 h)								
	MBE %							
Experiment	RK	RE	ED	CA	LL	PT	CN	SS
Default	-1.64	-1.6	-2.58	-2.26	-4.63	-0.7	-7.49	1.35
LCZ	1.39	3.5	2.38	1.63	-1.96	3.79	-4.07	1.57
WSF-MB	2.93	4.47	2.82	1.65	-0.65	4.56	-4.68	1.13
Geoscape	2.17	4.99	3.07	3.8	-0.36	4.5	-3.6	1.49
	MAE %							
Experiment	RK	RE	ED	CA	LL	PT	CN	SS
Default	5.54	5.49	6.79	8.07	8.95	5.26	9.76	7.65
LCZ	5.51	6.54	6.37	8.51	9.3	7.31	8.19	7.78
WSF-MB	7.19	7.84	7.49	10.11	10.32	7.84	8.8	7.18
Geoscape	6.25	7.36	6.37	10.45	10.35	7.93	8.39	7.96
10-day Average Errors for Evening (19-22 h)								
	MBE %							
Experiment	RK	RE	ED	CA	LL	PT	CN	SS
Default	4.16	3.6	2.59	1.7	-1.18	-0.66	-4.32	0.08
LCZ	2.04	3.1	0.51	0.59	-2.53	0.08	-4.34	-1.99
WSF-MB	2.6	4.99	1.64	2.46	-0.67	1.62	-4.82	-0.73
Geoscape	2.98	3.67	1.49	2.09	-0.88	2.04	-3.94	0.71
	MAE %							
Experiment	RK	RE	ED	CA	LL	PT	CN	SS
Default	5.58	4.72	3.75	4.3	7.49	6.24	6.9	6.12
LCZ	5.22	4.45	2.98	4.47	6.79	6.09	6.7	5.96
WSF-MB	5.92	5.59	3.59	4.87	7.1	6.23	7.15	6.18
Geoscape	5.93	4.62	3.47	4.46	6.68	6.86	5.89	5.73

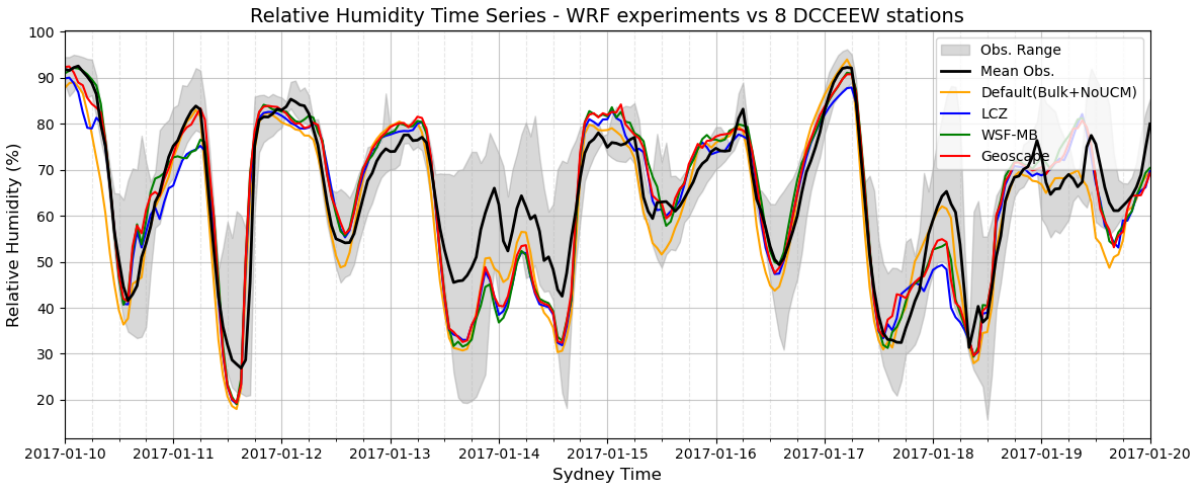

Figure S6. Time series of hourly mean relative humidity averaged over the 8 Department of Climate Change, Energy, the Environment and Water DCCEEW stations in Sydney. Results from four WRF experiments (see legends) are compared with the average values for weather station measurements (solid black line). The shadowed area shows the range of observational data across sites (see Figure S3Figure S4).

Table S5. The mean bias error (MBE) and mean absolute error (MAE) values of the modelled hourly mean relative humidity for the Default and Geoscape experiments compared with the observations from the DCCEEW stations averaged over the 8 stations (All) and at the Liverpool station (LL). The last line shows the improvements made by the Geoscape case in the metrics. See Table S1Table S4 for more information.

	Hourly mean relative humidity - 10-day average metrics				Hourly mean relative humidity - 10-day average for peak solar heating (11-14 h) metrics			
	MBE %		MAE %		MBE %		MAE %	
Experiment	All	LL	All	LL	All	LL	All	LL
Default	-3.43	-5.02	6.99	7.72	-8.95	-9.07	10.0	9.41
Geoscape	-0.45	-2.15	6.76	6.85	-3.18	-3.73	7.46	5.82
Default - Geoscape	**-2.98**	**-2.87**	**0.23**	**0.87**	**-5.77**	**-5.34**	**2.54**	**3.59**

Table S6. The mean bias error (MBE) and mean absolute error (MAE) values of the modelled hourly mean relative humidity for the LCZ, WSF-MB and Geoscape experiments compared with the observations from the DCCEEW stations averaged over the 8 stations (All) and at the St Marys station (SS). The last two lines show the differences in metrics with the Geoscape case. See Table S1Table S4 for more information.

	Hourly mean relative humidity - 10-day average metrics				Hourly mean relative humidity - 10-day average for before sunrise (2-5 h) metrics			
	MBE %		MAE %		MBE %		MAE %	
Experiment	All	SS	All	SS	All	SS	All	SS
LCZ	-1.94	-4.43	6.88	8.22	-4.68	-12.17	7.83	12.7
WSF-MB	-0.55	-3.14	6.93	7.99	-2.23	-10.73	6.90	11.99
Geoscape	-0.45	-2.29	6.76	7.43	-2.00	-8.59	6.44	9.76
LCZ - Geoscape	**-1.49**	**-2.14**	**0.12**	**0.79**	**-2.68**	**-3.58**	**1.39**	**2.94**
WSF-MB - Geoscape	**-0.1**	**-0.85**	**0.17**	**0.56**	**-0.23**	**-2.14**	**0.46**	**2.23**

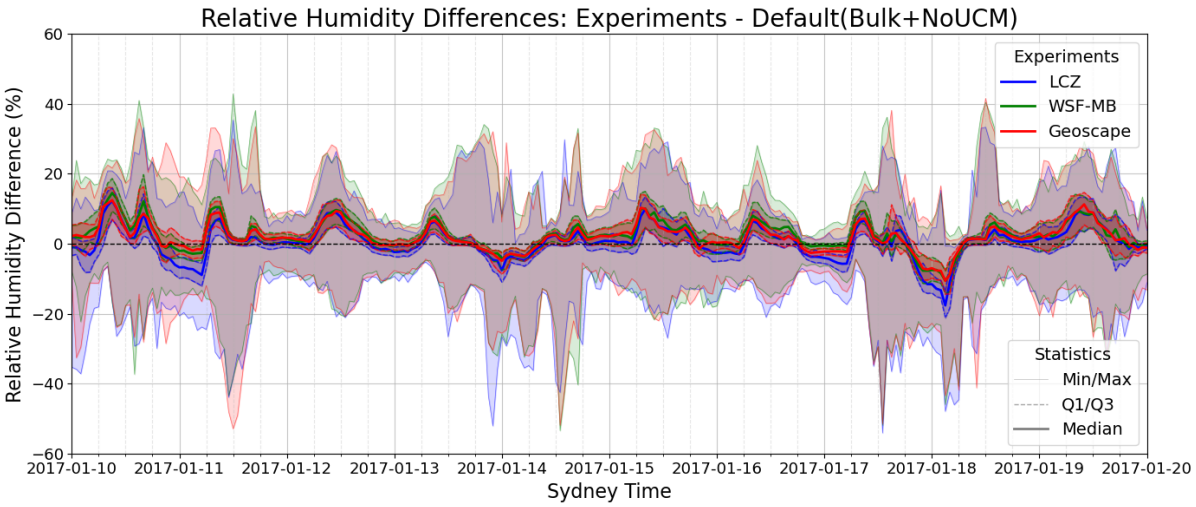

Figure S7. Statistical distribution of instantaneous relative humidity differences of the LCZ, WSF-MB, and Geoscape experiments with the Default case at all the spatial points during the simulation period. The five lines for each experiment specify the minimum, maximum, first quartile, median, and third quartile.

Table S7. The value and time of the top 10 instantaneous temperature and relative humidity differences of the LCZ, WSF-MB, and Geoscape experiments with the Default case across our urban domain. LCZ top temperature differences mostly occur at nighttime (3, 21, 22 h) on 13 and 18 Jan. The WSF-MB and Geoscape top temperature differences happen at daytime. Relative humidity differences range from 34.26 to 52.94%. Most of the top LCZ – Default relative humidity differences happen during nighttime.

Top 10 Air Temperature Differences						
	LCZ – Default		WSF-MB – Default		Geoscape - Default	
	Difference °C	Time	Difference °C	Time	Difference °C	Time
1	10.66	13/01 22:00	10.99	11/01 11:00	13.09	11/01 12:00
2	10.55	11/01 11:00	10.51	18/01 12:00	11.76	11/01 11:00
3	10.29	18/01 3:00	10.28	11/01 12:00	11.56	11/01 12:00
4	10.23	11/01 11:00	10.25	18/01 14:00	10.93	11/01 11:00
5	10.12	18/01 3:00	10.21	14/01 13:00	10.88	18/01 12:00
6	9.99	18/01 3:00	10.19	11/01 11:00	10.35	11/01 12:00
7	9.83	18/01 3:00	9.88	18/01 13:00	10.14	14/01 13:00
8	9.79	18/01 3:00	9.87	18/01 13:00	10.00	11/01 13:00
9	9.65	18/01 3:00	9.82	18/01 11:00	9.98	14/01 13:00
10	9.48	13/01 21:00	9.74	14/01 13:00	9.81	11/01 10:00
Top 10 Relative Humidity Differences						
	LCZ – Default		WSF-MB – Default		Geoscape - Default	
	Difference %	Time	Difference %	Time	Difference %	Time
1	54.12	17/01 13:00	53.46	14/01 13:00	52.94	11/01 12:00
2	52.13	13/01 22:00	51.94	17/01 13:00	51.95	14/01 13:00
3	47.94	18/01 3:00	50.62	14/01 13:00	51.52	17/01 13:00
4	47.23	18/01 3:00	48.74	14/01 13:00	50.82	14/01 13:00
5	47.16	18/01 3:00	46.04	14/01 13:00	49.09	14/01 13:00
6	47.15	18/01 3:00	46.00	18/01 3:00	49.05	11/01 13:00
7	47.07	18/01 3:00	45.90	18/01 3:00	48.03	11/01 11:00
8	46.07	18/01 5:00	45.37	18/01 3:00	46.19	14/01 13:00
9	45.68	18/01 5:00	44.32	14/01 13:00	45.71	11/01 12:00
10	45.01	18/01 3:00	43.49	11/01 11:00	43.98	11/01 11:00

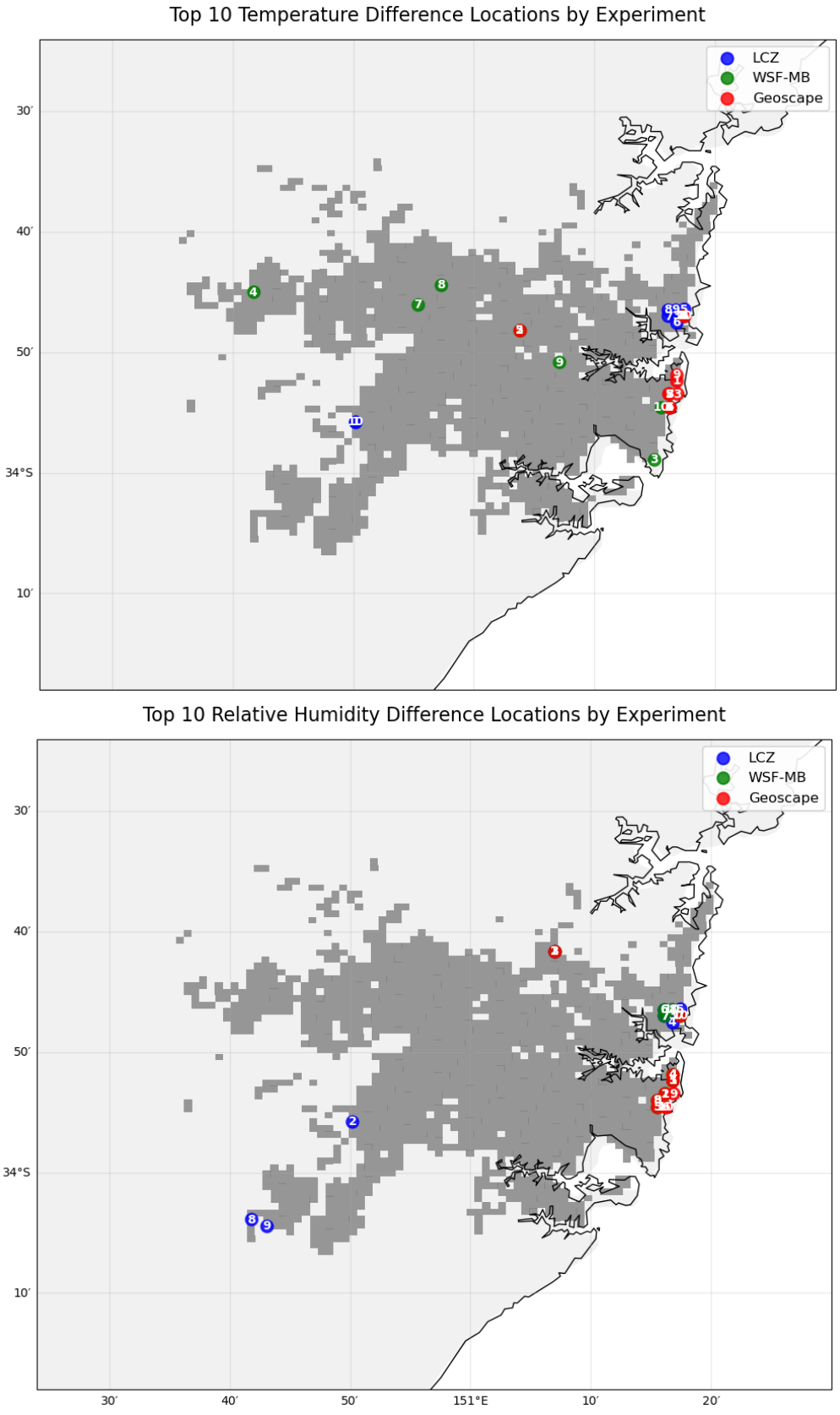

Figure S8. The location of the top 10 instantaneous temperature (top) and top 10 instantaneous relative humidity (bottom) differences of the experiments with the Default experiment. Top differences mostly occur along the coast.

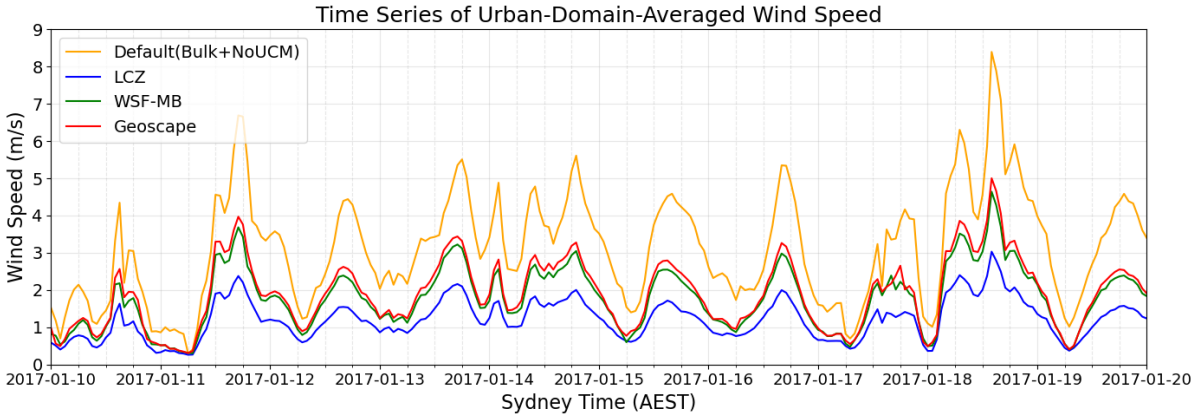

Figure S9. Time series of wind speed averaged over the entire urban domain.

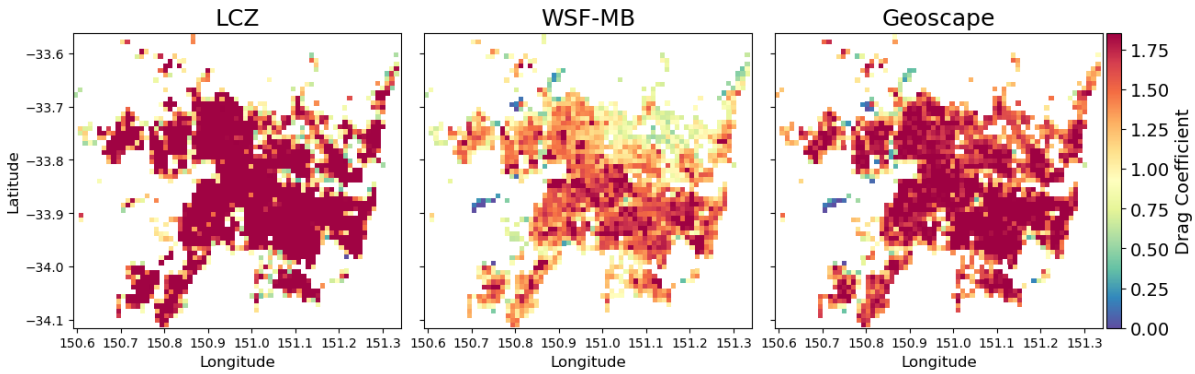

Figure S10. Drag coefficient as calculated in the urban canopy (Santiago & Martilli, 2010).

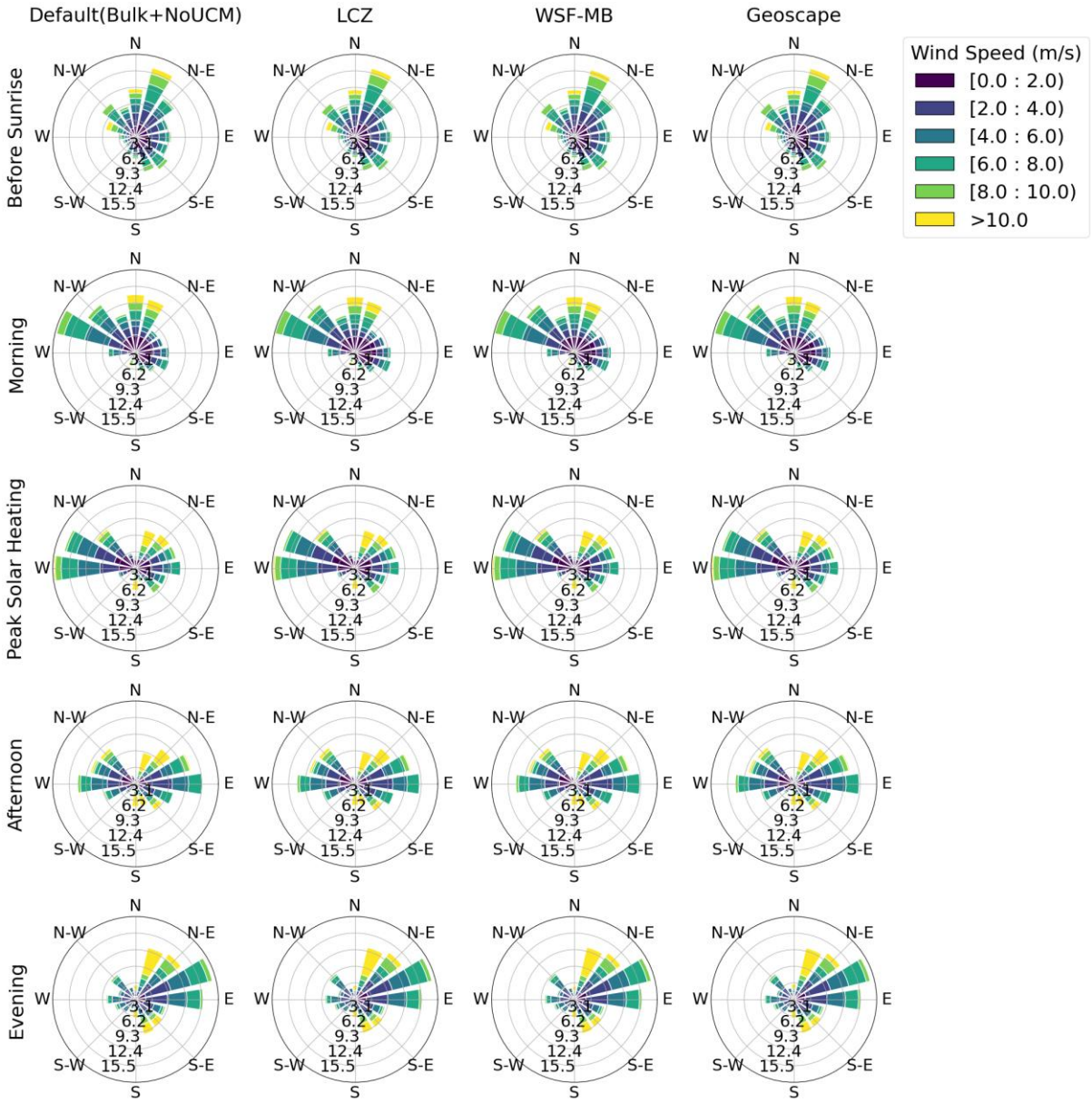

Figure S11. Temporal evolution of windroses over the entire nested domain for the four experiments.

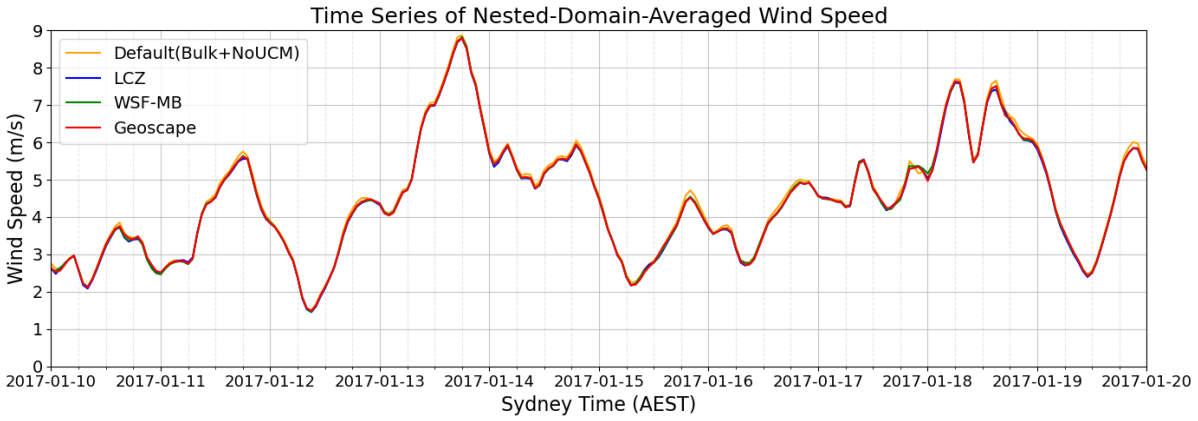

Figure S12. Time series of wind speed averaged over the nested domain.

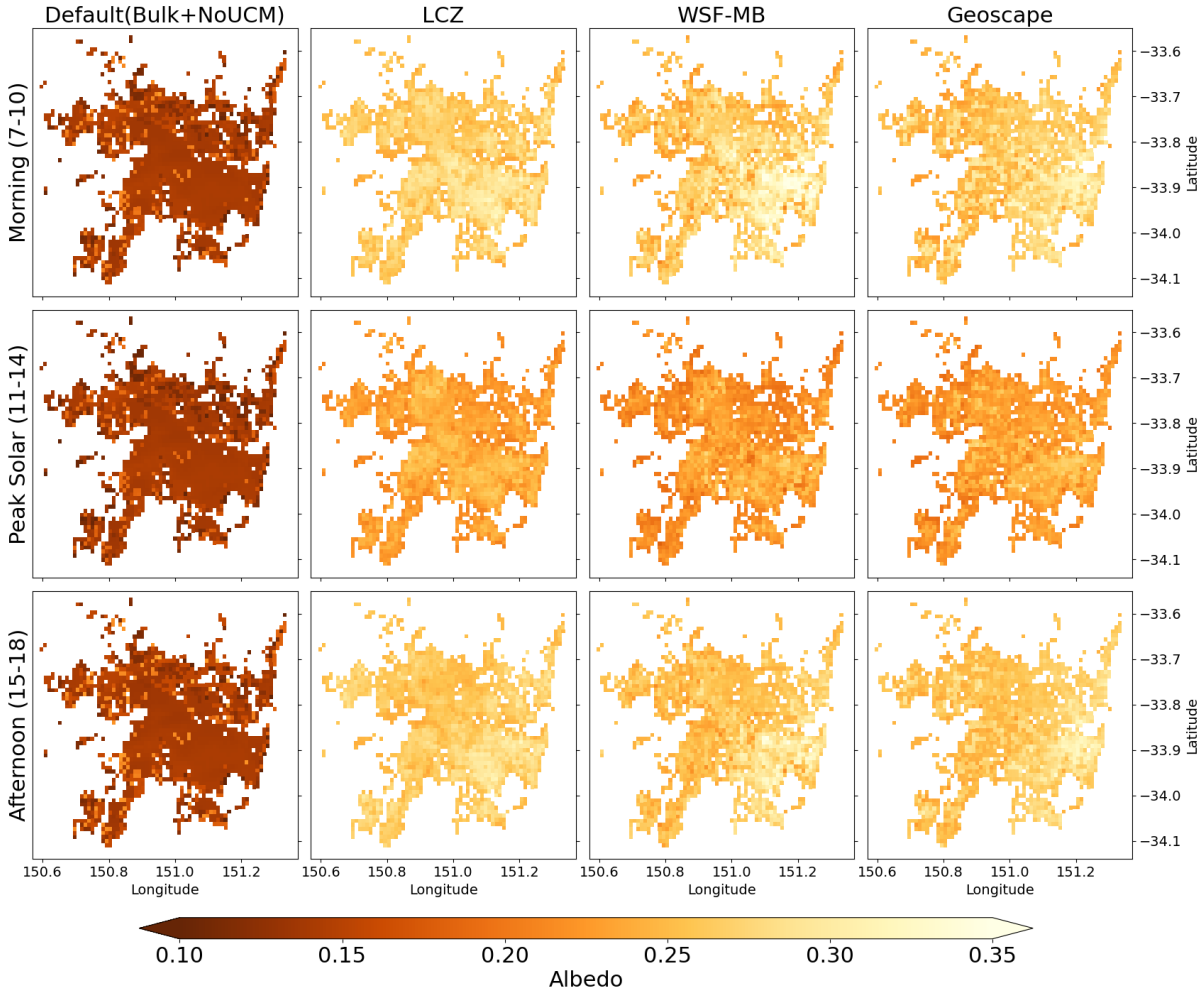

Figure S13. The diurnal evolution of albedo spatial maps for the four experiments.

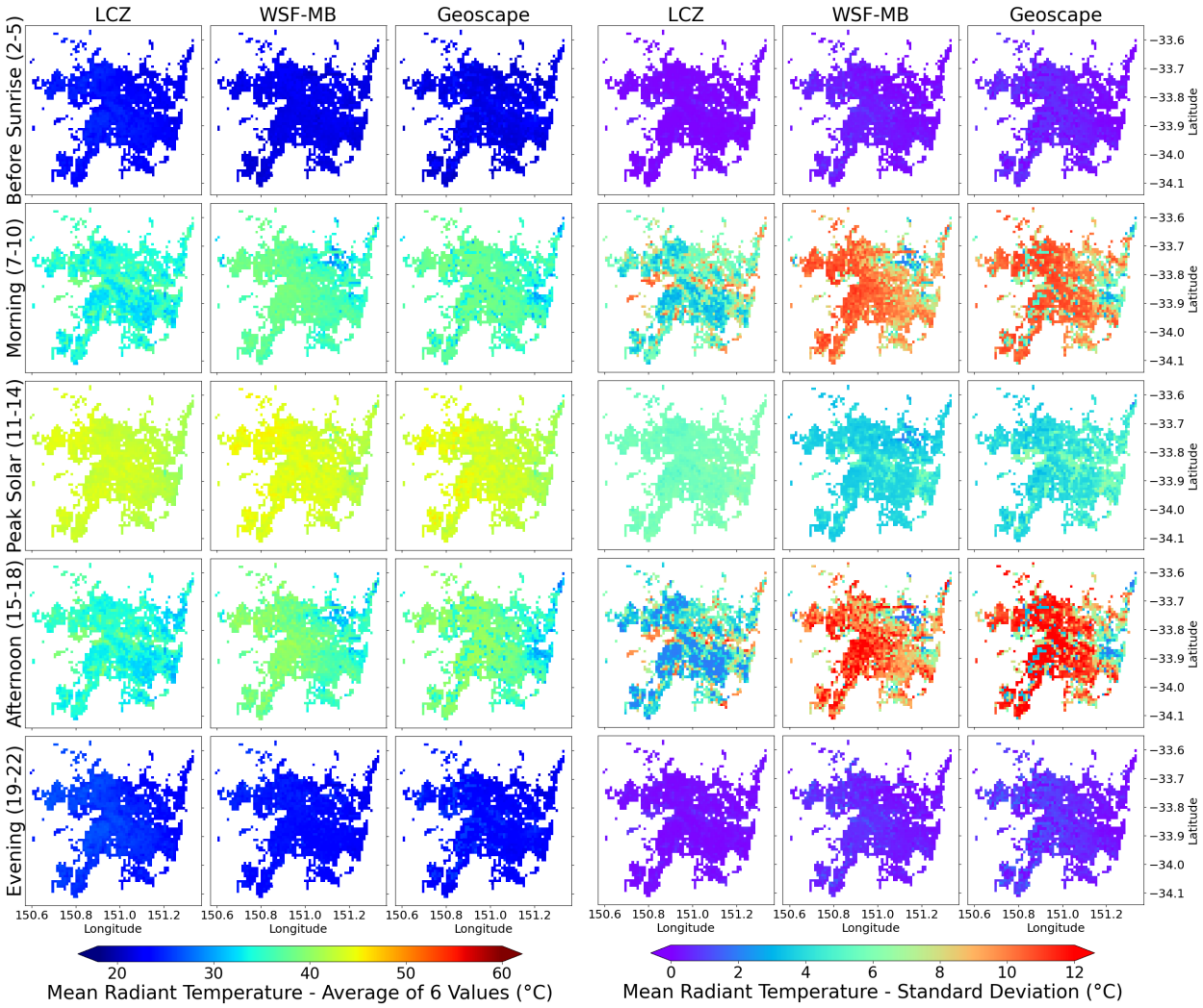

Figure S14. The temporal evolution of mean radiant temperature spatial maps for the LCZ, WSF3DMSB, and Geoscape experiments: average of the 6 WRF-Comfort values (left), and the corresponding standard deviation (right).

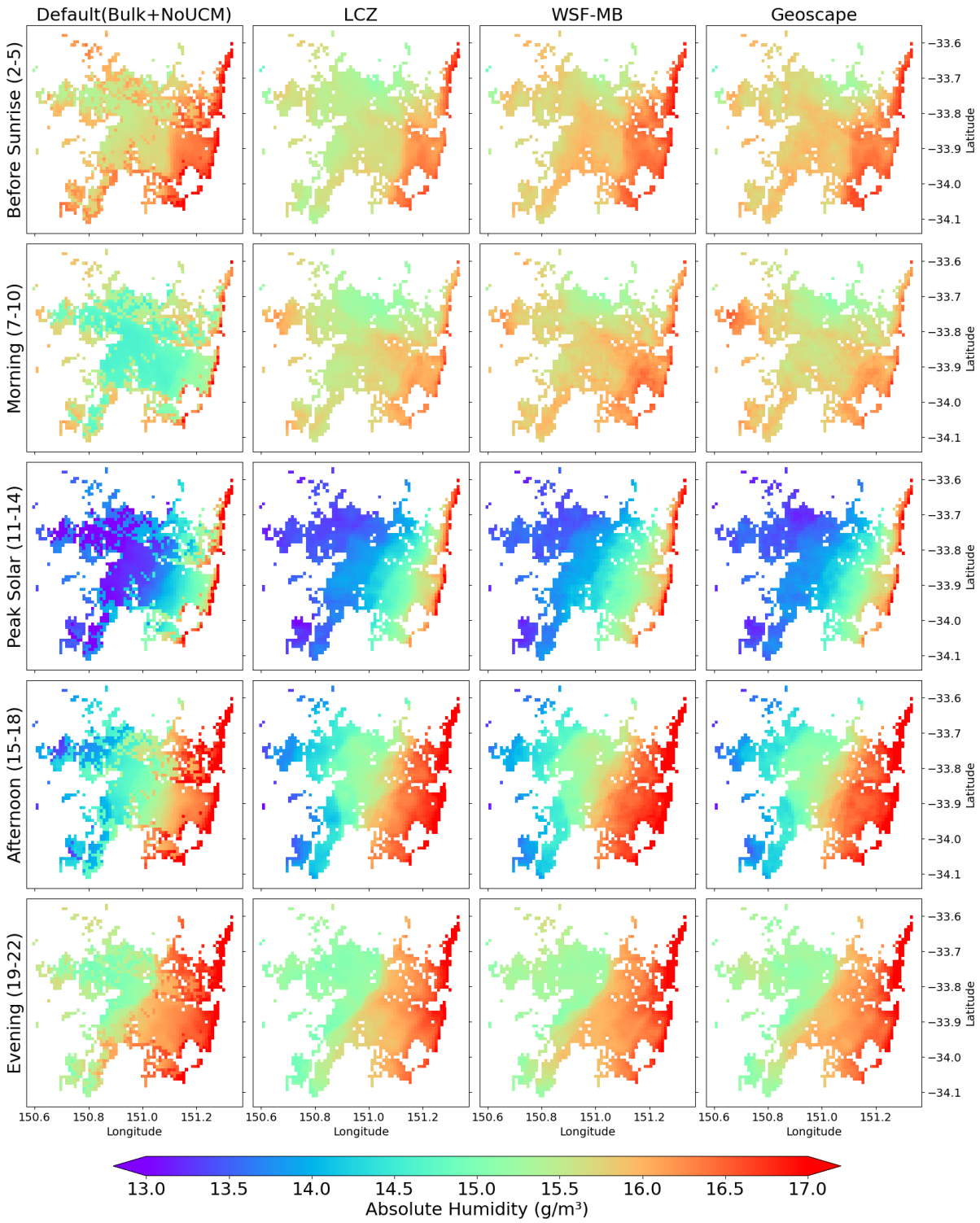

Figure S15. The temporal evolution of 2-m absolute humidity spatial maps for the four experiments.

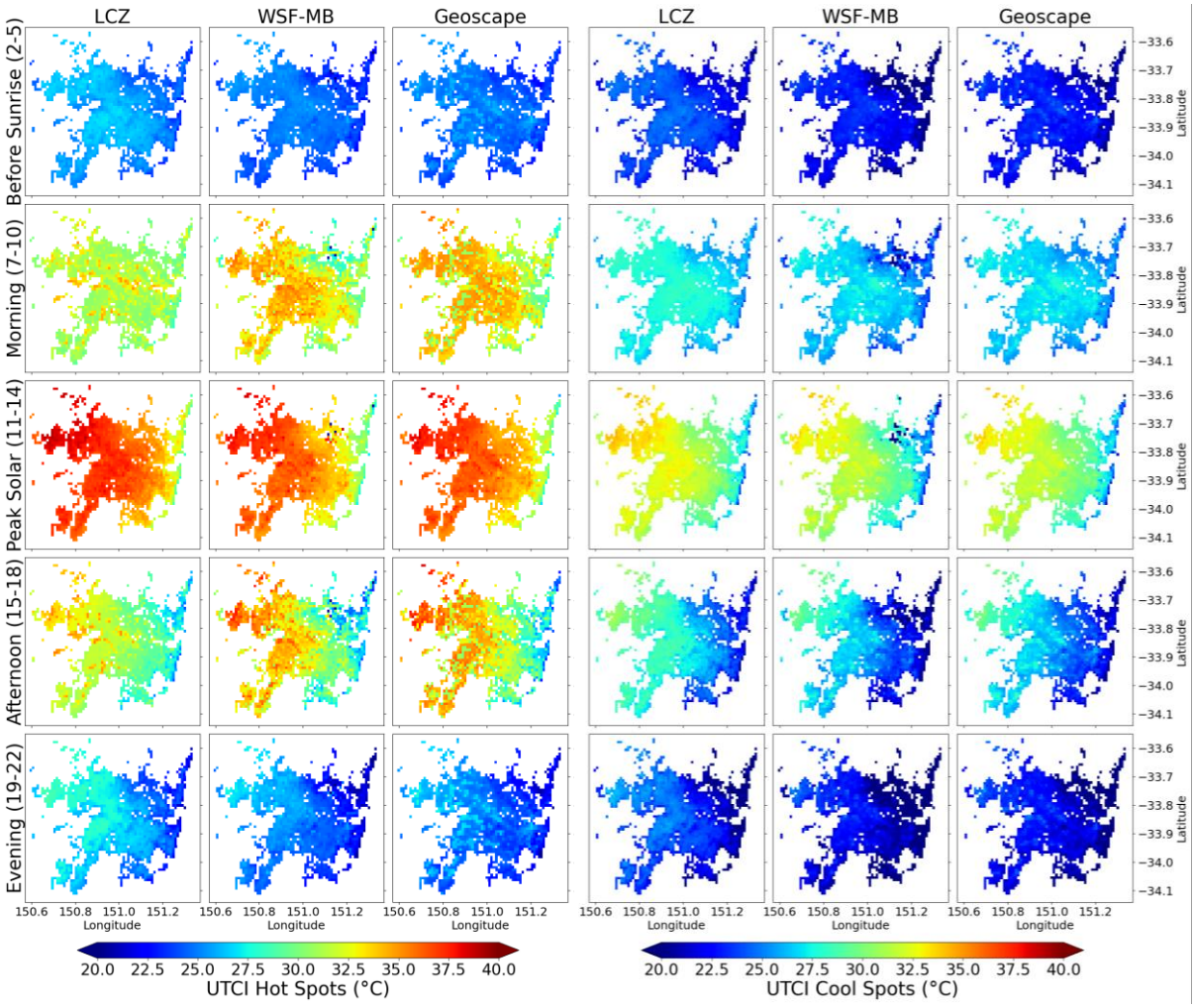

Figure S16. The temporal evolution of the UTCI spatial maps for hot spots (left) and cool spots (right) for the four experiments.

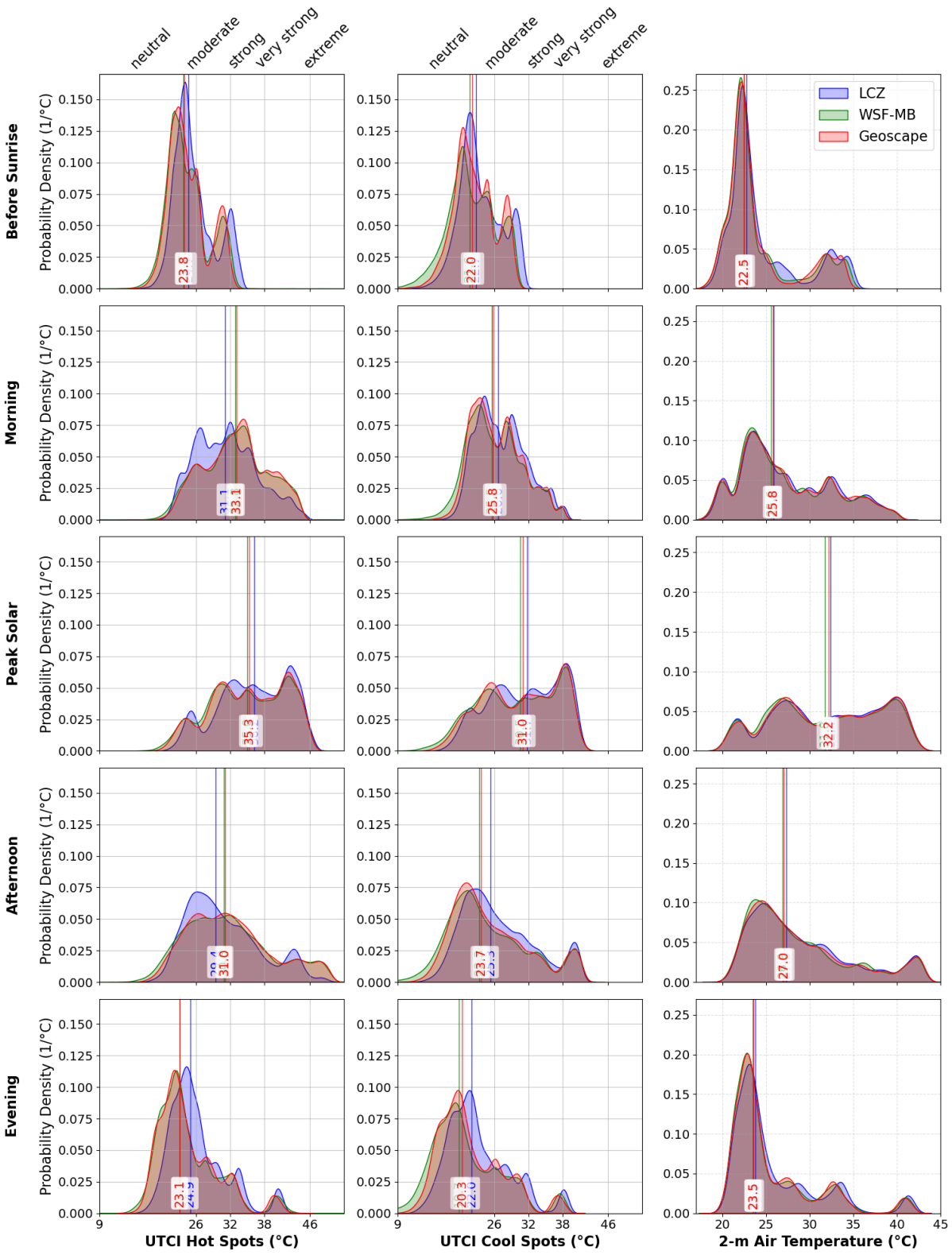

Figure S17. Probability density distribution of UTCI hot spots, UTCI cool spots, and 2m air temperature during different diurnal periods (rows) for the LCZ, WSF-MB, and Geoscape cases. The area under the curve equals to 1.

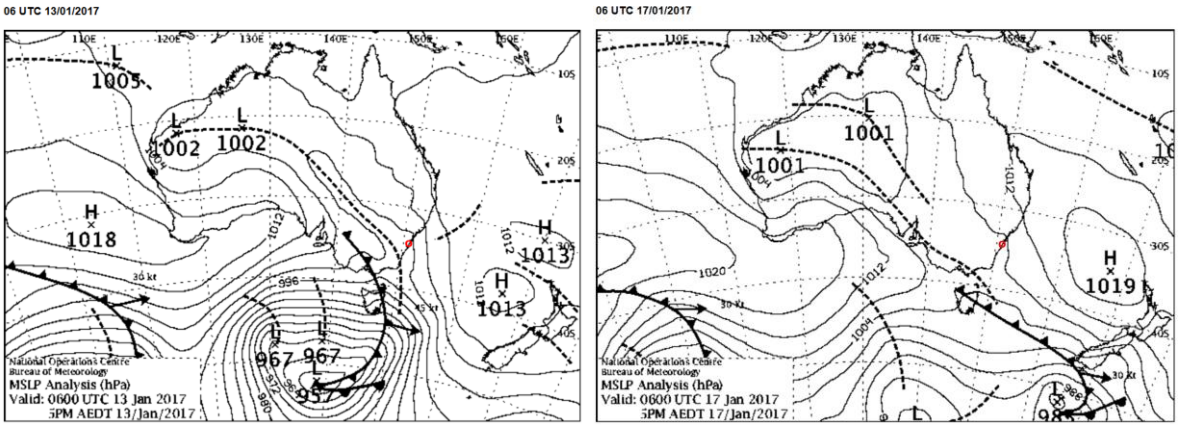

Figure S18. Mean sea level pressure (MSLP) analysis for Australia and New Zealand on 13 January 2017, 16:00 AEST (left), and on 17 January 2017, 16:00 AEST (right) from (Analysis Chart Archive, n.d.). The red mark shows the approximate location of Sydney. The denser isobar lines on 13th, with a strong low-pressure centre of 957 hPa, indicate a stronger synoptic influence compared with the 17th.

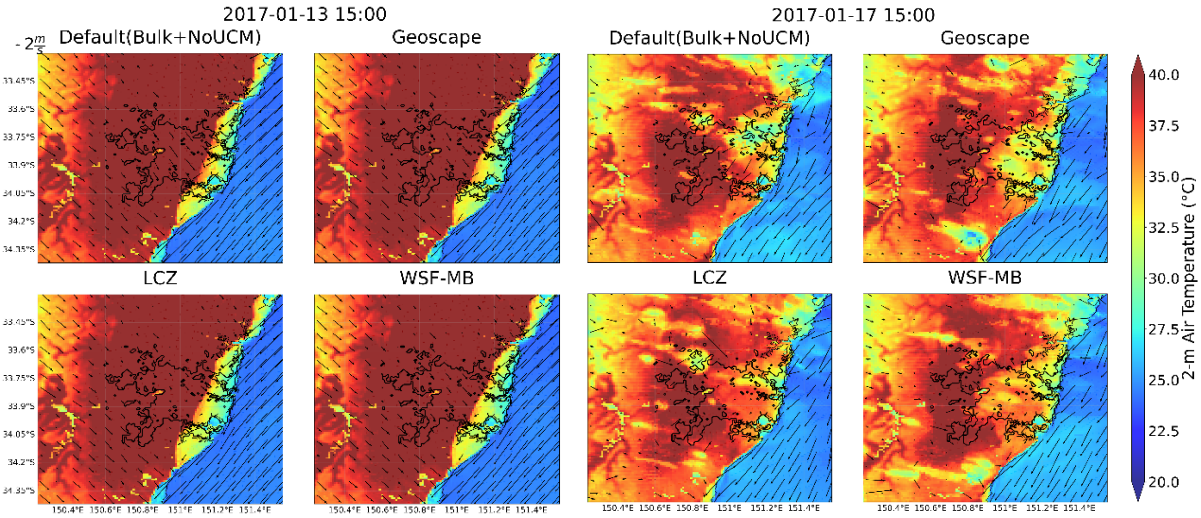

Figure S19. Snapshots of temperature maps with wind vectors on top for the LCZ, WSF3DMSB, and Geoscape experiments on 13 January 2017, 15:00 AEST (left), and on 17 January 2017, 15:00 AEST (right).

Table S8. High-built and low-built points with the elevations of 31.79 m and 75.47 m above sea level and classified as local climate zones of 1, compact highrise, and 3, compact lowrise, respectively. The high-built point is located at the high-built part of Sydney central business district.

	High built (-33.88, 151.20)			Low built (-33.83, 151.21)		
	LCZ	WSF-MB	Geoscape	LCZ	WSF-MB	Geoscape
Impervious fraction	0.8	0.84	0.85	0.54	0.55	0.49
Plan area density	0.41	0.34	0.52	0.3	0.1	0.2
area-weighted mean building height (m)	29.09	38.07	30.3	17.31	10.38	9.77
building surface to plan area ratio	1.6	1.46	1.6	0.69	0.04	0.4

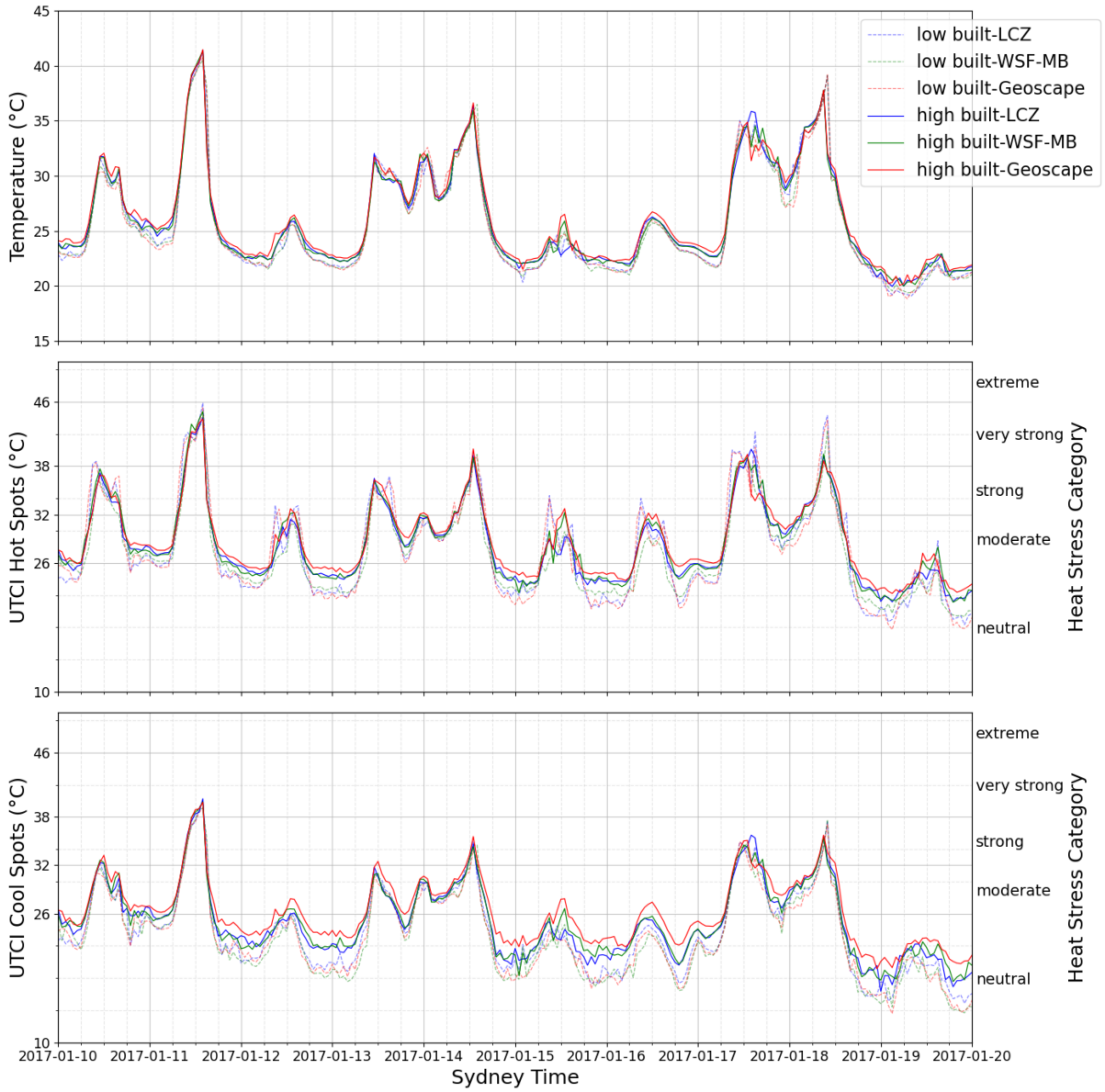

Figure S20. Time series of 2-m air temperature (first row), UTCI hot spots (second row), and UTCI cool spots (third row) in one of the highest built areas in Sydney's central business district (solid lines) and a low-built point (dashed lines) within a similar longitude for the LCZ (blue lines), WSF-MB (green lines), and Geoscape (red lines) cases.

References

Analysis Chart Archive. (n.d.). Bureau of Meteorology. Retrieved October 5, 2025, from https://www.bom.gov.au/australia/charts/archive/index.shtml

Department of Climate Change, Energy, the Environment and Water. (2023, December 19). *Data download facility*. Air Quality NSW. https://www.airquality.nsw.gov.au/air-quality-data-services/data-download-facility

Santiago, J. L., & Martilli, A. (2010). A dynamic urban canopy parameterization for mesoscale models based on computational fluid dynamics Reynolds-averaged Navier–stokes microscale simulations. *Boundary - Layer Meteorology*, *137*(3), 417–439.